Optische ontvangers voor opwaarts netwerkverkeer in passieve optische netwerken van de volgende generatie

Optical Receivers for Upstream Traffic in Next-Generation Passive Optical Networks

Gertjan Coudyzer

Promotoren: prof. dr. ir. X. Yin, dr. ir. P. Ossieur
Proefschrift ingediend tot het behalen van de graad van
Doctor in de ingenieurswetenschappen: elektrotechniek

Vakgroep Informatietechnologie
Voorzitter: prof. dr. ir. B. Dhoedt
Faculteit Ingenieurswetenschappen en Architectuur
Academiejaar 2019 - 2020

UNIVERSITEIT
GENT

ISBN 978-94-6355-339-1
NUR 959
Wettelijk depot: D/2020/10.500/16

FACULTY OF ENGINEERING
AND ARCHITECTURE

GHENT
UNIVERSITY

Ghent University
Faculty of Engineering and Architecture

Department of Information Technology
Tech Lane Ghent Science Park Campus A
iGent Tower, Technologiepark-Zwijnaarde 126,
B-9052 Ghent, Belgium

Tel.: +32 9 264 33 28

Optical Receivers for Upstream Traffic in Next-Generation Passive Optical Networks

Gertjan Coudyzer

Members of the Examination Board:

em. prof. dr. ir. Luc Taerwe	(Chairman)	Ghent University
prof. dr. ir. Xin Yin	(Supervisor)	Ghent University
dr. ir. Peter Ossieur	(Supervisor)	Ghent University
prof. dr. ir. Johan Bauwelinck		Ghent University
prof. dr. ir. Mario Pickavet		Ghent University
prof. dr. ir. Pieter Rombouts		Ghent University
prof. dr. Derek Nesset		Huawei Technologies
prof. dr. Marion Matters		TU/e

Dissertation submitted to obtain the degree of
Doctor of Electrical Engineering
Academic year 2019-2020

This work was supported by
The Ghent University Special Research Fund (BOF).

Voorwoord

Beste promotoren en collega's,
Beste vrienden en familie,

Na bijna 6 jaar is het bijna zover en is het einde van mijn doctoraat in zicht. Toen ik destijds in door de deuren van het toenmalige - wat uit de Sovjetperiode leek af te stammen - Technicum binnenwandelde, werd ik bijna een beetje overdonderd door de sterke expertise aanwezig in het lab. Doorheen de jaren ben ik dan ook gegroeid van onervaren ad-hoc circuit-ontwerper tot volwaardig chip-designer, waarbij structurele aanpak en doordachte redeneringen centraal staan. Dit zou niet mogelijk geweest zijn zonder in eerste plaats de hulp van mijn mede (ex)-chip-designers, waarvoor ik hen allemaal wil bedanken.

In het bijzonder wil ik dan ook mijn promotoren dr. ir. Peter Ossieur en prof. Xin Yin bedanken. Scott, I would like to thank you for introducing me into the wondrous world of passive optical access networks, your expertise, and bringing me into contact with the industry. Peter heeft zich pas na enige tijd terug aan de groep toegevoegd, maar zijn aanwezigheid heeft een ongelofelijke boost gegeven aan mijn onderzoek. Peter, jouw inzichten in burst-mode ontvangers, -egalisatie en de experimentele opbouw van passieve optische netwerken hebben tot doorbraken geleid die anders maanden - zoniet jaren - op zich zouden laten wachten.

Ik wil prof. Johan Bauwelinck graag bedanken; in eerste instantie om mij te laten starten bij de IDLab Design-groep; maar ook voor de verdere ondersteuning en ook het aangename gezelschap tijdens de vele WIPE-vergaderingen, al dan niet in het buitenland. Daarnaast wil ik ook prof. dr. ir. Guy Torfs bedanken, die met tijd en stond mijn redeneringen kon bijsturen met een aantal wel-doordachte inzichten.

Daarnaast wens ik ook prof. dr. ir. Bart Dhoedt en prof. dr. ir. Piet Demeester te bedanken voor de financiële en structurele omkadering. Ik wil graag ook Mike Van Puyenbroeck bedanken voor de administratieve hulp, en voor het verwerken van de zoveelste onkostennota of reisaanvraag.

Tenslotte wil ik ook nog ing. Jan Gillis en ir. Joris Van Kerrebrouck (waar hopelijk binnenkort ook dr. mag aangeplakt worden) bedanken voor alle technologische ondersteuning. Zij stonden in een mum van tijd klaar om PCB's te frezen of om nieuwe connectors, kabels of optische componenten te bestellen wanneer dit nodig was.

A small word towards the project partners: By now, the WIPE-project has been succesfully completed, and I would like to thank the many partners that helped in its realization. Within the context of this project, I was given the opportunity to develop two full on-chip receivers with virtually no space limitations. I am already looking forward towards the wafer-bonded end result of Design 2.

Er waren helaas ook vaak momenten waarop het allemaal minder makkelijk ging. Daarom wil ik ook mijn vrienden bedanken die voor mij klaarstonden wanneer ik 's avonds thuiskwam na de vele lange werkdagen. De immense steun die ik van hen kreeg wanneer de stilte toesloeg heeft er voor gezorgd dat ik dit werk nooit vroegtijdig opgaf, maar dat ik doorzette tot het einde. En op de verschillende folkbals werd ik steeds met open armen ontvangen, en kon ik even de stress van chip-tapeouts en 70-uur-tellende werkweken tijdens metingen in het labo volledig vergeten. Dankjewel Bart, Anneleen, Philip, Laura, Wim, Dorien, Bas, Floris, Davy, Ellen, Marie, Sven, Dries, Caroline, Joachim, Jeroen, Klaus, Sarah, Miriam, en eigenlijk nog vele anderen die evenwaardig vermeld mogen worden. Ook de vele reizen en tripjes met sommigen van jullie doorheen de jaren zullen mij steeds bijblijven.

Ik wil daarnaast ook graag mijn reisgenoten bedanken voor het prachtige avontuur in Costa Rica twee maanden geleden, dat ik niet snel zal vergeten. Tenslotte wil ik ook mijn familie - in het bijzonder mijn moeder - bedanken, omdat zij uiteindelijk diegenen zijn die ervoor gezorgd hebben dit alles mogelijk te maken en steeds voor alles klaarstaan.

Gent, Januari 2020

Gertjan Coudyzer

Table of Contents

List of Figures

List of Tables

Acronyms

ADC analog-to-digital converter.

ADSL Assymetric Digital Subscriber Line.

AGC automatic-gain-control.

AOC automatic-offset-control.

APD avalanche photodiode.

ARPA Advanced Research Projects Agency.

ATM Asynchronous Transfer Mode.

AWG arbitrary waveform generator.

AWG arrayed waveguide grating.

BCH Bose-Chaudhuri-Hocquenghem.

BER bit error rate.

BM burst-mode.

BMCDR burst-mode clock- and data-recovery.

BMEDC burst-mode electronic dispersion compensation.

BMEQ burst-mode equalization.

BMRX burst-mode receiver.

BMTX burst-mode transmitter.

CAGR compound annual growth rate.

CDR clock- and data-recovery.

CID consecutive identical digits.

CM continuous-mode.

CML current-mode logic.

CPE customer premises equipment.

CW continuous-wave.

DAC digital-to-analog converter.

DDA differential difference amplifier.

DFB distributed feedback.

DFE decision-feedback equalizer.

DLM dynamic line management.

DML directly modulated laser.

DS downstream.

DSL Digital Subscriber Line.

DSP digital signal processing.

DWDM (dense) wavelength division multiplexing.

EAM electro-absorption modulator.

EDC electronic dispersion compensation.

EML externally modulated laser.

EOB end-of-burst.

FEC forward error correcting.

FEXT far-end crosstalk.

FFE feedforward equalizer.

FFS for further study.

FP Fabry-Perot.

FPGA field programmable gate array.

FSAN Full Service Access Network.

FTTB Fiber-to-the-Building.

FTTC Fiber-to-the-Curb.

FTTH Fiber-to-the-Home.

GBWP gain-bandwidth product.

HFC Hybrid Fiber-Coax.

IP Internet Protocol.

ISI inter-symbol interference.

ISP Internet service provider.

LBMRX linear burst-mode receiver.

LBMTIA linear burst-mode transimpedance amplifier.

LDPC low-density parity check.

LMS least-mean-squares.

LPF low-pass filter.

LUT look-up table.

MAC medium access control.

MPN mode partition noise.

MZM Mach-Zehnder-modulator.

NPD negative peak-detector.

NRZ non-return-to-zero.

OADM optical add-drop multiplexer.

OD output driver.

ODN optical distribution network.

OFDM orthogonal frequency division multiplexing.

OLT optical line terminal.

ONU optical network unit.

OOK on-off keying.

P2P point-to-point.

PAM-4 4-level pulse amplitude modulation.

PCB printed circuit board.

PON passive optical network.

PPD postive peak-detector.

PRBS pseudo-random binary sequence.

QAM quadrature amplitude modulation.

RLS recursive-least-squares.

RMS root-mean-square.

ROP remote optical platform.

RS Reed-Solomon.

RTO real-time-oscilloscope.

S2D single-ended-to-differential.

SMF single-mode fiber.

SNR signal-to-noise ratio.

SOA semiconductor optical amplifier.

SOB start-of-burst.

TDM time division multiplexing.

TDM-PON time-division multiplexed PON.

TDMA time-division multiple access.

TDP transmitter dispersion penalty.

THD total harmonic distortion.

TIA transimpedance amplifier.

TWDM-PON time-wavelength division multiplexing PON.

US upstream.

VDSL Very-high-bit-rate Digital Subscriber Line.

VGA variable-gain-amplifier.

VNA vector network analyzer.

VOA variable optical attenuator.

VR virtual reality.

WDM wavelength division multiplexing.

WDM-PON wavelength-division multiplexed PON.

Nederlandstalige Samenvatting –Dutch Summary–

De voorbije decennia is het Internet geleidelijk aan geëvolueerd in een globaal medium dat gebruikt wordt door mensen van over de hele wereld. De maatschappij berust steeds meer op dit netwerk, met als gevolg dat het globale netwerkverkeer heel snel stijgt.

Het Internet is opgedeeld in drie lagen: in de "core"- en "metro"-netwerken wordt de ruggengraat van het Internet gevormd, terwijl de "access"-netwerken de toegang ("last-mile") voor de klanten verschaffen. Traditioneel werden deze netwerken uitgerold op de reeds bestaande telefonie- (via getwiste koperbedrading) of televisienetwerken (via coaxiale distributie). De immense groei in netwerkverkeer heeft er echter voor gezorgd dat laatstgenoemde de knelpunten vormen bij het aanbieden van hogesnelheidsverbindingen aan de klant. Verschillende telecom-operatoren zijn daarom geleidelijk aan begonnen aan de uitrol van glasvezel, waardoor op termijn een "Fiber-to-the-Home (FTTH)" situatie ontstaat, waarbij de eindgebruikers rechtstreeks via glasvezel met het netwerk verbonden zijn.

Het gebruik van passieve optische netwerken (PON) is vitaal voor een kosteneffectieve uitrol van glasvezel. In dergelijke netwerken wordt de "feed-fiber" van de optische lijnterminal (OLT) passief gesplitst en verdeeld tussen verschillende optische netwerk-eenheden (ONUs). De communicatieverdeling tussen eindgebruikers kan gerealiseerd worden in het golflengtedomein ("wavelength-division multiplexed PON" of WDM-PON) of in het tijdsdomein ("time-division multiplexed PON" of TDM-PON). Deze twee technieken worden vaak gecombineerd, wat dan resulteert in een "time-wavelength division multiplexed PON" of TWDM-PON.

Het resulterende "time-division-multiple access (TDMA)" medium dat onstaat door upstream communicatie in deze passieve optische netwerken introduceert echter vele uitdagingen bij het ontwerp van deze burst-mode opto-elektronische ontvangers, omdat de versterking en DC-offset moeten bijgeregeld worden van de ene burst op de andere. Om de overhead te beperken moet dit zeer snel gebeuren, terwijl communicatie tussen eindgebruikers ten allen tijde gegarandeerd moet kunnen worden, ook in het geval van zeer variërende burst-sterktes. Daarnaast moet de ontvanger linear zijn indien complexere modulatieformaten of elektronische dispersiecompensatie worden toegepast. De ontwikkeling van dergelijke lineaire burst-mode opto-elektronische ontvangers vormt het hoofdthema van dit proefschrift.

Hoofdstuk 2 beschrijft de relevante terminologie en geeft een overzicht van de specificaties die vooropgelegd worden in de verschillende PON-standaarden, die nodig zijn voor de ontwikkeling van dergelijke burst-mode OLT-ontvangers. Nadien volgt een overzicht van verschillende architecturen die geschikt zijn voor burst-mode data-ontvangst, waarbij aandacht besteed wordt aan "single-ended" naar differentiële conversie, automatische DC-offset controle (AOC) en automatische versterkingscontrole (AGC) . Deze technieken worden gebruikt as leidraad bij het ontwerp van twee verschillende burst-mode ontvangers (BMRXs) die vervolgens in dit proefschrift besproken worden.

Hoofdstuk 3 beschrijft uitvoerig de werking en performantie van een eerste-generatie lineaire BMRX, waarbij de AOC en AGC geïmplementeerd zijn in hun meest-eenvoudige vorm, namelijk via een opzoektabel waarbij instellingen (geoptimaliseerd voor een welbepaald burstvermogen) voor de AOC en AGC ingeladen worden bij het begin van elke burst. Door uitgebreide configuratiemogelijkheden en het uitwendig maken van signalen zoals de burst-startindicatie (SOB) en referentie-drempelwaarden voor het detecteren van het burstvermogen, kan de ontvanger gebruikt worden om inzichten te verwerven in de uitdagingen betreffende burst-mode transmissie. De ontvanger is gekarakteriseerd in een rechtstreekse optische verbinding waarbij geopteerd werd voor 25 Gbit/s "non-return to zero (NRZ)" modulatie met behulp van een Mach-Zehnder modulator (MZM). De bit-fout-probabiliteit (BER) werd hierbij geëvalueerd in zowel continue als burst-mode transmissie. Daarnaast werd de lineariteit van de ontvanger geëvalueerd via "4-level pulse amplitude modulation (PAM-4)" signalen aan 50 Gbit/s. Tijdens de experimenten behaalde de ontvanger een gevoeligheid van -13.8 dBm voor NRZ en -5.4 dBm voor PAM-4 en een dynamisch ingangsbereik van 17.7 dB voor NRZ en 10.9 dB voor PAM-4 (waarbij een foutprobabiliteitsgrens van 1% vooropgesteld werd bij gebruik van een "low-density-parity-check (LDPC)" foutcorrigerende code). Daarnaast werd een quasi-verwaarloosbare impact van < 0.6 dB op de gevoeligheid vastgesteld wanneer een zwakke burst voorafgegaan werd door een heel sterke. Het volledig instellen van de ontvanger duurt 48 ns.

In Hoofdstuk 4 wordt een tweede, volledig uitgeruste lineare BMRX beschreven voor 25 Gbit/s NRZ of 50 Gbit/s PAM-4 transmissie. In tegenstelling tot de vorige ontvanger wordt de versterking en DC-offset in de verschillende versterkers geregeld via continue regelkringen die zich instellen aan de start van elke burst. Om dit te verwezenlijken wordt voor de AOC en AGC gebruik gemaakt van zowel feedforward-technieken (waarbij een snelle responstijd gehaald kan worden) als feedback-technieken (die uitblinken in het halen van hoge precisie). De lussen worden aangestuurd door snelle detectie van het gemiddelde en de RMS-waarde van het ingangssignaal. Daarnaast worden bemonsterings-condensatoren gebruikt voor het vasthouden van de regimewaarde van elke regellus tijdens het finale deel van elke burst (waarbij de eigenlijke datatransmissie geschiedt). Door deze technieken te gebruiken, geraakt men af van de afweging tussen een snelle insteltijd enerzijds, en een modulatie van versterking en DC-offset tijdens het kritische deel van de burst anderzijds. Aan de ontvanger werden daarnaast verschillende circuits toegevoegd voor de detectie en het naar buiten brengen van controlesignalen die het start en einde van een burst aanduiden. Net zoals voordien werd een rechtstreekse optische link gebruikt voor de karakterisatie van de ontvanger, waarbij zowel continue- als burst-mode transmissie getest werd. Ten opzichte van de eerste ontvanger heeft deze ontvanger een verhoogde gevoeligheid (−18.1 dBm voor NRZ-modulatie en −15.8 dBm voor PAM-4-modulatie), een breder dynamisch ingangsbereik (21.6 dB voor NRZ-modulatie en 15.8 dB voor PAM-4 modulatie), een "loud-soft" penalty van < 0.9 dB, en een sterk gereduceerd dynamisch uitgangsbereik (<1.4 dB voor NRZ-modulatie en <2.0 dB voor PAM-4 modulatie). Daarenboven blijft in al deze condities de ontvanger lineair. De maximale adaptatietijd voor de AGC/AOC instellussen is instelbaar en bedraagt maximaal 82.7 ns, waarna hun waarde vastgehouden wordt door de bemonsteringscondensatoren.

In Hoofdstuk 5 wordt de ontvanger uit Hoofdstuk 3 gebruikt in een optisch link-experiment waarbij een direct gemoduleerde "distributed feedback laser (DFB)" en een optische halfgeleiderversterker (SOA) aan de ONU-verzendzijde geplaatst wordt samen met een glasvezel kabel van welbepaalde lengte. Data-transmissie aan snelheden van 25 Gbit/s over deze link is zeer uitdagend, in het bijzonder bij complexere modulatieformaten zoals PAM-4. In dit geval is elektronische dispersiecompensatie (EDC) (egalisatie) vereist om het optische link-budget te verhogen. Een equalizer met een aantal vast ingestelde gewichten kan gebruikt worden om bv. de bandbreedtebeperking te compenseren die geïntroduceerd werd door een APD-fotodiode, maar dergelijke equalizers kunnen slechts volledig benut worden wanneer een burst-mode equalizer (BMEQ) gebruikt wordt waarvan de parameters kunnen ingesteld worden aan het begin van elke burst. In dit hoofdstuk komen verschillende aspecten rond dergelijke burst-mode egalisatie aan bod door "offline post-processing", zoals de beperking van de trainingsduur en faseveranderingen die optreden tussen verschillende bursts.

Hoofdstuk 6 concludeert dit proefschrift en vergelijkt de behaalde resultaten van de twee burst-mode ontvangers met de huidige state-of-the-art. Naast PON-applicaties kunnen de ontvangers ook gebruikt worden in optische "packet-switching" netwerken die o.a. gebruikt worden in datacenters, waarbij een korte insteltijd primeert over een groot dynamisch ingangsbereik. Daarnaast werd reeds een proefbord ontwikkeld met een APD-fotodiode: voor dit prototype dienen nog metingen uitgevoerd te worden in een gelijkaardige proefopstelling als die in Hoofdstuk 5. Door gebruik te maken van een APD-fotodiode wordt de gevoeligheid drastisch verhoogd, zodat de resultaten beter aansluiten bij de specificaties vooropgesteld door de verschillende PON-standaarden. Tenslotte kunnen de verworven inzichten uit Hoofdstuk 5 gebruikt worden bij de implementatie van een real-time BMEQ, waarbij de equalizer getraind wordt door een on-chip adaptatie-algoritme bij de start van elke burst.

English Summary

Over the past few decades, the Internet has gradually evolved into a global medium used by people all over the world. As society has become highly dependent on this network and new services are added every day, global network traffic is booming.

The Internet has been layered into three tiers: the core and metro networks form the backbone of the Internet, whereas the access networks provide the last-mile to the customers. Traditionally, the access networks were built on top of the already existing telephony (using twisted-pair copper wiring) and television (using coaxial cable) distribution networks. However, the tremendous growth in IP traffic has rendered these last-mile access networks the bottleneck into providing high-bandwidth data connections. Increasingly larger portions of the access network are therefore being replaced with optical fiber, eventually reaching a Fiber-to-the-Home (FTTH) situation, in which end-users directly connect to an optical network.

The use of passive optical networks (PONs) is paramount to achieve a cost-effective deployment of FTTH. In these networks, the feeder fiber from the optical line terminal (OLT) is split and shared passively amongst many optical network units (ONUs). Multiplexing multi-user transmission is then realized in the wavelength-domain (wavelength-division multiplexed PON or WDM-PON) or in the time-domain (time-division multiplexed PON or time-division multiplexed PON (TDM-PON)). Typically, different TDM-PONs are combined using multiple wavelengths, resulting in a combined time-wavelength division multiplexing PON (TWDM-PON).

The resulting time-division multiple access (TDMA) medium created through upstream direction in these single-wavelength TDM-PONs introduces many challenges for the burst-mode opto-electronic receivers, as they need to adapt their internal gain and offset on a burst-to-burst basis. To reduce the overhead, this needs to happen as quickly as possible while ensuring reliably transmission with wildly varying optical burst powers. In addition, to support the use of multi-level modulation formats and electronic dispersion compensation, the receiver needs to be linear. The development of these linear burst-mode receivers form the major topic of this thesis dissertation.

Chapter 2 presents the required terminology and specifications imposed by next-generation PON standards needed for the development of high-rate burst-mode OLT receivers. Then, different burst-mode architectures are proposed, with emphasis on quick single-ended to differential conversion, automatic-offset-control (AOC) and automatic-gain-control (AGC). They are used as a starting point in the development of two burst-mode receivers.

Chapter 3 describes in detail the operation and performance of a first-generation linear burst-mode receiver (BMRX) design, where AOC and AGC have been implemented in one of its most basic forms; i.e. through a simple look-up table (LUT) which selects the appropriate AOC and AGC settings at the start of each burst, which are optimized for a specific burst power level. Through extensive configuration options and externalizing signals such as the SOB and power threshold reference signals, the BMRX can be used to gain insights in the different challenges in burst-mode transmission. The receiver is characterized in a back-to-back experiment at 25 Gbit/s non-return-to-zero (NRZ) with idealized Mach-Zehnder-modulator (MZM) modulation to evaluate the bit error rate (BER) performance in both continuous- and burst-mode. In addition, the linearity of the receiver is evaluated by performing a 4-level pulse amplitude modulation (PAM-4) transmission experiment at 50 Gbit/s. In the experiments, the receiver achieves a sensitivity level of −13.8 dBm for NRZ and −5.4 dBm for PAM-4, while an input dynamic range of at least 17.7 dB for NRZ and 10.9 dB for PAM-4 is obtained (at the low-density parity check (LDPC) forward error correcting (FEC) threshold of 1×10^{-2}). A negligible power-penalty of < 0.6 dB is observed for weak bursts following a strong preceding burst. The settling time is measured as 48 ns.

Chapter 4 describes a second, fully-featured linear BMRX, capable of operating at 25 Gbit/s NRZ or 50 Gbit/s PAM-4. As opposed to before, the gain of the post-amplifier stages and DC-offsets of the datapath can be quickly adjusted in a continuous manner from one burst to the next through combined feedforward (providing rapid settling) and feedback (providing accurate gain and offset control) AGC and AOC loops. Both are driven by rapid detection of average and root-mean-square (RMS)-values of the input signal. In addition, sample-and-hold capacitors are used to fix the state of the AGC and AOC loops during the payload section of each burst, to eliminate the trade-off between settling time and power penalties caused by gain modulation and/or baseline wander. Several circuits were added to detect and interface the SOB and EOB signals. Similarly as before, the receiver is characterized in back-to-back experiment featuring MZM modulation, both in continuous- and in burst-mode. Compared to Chapter 3, the receiver has an improved sensitivity level (−18.1 dBm for NRZ and −11.4 dBm for PAM-4), a wider input dynamic range (21.6 dB for NRZ and 15.8 dB for PAM-4), a loud-soft power penalty of < 0.9 dB, and a near-zero output dynamic range (<1.4 dB for NRZ and <2.0 dB for PAM-4), all while maintaining linear operation. The AGC/AOC loops are allowed a (configurable) maximum settling time of 82.7 ns, at which point they are fixed using the sample-and-hold capacitors.

In Chapter 5, the developed receiver described in Chapter 3 is used in an experimental setup, together with a directly modulated distributed feedback (DFB) laser and a semiconductor optical amplifier

(SOA) at the ONU transmit side, in combination with a significantly long section of fiber. Because these components introduce severe bandwidth limitations and dispersion, transmission at 25 Gbit/s and beyond is very challenging, in particular for multilevel modulation formats such as PAM-4. As such, some form of electronic dispersion compensation (EDC) (equalization) is needed to increase the optical power budget. A fixed-tap equalizer can be used to compensate the bandwidth of e.g. the avalanche photodiode (APD) at the receive side only, but its full potential can only be realized by using a burst-mode equalization (BMEQ) which adapts the equalizer parameters on a burst-to-burst basis. In this chapter, we analyze the different aspects of such a conceptual burst-mode feedforward equalizer (FFE)/decision-feedback equalizer (DFE) equalizer by using offline post-processing, to establish specific burst-mode equalizer penalties and trade-offs such as limited training time and burst-to-burst phase variation.

The final chapter concludes and summarizes the work performed and compares the performance of the two developed receivers to the current state-of-the-art. Besides PON applications, the receivers can also be used in optical packet switching networks, where short settling times are preferred over a wide input dynamic range. In addition, a fabricated APD-assembly is yet to be tested in a directly modulated link setup such as the one described in Chapter 5, promising a higher sensitivity, which is needed by current PON standards. Finally, the insights on burst-mode equalization can be used in the development of a first real-time BMEQ, where the equalizer is trained using an on-chip adaptation algorithm at the start of each burst.

List of Publications

Publications in International Journals

- **G. Coudyzer**, P. Ossieur, J. Bauwelinck, and X. Yin, “A 50 Gbit/s PAM-4 Linear Burst-Mode Receiver with Analog Gain- and Offset Control in 0.25 µm SiGe:C BiCMOS,” *IEEE Journal of Solid State Circuits*, Sept. 2019 [Submitted].
- **G. Coudyzer**, P. Ossieur, L. Breyne, A. La Porta, S. Paredes, J. Bauwelinck, and X. Yin, “Study of Burst-Mode Adaptive Equalization for >25G PON Applications [Invited],” *Journal of Optical Communications and Networking*, June 2019.
- **G. Coudyzer**, P. Ossieur, L. Breyne, M. Matters, J. Bauwelinck, and X. Yin, “A 50 Gbit/s PAM-4 Linear Burst-Mode Transimpedance Amplifier,” *IEEE Photonics Technology Letters*, vol. 31, no. 12, pp. 951–954, June 2019.
- B. Moeneclaey, F. Blache, J. Van Kerrebrouck, R. Brenot, **G. Coudyzer**, M. Achouche, X.-Z. Qiu, J. Bauwelinck, and X. Yin, “40-Gb/s TDM-PON Downstream Link With Low-Cost EML Transmitter and APD-based Electrical Duobinary Receiver,” *IEEE Journal of Lightwave Technology*, vol. 35, no. 4, pp. 1083–1089, 2017.

Publications in International Conferences

- X. Yin, J. Lambrecht, **G. Coudyzer**, J. Verbist, H. Ramon, P. Ossieur, G. Torfs, and J. Bauwelinck, "Electronic Circuits for High Speed PON Beyond 25G," *2019 Optical Fiber Communications Conference and Exhibition (OFC)*, 2019, pp. 1–3. pp. 951–954, June 2019.

- P. Ossieur, **G. Coudyzer**, D. Kelly, X. Yin, P. Townsend, and J. Bauwelinck, "ASIC Implementation Challenges for Next Generation Access Networks," *Advanced Photonics 2018 (BGPP, IPR, NP, NOMA, Sensors, Networks, SPPCom, SOF)*, OSA, 2018, pp. 1–2.

- X. Yin, J. Van Kerrebrouck, **G. Coudyzer**, and J. Bauwelinck, "Multi-Level High Speed Burst-Mode Receivers," *21st Optoelectronics and Communications Conference (OECC) Held Jointly with the International Conference on Photonics in Switching (PS)* 2016, pp. 1–3.

- X. Yin, F. Blache, B. Moeneclaey, J. Van Kerrebrouck, R. Brenot, **G. Coudyzer**, M. Achouche, X.-Z. Qiu, and J. Bauwelinck, "Multi-Level High Speed Burst-Mode Receivers," *2016 Optical Fiber Communications Conference and Exhibition (OFC)*, 2016.

Patent Applications

- **G. Coudyzer** and X. Yin, "Sequence Aligner for Synchronizing Data,", European Patent Application EP3297205A1, Sept. 09, 2016

1

Introduction

Over 50 years ago, a project was initiated by the U.S Advanced Research Projects Agency (ARPA) [1] which enabled four university mainframe computers to communicate with each other, allowing the exchange of scientific research data. Back then, no one would have thought that that the so-called ARPANET would grow into a network of over 18 billion interconnected devices [2], which we now call the Internet. Driven by enterprise companies such as Microsoft, Amazon, Google, Netflix and many more, the Internet has totally changed the way we live. Internet has become more than its bare bitrate-capacity: we communicate through instant messages, public blogs and vlogs, Twitter tweets and even hashtags (thank Instagram for that one). Just about anything can be bought online: regular shopping, but also take-away and even groceries. And the steady decline -and, ultimately, demise- of vinyl and CD sales proves the popularity of on-demand, a la carte, audio and video streaming. And virtual reality (VR) entertainment is right around the corner.

Figure 1.1: A selection of online web services.

This ever-growing number of services goes hand in hand with the increasing demand for data bandwidth. Cisco predicts a threefold increase of global Internet Protocol (IP) traffic (which is comprised out of 80% of video traffic) from 2017 onwards to 2022, with a compound annual growth rate (CAGR) growth rate of 26 % [2]. In order to accomodate the ever-increasing demand for online connectivity, the Internet has been deployed on a communication infrastructure (shown in Fig. 1.2) which is layered into three tiers. Each tier has a different function and topology.

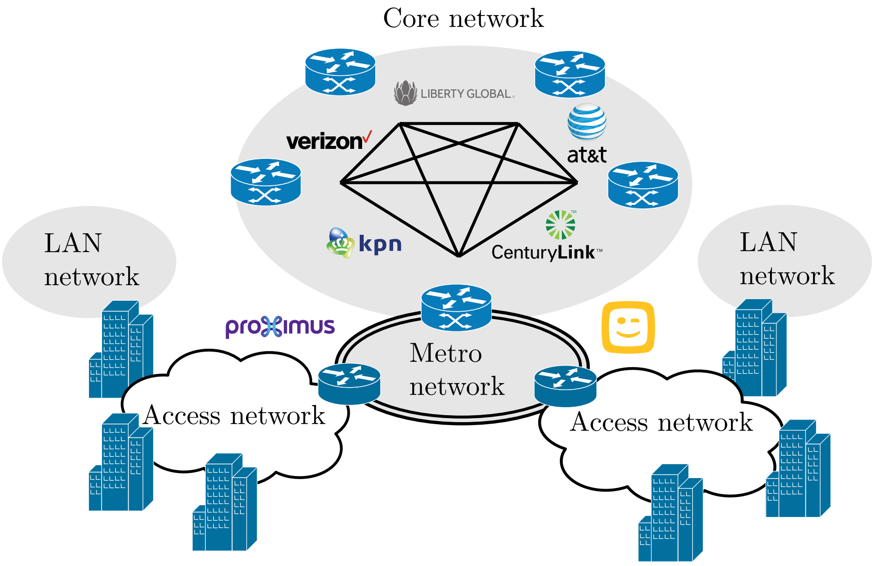

Figure 1.2: Core, metro and access tier networks.

The backbone of the Internet is found in the core network [3–5], which provides many different routes in a meshed interconnect grid to exchange information through the various sub-networks, interconnecting countries and continents together. High-end switches and routers are used to communicate data between nodes in various protocols such as the IP or Asynchronous Transfer Mode (ATM) protocol. Core networks are generally managed by companies operating worldwide, such as KPN, Verizon and Liberty Global.

The metro network (short for metropolitan) provides coverage over a limited area, spanning one or multiple cities. These are the networks managed by the different Internet service providers (ISPs), such as Belnet, Proximus and Telenet (in Belgium), and are deployed using a ring-topology. Both core and metro networks are implemented using state-of-the-art dedicated fiber optic links and (dense) wavelength division multiplexing (DWDM), enabling multi-Terabit/s communication over large distances.

Access networks provide the last-mile towards the end customer. Traditionally, these networks were built on top of the already existing telephony (using twisted-pair copper wiring) and television (using coaxial cables) distribution networks. However, the tremendous growth in IP traffic has rendered these last-mile access networks the bottleneck into providing high-bandwidth data connections. In addition, as more and more traffic migrates from intra-datacenter communication to access networks [6], large changes in the infrastructure are necessary.

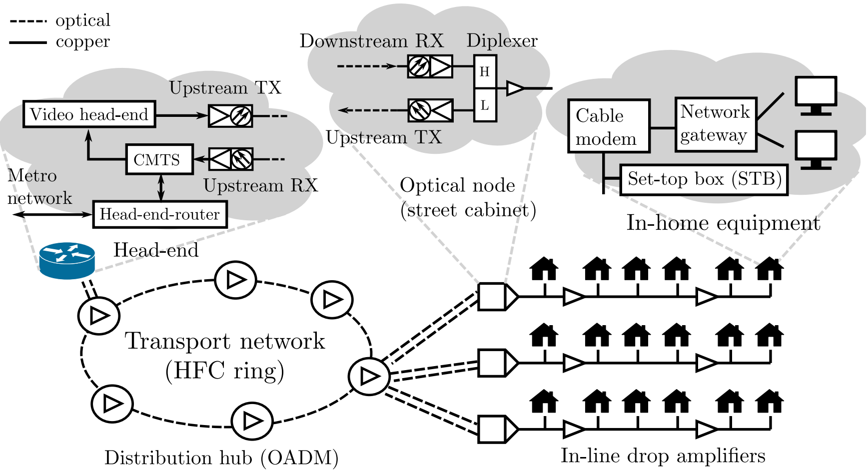

Figure 1.3: The HFC access-network.

The coaxial distribution network gradually evolved into what is now known as the Hybrid Fiber-Coax (HFC)-network, shown in Fig. 1.3. Here, data is transmitted across an optical fiber ring, using optical add-drop multiplexers (OADMs) and coarse wavelength division multiplexing (WDM) to provide connectivity to the different optical nodes [7, 8]. The last-mile remains implemented using coaxial cable. Upstream and downstream transmission is modulated using quadrature amplitude modulation (QAM) on different frequency bands, requiring bidirectional drop amplifiers and diplexers. In order to increase the capacity, higher-order QAM and orthogonal frequency division multiplexing (OFDM) are used to increase the throughput. In DOCSIS 3.1 for example [9], 4096-QAM is used, to support up to 1.89 Gbit/s per 192 MHz channel.

The telephony network, shown in Fig. 1.4 now uses optical fiber as a feed line into the remote optical platform (ROP). This Fiber-to-the-Curb (FTTC) arrangement provides sufficient capacity up until the street cabinet. To increase the capacity between the ROP and customer premises equipment (CPE), Assymetric Digital Subscriber Line (ADSL) is being phased out and replaced with Very-high-bit-rate Digital Subscriber Line (VDSL) and VDSL2 [10], which uses bandwidths up to 12 MHz on the twisted-pair copper wires to provide data rates exceeding 100 Mbit/s. This is done through dynamic line management (DLM) and the use of vectoring, in which the far-end crosstalk (FEXT) is actively canceled [11].

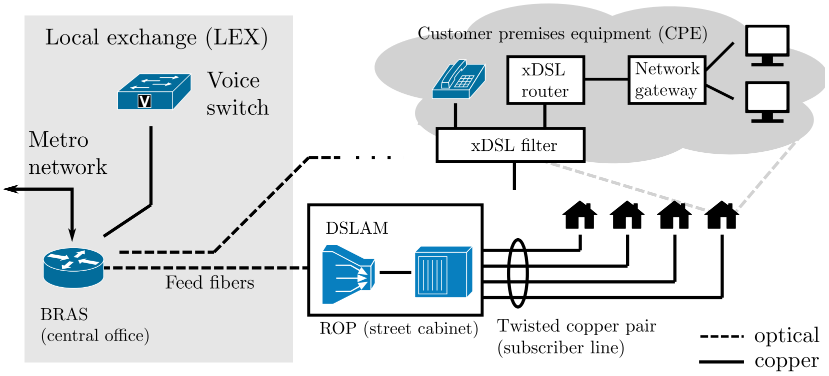

Figure 1.4: The Digital Subscriber Line (DSL) access-network.

It becomes clear that increasing the data rate capacity even further will become exceedingly difficult. This is why FTTH or Fiber-to-the-Building (FTTB) is proposed to keep up with the ever-growing demand for bandwidth. Here, the optical fiber is extended to cover the last-mile towards the CPE. Still, the deployment of these networks require significant infrastructural changes.

In large regions with few telecommunication operators this transition goes quite smoothly: Asia for example, currently leads the

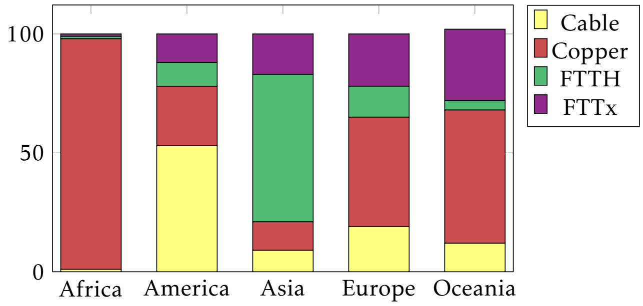

Figure 1.5: Technology market share by region in Q3, 2017 [13].

FTTH-market with a market share of over 60%, as shown in Fig. 1.5. Telecommunications in Europe on the other hand, are managed per country by one or more telecommunication operators, resulting in hundreds of different operators, each having to upgrade their infrastructure. To promote and accelerate the deployment of FTTH in these countries, the European FTTH council [12] was founded. Each year, it publishes the top-tier FTTH coverage in European countries, which for 2017 is shown in Fig. 1.6.

Note in this figure the abscense of several countries, including the author's country of origin, Belgium: Here, the last-mile still uses the legacy copper and twisted-pair access networks. By 2026, Proximus plans to provide at least 50% FTTH coverage [15]. Telenet will keep using its existing coaxial infrastructure, with addition of FTTH projects for selected places.

The European Commision promotes the deployment of FTTH networks, promising at least 1Gbps for schools, universities and research centres, and at least 100Mbps (upgradable to 1Gbps) for all European households by 2025 [16]. Nevertheless, deploying FTTH remains very challenging, especially due to the sheer number of fibers required to provide a dedicated line to each customer. To overcome this challenge, passive optical networks are proposed as a cost-effective way of deploying FTTH and FTTB. In such a network (conceptually shown in Fig. 1.7), a single fiber is split and shared amongst many end-users.

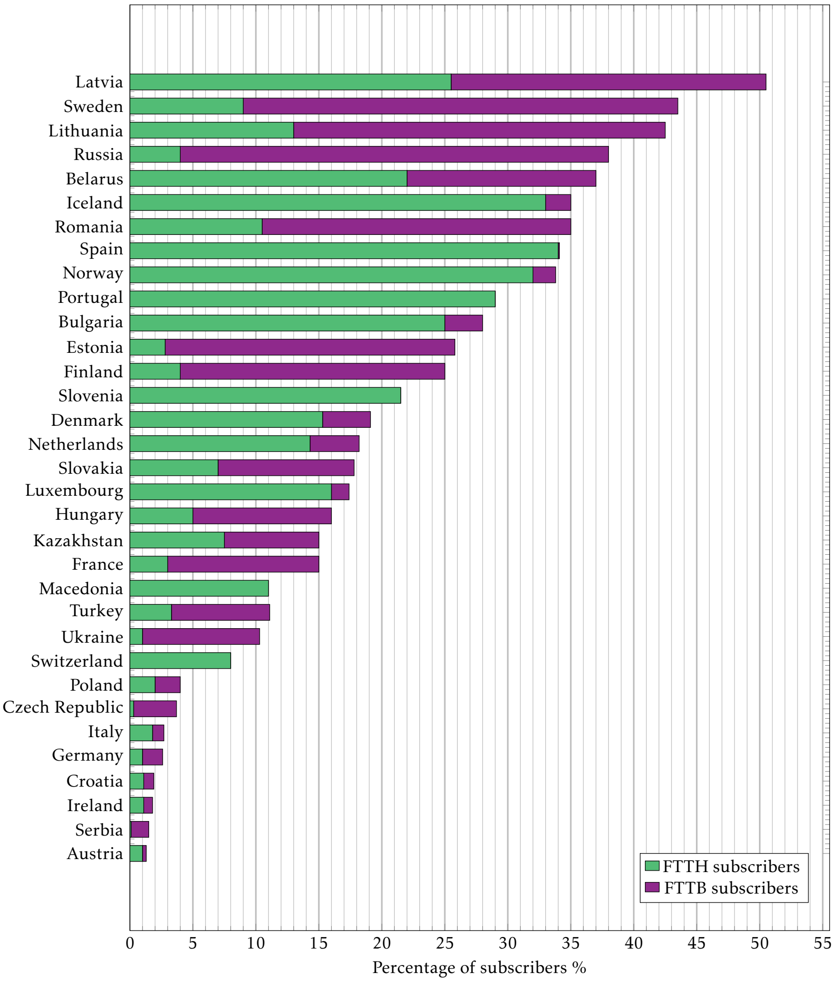

Figure 1.6: FTTH coverage in European countries on September 2017 (with more than 1% coverage) [14].

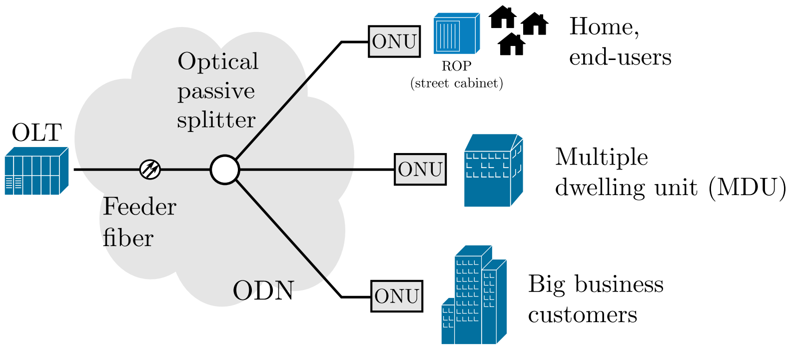

Figure 1.7: Conceptual illustration of a PON.

Here, the OLT can play the role of a ROP (Fig. 1.4) or replace the optical nodes (Fig. 1.3), while the different ONUs are the end-users of the PON network. The optical distribution network (ODN) is defined as the fiber network inbetween both.

In Fig. 1.8 an overview is given of different access techniques including different PON FTTH standards, in addition to Nielsen's law, which estimates that a high-end user's connection speed grows by 50% per year [17]. Should we believe the promises of the European FTTH Council and this law, we can rest assured that multi-gigabit, optical fiber Internet connections will be available for most households in a few years.

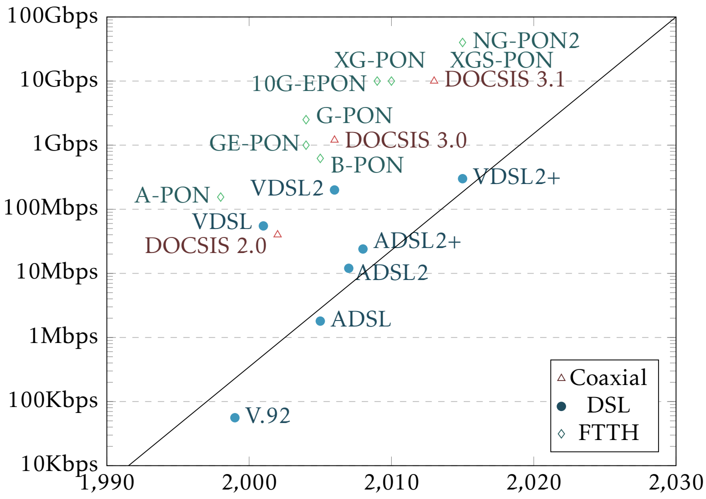

Figure 1.8: Bandwidth evolution in the access network [18].

1.1 Outline of this Dissertation

This chapter defined the basic concepts of the different access networks typically being used nowadays. In the future, these networks will be gradually augmented (and eventually replaced) with FTTH and FTTB, deployed in the form of passive optical networks.

In the next chapter, we delve into how different users communicate over these passive optical networks: user multiplexing is done in either the wavelength domain (wavelength-division multiplexed PON or WDM-PON), in the time domain (time-division multiplexed PON or TDM-PON), or both. In addition, we look at the requirements for receivers at the OLT side, which will need to operate in burst-mode.

The development of these burst-mode receivers form the major topic of this dissertation. In Chapter 3 and Chapter 4 two burst-mode receivers are described and characterized. They are tested with 25 Gbit/s NRZ bursts, as well as 50 Gbit/s PAM-4 bursts to evaluate their linearity. The first receiver implements AOC/AGC through a LUT, whereas the second-generation receiver uses full analog AOC/AGC instead.

In Chapter 5, the developed receiver from Chapter 3 is used in an experimental optical link setup using low-cost optical components and a portion of fiber of significant length, mimicking actual PON upstream transmission. We look at the different optical link budget penalties introduced by the severe bandwidth limitations and dispersion, which requires electronic (dispersion) compensation using e.g. a FFE/DFE equalizer. Here, the different aspects of such a burst-mode equalizer are investigated, to establish design criteria for future real-time burst-mode equalizers.

The final chapter concludes and summarizes the work performed and compares the perfomance of the two developed receivers to the current state-of-the-art.

References

[1] T. SearchNetworking. (2017) Definition of arpanet. [Online]. Available: https://searchnetworking.techtarget.com/definition/ARPANET

[2] Cisco. (2019) Cisco visual networking index: Forecast and trends, 20172022 white paper. [Online]. Available: https://www.cisco.com/c/en/us/solutions/collateral/service-provider/visual-networking-index-vni/white-paper-c11-741490.html

[3] Techopedia. Core network - definition. [Online]. Available: https://www.techopedia.com/definition/6641/core-network

[4] C. Solutions. Ip core/edge networks. [Online]. Available: http://www.commverge.com/Solutions/IPCoreEdgeNetworks/tabid/153/Default.aspx

[5] C. Telecommunications. Core network layer: Explained. [Online]. Available: http://www.carritech.com/news/core-networks/

[6] A. Rebatta. End-user traffic rising, more traffic migrating to private networks. [Online]. Available: https://blog.telegeography.com/end-user-traffic-rising-more-traffic-migrating-to-private-networks

[7] T. Koch, *Optical Fiber Telecommunications IIIA*, ser. Optics and Photonics. Elsevier Science, 2012.

[8] T. Rokkas, D. Katsianis, and D. Varoutas, “Techno-economic evaluation of fttc/vdsl and ftth roll-out scenarios: Discounted cash flows and real option valuation,” *Optical Communications and Networking, IEEE/OSA Journal of*, vol. 2, pp. 760 – 772, 10 2010.

[9] CableLabs. Docsis3.1. [Online]. Available: https://www.cablelabs.com/innovations/docsis-3-1

[10] ITU-T Recommendation G.993.1. (2012) Very high speed digital subscriber line transceivers (VDSL). [Online]. Available: https://www.itu.int/rec/T-REC-G.993.1/en

[11] ITU-T Recommendation G.993.5. (2012) Self-FEXT cancellation (vectoring) for use with VDSL2 transceivers. [Online]. Available: https://www.itu.int/rec/T-REC-G.993.5/en

[12] FTTH Council Europe. (2019). [Online]. Available: https://www.ftthcouncil.eu/

[13] P. Topic. World broadband statistics q3 2017. [Online]. Available: http://point-topic.com/free-analysis/world-broadband-statistics-q3-2017/

[14] R. Montagne, “Ftth conference 2018 - ftth/b panorama.” [Online]. Available: https://www.ftthcouncil.eu/documents/IDATE_European_FTTH_B_panorama%20_at_Sept_2017_VF.pdf

[15] C. Fiber. Proximus prepares for 50https://comsof.com/fiber/cases/proximus-prepares-for-50-ftth-coverage-by-2026/

[16] E. Commission, “Broadband europe.” [Online]. Available: https://ec.europa.eu/digital-single-market/en/broadband-europe

[17] J. Nielsen. Nielsen’s law of internet bandwidth. [Online]. Available: https://www.nngroup.com/articles/law-of-bandwidth/

[18] K. Casier, “Techno-economic evaluation of a next generation access network deployment in a competitive setting,” Ph.D. dissertation, Ghent University, 2009.

2

Passive Optical Networks and Burst-Mode Receivers

This chapter discusses some important fundamental concepts and terminology related to passive optical networks (PONs). Some of the major PON network types are described, distinguishing between wavelength-division multiplexed PON (WDM-PON), time-division multiplexed PON (TDM-PON) and time-wavelength division multiplexing PON (TWDM-PON). Then, an overview of the different standards is given, together with some of their key specifications (including optical power budget, wavelength allocation, error correction schemes and security aspects). In the second half of this chapter different burst-mode receiver architectures are desribed, with emphasis on AOC and AGC.

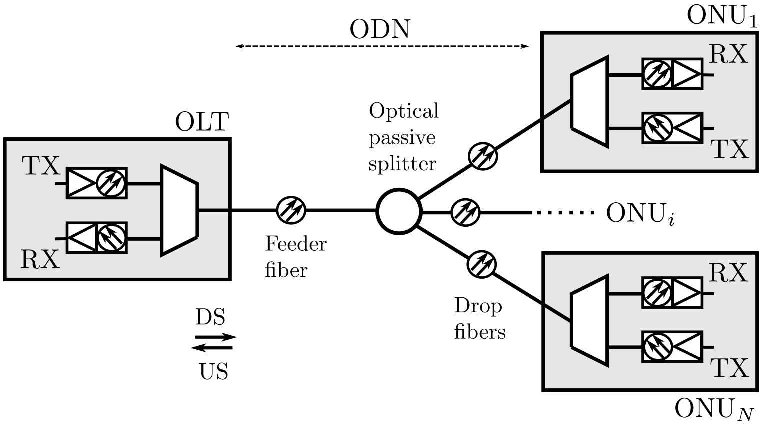

Figure 2.1: A conceptual passive optical network.

2.1 Passive Optical Networks

In its most basic form, a PON can be illustrated as shown in Fig. 2.1. Here, the OLT (typically located at the central office) is connected to different ONUs using an optical passive splitter. The ODN is a passive network of optical fiber and splitters, designed to reach as many ONUs as possible, to lower the deployment cost. This however requires that many users communicate over a single fiber, which requires (de)multiplexing techniques on both sides. In general, this (de)multiplexing can be done in the time-domain and/or the frequency/wavelength-domain [1].

Wavelength Division Multiplexed PON

In wavelength-division multiplexed PON (WDM-PON), downstream (DS) and upstream (US) communication channels are established over different wavelengths for each subscriber. These different wavelengths can be separated from each other using an arrayed waveguide grating (AWG), as shown in Fig. 2.2. This way, point-to-point (P2P)-connections are possible using a simple medium access control (MAC)-interface.

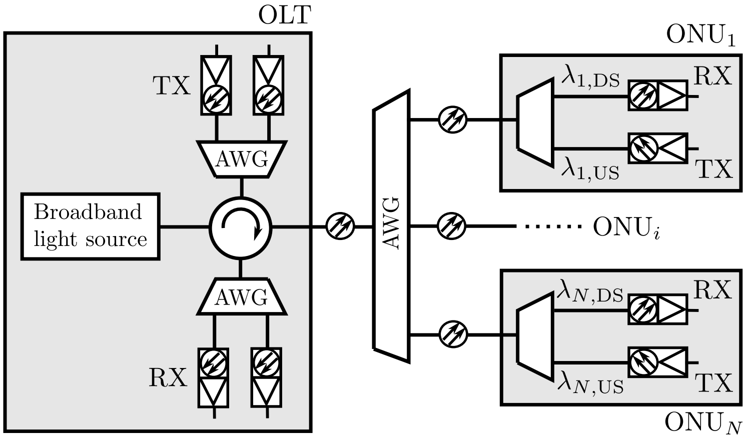

Figure 2.2: Architecture of a wavelength-division multiplexed PON (WDM-PON).

However, because the OLT must transmit precisely on many different wavelenghts, expensive tunable lasers (or a broad array of fixed-wavelength lasers) are required. This is why typically a broadband light source is used to generate a broad spectra of wavelengths, which is then spectrally sliced using the AWG. Injection-locked lasers at the OLT and ONU then use these seed wavelengths to establish different optical channels.

Time Division Multiplexed PON

In a time-division multiplexed PON (TDM-PON), traffic between the ONU and OLT is separated into different optical packets, which are then transmitted at various time slots across the ODN. TDM-PON networks typically rely on coarse WDM to separate the network in an DS channel and an US channel [2].

DS traffic originating from the central office OLT to the end-users ONUs is performed through broadcasting. The ONUs monitors the channel and only processes datapackets meant for that specific ONU. As a result, the ONU receives data using simple, continuous-mode receivers.

US traffic from the end-users back to the central office OLT on the other hand, require that different ONUs access the optical network at non-overlapping time slots (also known as TDMA). This requires a degree of coordination in which the OLT signals when certain ONUs are allowed to transmit. This results in bursty traffic at the OLT receiver, as shown in Fig. 2.3.

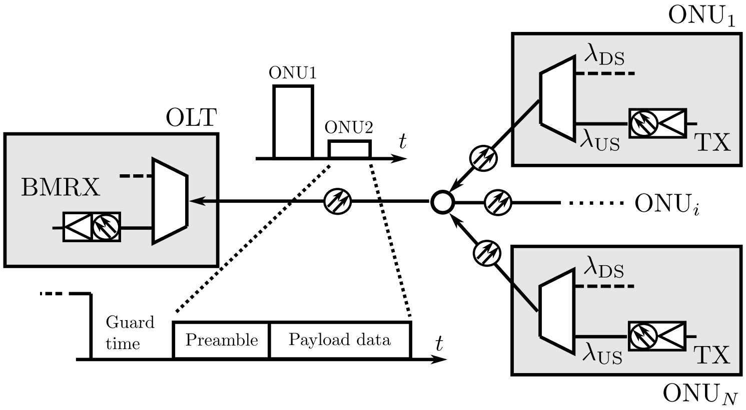

Figure 2.3: Upstream data transmission in a TDM-PON.

In addition, the individual bursts arrive at the OLT with significant power variations (> 20 dB optical) and an unpredictable phase, separated by only a small guard time (e.g. 25.6 ns). This requires the OLT receiver to adapt its internal parameters (such as gain and differential output offset voltage) on a burst-to-burst basis, while minimizing the required settling time in order to reduce preamble overhead. This thesis dissertation focuses on the development of these burst-mode receivers, starting with a more detailed discussion on the received signal in Section 2.3.

Time-Wavelength Division Multiplexed PON

TWDM-PONs have been proposed as an effort into increasing the capacity of conventional PON-networks, by splitting the US and DS wavelengths into multiple individual channels, while still employing time division multiplexing (TDM) within each channel. This guarantees the maximum usage of the available infrastructure. In addition, the flexibility of TWDM-PON allows multiple services to be aggregated onto a single wavelength, isolating applications from one another [3].

Standardization Efforts and Milestones

The many different methods of deploying PON have evolved over the years, driven by optical equipment manufacturers and service providers. Back in 1995, the Full Service Access Network (FSAN) consortium was founded by 7 telecommunication providers in order to study the feasibility of extending fiber optics access to end users [1]. Its main purpose was to build industry consensus around access networking technologies. Their member companies brought significant contributions to the ITU-T study group, which defines standards for PON (see Fig. 2.4). In parallel, the IEEE developed its own set of standards, extending its widely-known standards for Ethernet for optical access networks. Whereas ITU-T is driven by the operators (leading to standards based on well established components), IEEE defines its network specifications based on more recent innovations, leading to more relaxed requirements, to allow early adoption of these systems. Table 2.1 summarizes the most important standards, its type and their DS and US data-rates.

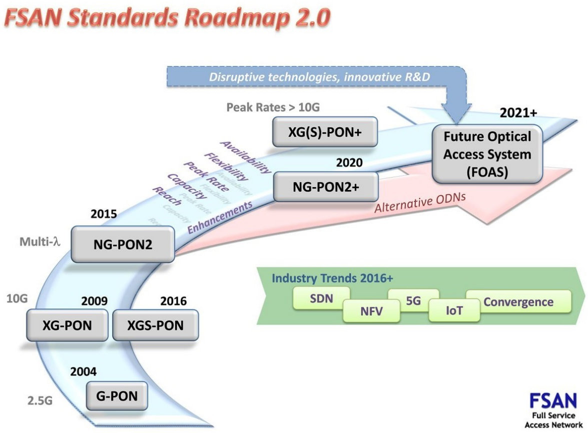

Figure 2.4: The FSAN Standards Roadmap 2.0 [4].

Name	Release	US-Type	DS-rate	US-rate
A-PON (ITU-T G.983.1) [5]	1998	TDMPON	155Mbps	155Mbps
B-PON (ITU-T G.983 Amdt) [5]	2005	TDMPON	622Mbps	155/622Mbps
G-PON (ITU-T G.984.2) [6]	2004	TDMPON	2.5Gbps	1.25/2.5Gbps
GE-PON (IEEE 802.3ah) [7]	2004	TDMPON	1Gbps	1Gps
10G-EPON (IEEE 802.3av) [8]	2009	TDMPON	10Gbps	1/10Gbps
XG-PON (ITU-T G.987) [9]	2010	TDMPON*	10Gbps	2.5Gbps
NG-PON2 (ITU-T G.989) [10]	2015	TWDMPON	4×10Gbps	4×2.5/10Gbps
XGS-PON (ITU-T G.9807) [11]	2016	TDMPON	10Gbps	10Gbps
50G-EPON (IEEE 802.3ca) [12]	-	TWDMPON	2×25Gbps	2×25Gbps
G.hsp.50Gpmd (ITU-T) [13]	-	TDMPON	>25Gbps	>25Gbps

Table 2.1: Primary PON standards.

Whereas the initial standards focused on TDM-PON with only coarse WDM to separate downstream from upstream communications, the increasing demand for bandwidth pushed newer standards towards the use of different wavelengths, as is the case for NG-PON2 (ITU-T G.989). In this standard, 4 wavelengths are proposed, each carrying a 10/2.5G asymmetric TDM-PON link [10]. Alternatively, the IEEE 802.3ca task force proposes single-wavelength 25 Gbit/s or 50 Gbit/s channels [12] for next-generation access networks.

Actual implementation and deployment of these standards typically lag behind around 10 years. At the time of writing, the majority of products follow the G-PON and GE-PON standard (the former holding the largest market share of 85 % reported in 2017 [14]). However, it is expected that this will be reduced by almost 20 % by 2022 due to the gradual deployment of 10G-EPON and XGS-PON. Several market research reports indicate that XGS-PON will dominate the market over 10G-EPON [15, 16]. In 2020, Verizon expects to start deploying NG-PON2 in consumer applications [17]. The 50G-EPON standard is expected to be finalized in August 2020 [12], but actual deployment will take at least until 2024 [18].

In the next sections, different aspects of these networks are considered, linking them to the different standards.

Optical Power Budgets

To maximize the effectiveness of a passive optical network deployment, different ONUs must be able to connect to the network at various locations. These locations can be very far from or very close to the central OLT. In addition, different splitters can be introduced in the ODN, which increases the split factor. At the ONU side, variations in the launch power can also be observed due to the non-identical equipment and varying environment conditions. This is why standardization bodies have defined transmit and receive optical power level ranges, to which both the transmitter and receiver in the network must adhere. The different power level ranges for the most important standards are shown in Table 2.2.

Notice that the launch powers at the transmit side are often several dBm, requiring the use of directly modulated DFB lasers with large output power, and/or optical amplification using SOAs. At the receiver side, the optical powers can be very low, which favors the use of APDs or optically preamplified receivers. And huge burst-to-burst power variations are to be expected, which requires a burst-mode receiver with a very wide input dynamic range.

The numbers given in Table 2.2 can be used to establish an optical power budget, which can be distributed to accomodate a certain number of end-users (split factor) and reach (fiber loss over distance). In addition, a number of power penalties need to be added to account for:

		TX Power (dBm)		RX Power (dBm)	
Standard	ODN class	Min	Max	Sens.	Overload
A-PON [5]	Class B	-4	-2	-30	-8
	Class C	-2	4	-33	-11
B-PON [5]	Class A	-6	-1	-27	-6
	Class B	-1	4	-27	-6
	Class C	-1	4	-32	-11
G-PON [6]	Class A	-3	2	-24	-3
	Class B	-2	3	-28	-7
	Class C	2	7	-29	-8
	Class B+	1.5	5	-28	-8
	Class C+	3	7	-32	-12
GE-PON [7]	LX10	-9	-3	-19.5	-3
10G-EPON [8]	PR10	2	5	-24	-1
	PR20	5	9	-28	-6
	PR30	2	5	-28	-6
XG-PON [9]	Class N1	2	7	-27.5	-7
	Class N2	2	7	-29.5	-9
	Class E1	2	7	-31.5	-11
	Class E2	2	7	-33.5	-13
XGS-PON [19]	Class N1	4	9	-26	-5
	Class N2	4	9	-28	-7
	Class E1	4	9	-30	-9
	Class E2	FFS	FFS	FFS	FFS
NG-PON2 [10]	Class N1	2	7	-28	-7
	Class N2	2	7	-30	-9
	Class E1	2	7	-32.5	-11
	Class E2	4	9	-32.5	-11
50G-EPON [8]	(draft)	6	8	-24	0

Table 2.2: Typical upstream power levels in PONs.

- Non-ideal transmitters, introducing a transmitter dispersion penalty (TDP) (typically around 1.5 dB), in particular for directly modulated transmitters,
- Finite extinction ratios (e.g. 2 dB for an extinction ratio of 7 dB), typically worse for higher-order modulation formats,
- Crosstalk in WDM channels [20], typically occurring at the AWG: in [21] this effect is studied, relating the resulting power penalty as a function of the linear crosstalk between channels.
- Non-ideal receivers, introducing burst-mode (and loud-soft) power penalties (compared to continuous-mode) as well as power penalties due to baseline wander.

In addition to the losses in the ODN, the distance between the OLT and ONU determines the amount of dispersion introduced in the optical link. Table 2.3 summarizes the most commonly used split factor and total ODN fiber length (reach). Because dispersion is only an issue at higher baudrates, it is typically not mentioned in the older standards.

Standard	**Split-ratio**	**Reach**	**Dispersion**
A-PON [5]	1:128	20 km	
B-PON [5]	1:128	20 km	
G-PON [6]	1:128	60 km	
GE-PON [7]	1:16	10/20 km	
10G-EPON [8]	-	20 km	
XG-PON [9]	-	20/40 km	≈ 0 → 200/400 ps/nm*
XGS-PON [19]	1:64	>20 km	0 → -140 ps/nm
NG-PON2 [10]	-	20/40 km	0 → 400/800 ps/nm
50G-EPON [8]	1:32	20 km	20 ps/nm/km

* Exact value dependent on the wavelength of the channel being used.

Table 2.3: Typical values for the split-factor, reach and dispersion in several PON standards.

Wavelength Allocation and Coexistence Schemes

The fiber loss and dispersion from previous section are heavily dependent on the choice of wavelength for the transmission link. Fig. 2.5

shows the fiber loss and dispersion as a function of wavelength [22], as well as the most commonly allocated wavelengths for the most prominent standards currently available.

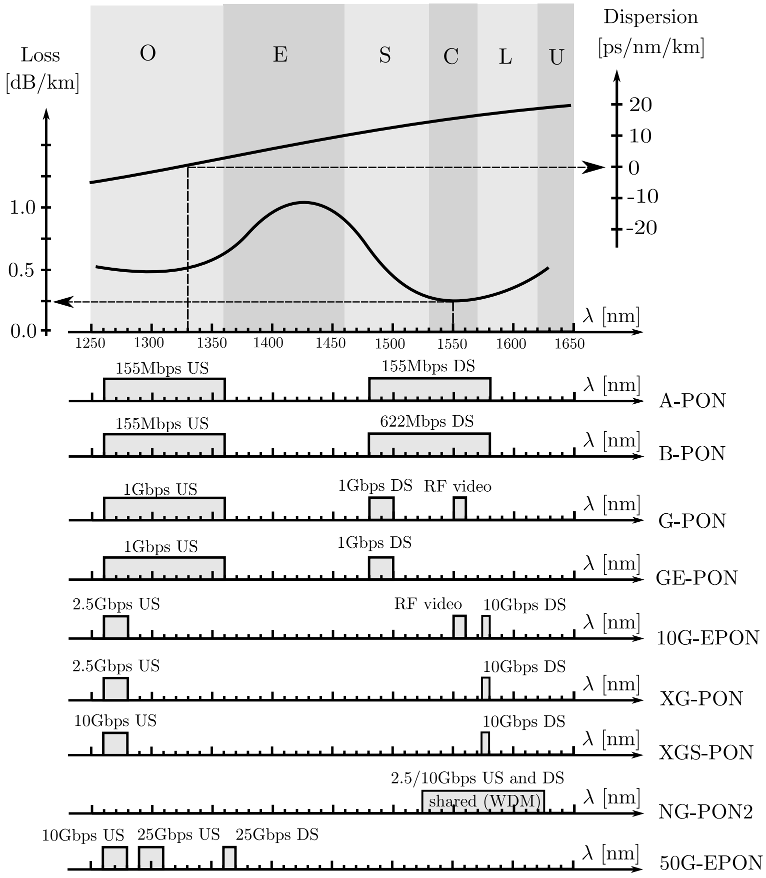

Figure 2.5: Wavelength allocation plan for different standards [23]. 50G-EPON allocations based on [24].

The presence of the two low-loss windows in the C- and O-band is widely known, as is the zero-dispersion wavelength (situated in the O-band). The allocation of wavelengths for next-generation access networks depends on these parameters, but must also take into account coexistence with existing deployments.

Notice that the 50G-EPON task force currently proposes both US and DS transmission in the O-band. This is because C-band transmission introduces severe dispersion, which is (currently) for these higher baudrates a bigger problem than the introduced excess fiber loss when choosing O-band wavelengths. The excess fiber loss can be accounted for in the power link budget, unlike the dispersion penalty.

Error Correction Schemes

As the line-rate in PONs gradually increased, so did the challenge of maintaining error free-transmission for every ONU connected to the network. Due to the increased bandwidth requirements for higher data-rate receivers, their sensitivity is often worse, which reduces the achievable input dynamic range. In addition, the effects of chromatic fiber dispersion have a much larger impact at multi-gigabit transmission rates.

The use of FEC schemes allows upgrading the line rate to higher data-rates while still supporting the same optical fiber plant. Following initial experiments [25], FEC was first considered in the G-PON and 10G-PON standards [1, 26]. An overview of the most commonly used codes is given in Table 2.4 [27–29].

At first, an 8-bit symbol Reed-Solomon RS(255,223) coding was selected (e.g. in G-PON and 10G-EPON) due to its good performance and good coding gain. Eventually, stronger but more complex Reed-Solomon (RS) codes were considered (Bose-Chaudhuri-Hocquenghem (BCH) codes in a broader sense), as well as staircase codes [30] or LDPC codes [31].

For upstream PON transmission, the use of a non-ideal burst-mode receiver adds another layer of complexity to the performance evaluation of different FEC codes. Improper settling of the receiver can cause bursty errors at the start of each burst. This non-random error distribution causes a reduction in the FEC coding gain, which needs to be taken into consideration when comparing the FEC overhead with the needed additional overhead due to a longer preamble (to avoid these kinds of burst errors) [28]. Alternatively, data scrambling or differential pre-coding can be added at the transmit ONU

Code	OH	Req. input BER*	Req. input BER* (with pre-coding)	Optical FEC coding gain using 1 dBe ≈ 0.7 dBo	Optical FEC coding gain using 1 dBe ≈ 0.9 dBo
Low complexity					
RS(255,223)	13%	1E-3	1.4E-3	5.0 dBo	6.4 dBo
RS(992,864)	13%	2.3E-3	4E-3	5.3 dBo	6.8 dBo
RS(255,201)	20%	2.9E-3	4E-3	5.3 dBo	6.8 dBo
RS(255,151)	41%	1E-2	1.8E-2	6.4 dBo	8.2 dBo
Medium complexity					
RS(992,792)	20%	5.2E-3	9E-3	5.7 dBo	7.3 dBo
RS(1023,847)	18%	4E-3	TBD	6.0 dBo	7.6 dBo
High complexity					
BCH(4095,3501)	15%	5.8E-3	TBD	6.0 dBo	7.6 dBo
LDPC(16000,13952)	13%	1E-2	TBD	6.2 dBo	8.0 dBo
LDPC(19200,16000)	17%	1E-2	TBD	6.7 dBo	8.6 dBo

* Required to obtain an output BER of 1E-12.
Evaluated with an APD-based receiver with 1 dBe ≈ 0.7 - 0.9 dBo.

Table 2.4: Performance of different FEC-codes for burst-mode upstream transmission [26, 28].

side to increase the FEC effectiveness [26, 32].

The choice of FEC scheme for next-generation PONs is still an ongoing topic of discussion, but an advanced RS code is highly likely due to its maturity in well-established PON networks (e.g. RS(1023,847) proposed by Nokia [28]). Alternatively for 50G-EPON, an LDPC code was chosen [33, 34].

Cost Considerations

In contrast with point-to-point links deployed in metro and long-haul networks, passive optical networks require a sheer number of optical components, especially at the ONU side. In the early days of PON, cheap Fabry-Perot (FP) lasers were used for this purpose. For multi-gigabit transmission these can unfortunately no longer be used, due to their large linewidth and multi-mode behaviour (causing more dispersion in the optical fiber) or the introduction of mode partition noise (MPN) (which decreases the available power budget). Instead, they have been replaced by single-mode directly modulated lasers (DMLs) such as DFB lasers or externally modulated lasers (EMLs), using electro-absorption modulators (EAMs).

Considerable efforts have been made by standardization bodies into finding the most cost-effective solutions for next-generation passive optical networks. One such way is to leverage high-volume existing 25 Gbit/s data center components, in particular 25 Gbit/s DMLs and EMLs devices [35]. As shown in Table 2.2, ITU-T standards also define different classes, corresponding to the cost of the optics used. For example, Class B+ or C+ links would use DFB lasers / APD based receivers at both the OLT and ONU side [1].

Security Considerations

PON has a number of security vulnerabilities [2] inherent to its architecture: as the fiber is shared among many end-users, broadcast DS information from the OLT to one of the ONUs must be encrypted to avoid eavesdropping. Denial-of-service attacks in the US direction are also possible when a malicious ONU blinds the OLT by transmitting excessive amounts of optical power at unauthorized times. Finally, because the OLT broadcasts the identification info of the different ONUs, data theft through spoofing is also possible. Protection mechanisms such as encryption are typically implemented in the PON MAC layer (in the case of ITU-T defined PON standards) and are not further discussed.

2.2 Continuous-Mode PON-Receivers

After having discussed several aspects regarding the deployment of PONs, we now turn our attention to the development of integrated opto-electronic receivers targeting these networks.

Receivers at the ONU side for downstream transmission operate in continuous-mode and must convert the unipolar photocurrent from the photodiode into a differential output signal. To do this, they need a reference voltage at the input of the S2D amplifier. This voltage must be set as to remove any DC-offset voltage at the differential output (ensuring a balanced signal). Typically, this is done using a feedback loop as shown in Fig. 2.6 [36].

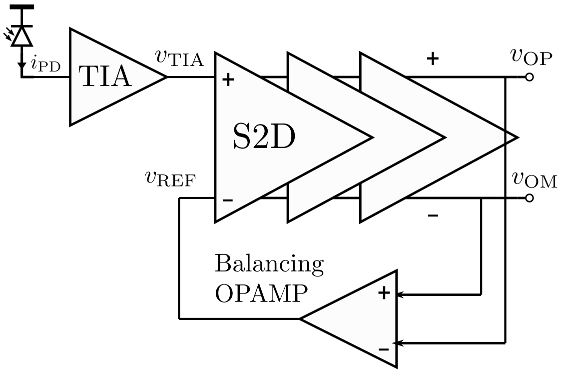

Figure 2.6: A typical continuous-mode AOC system.

When the average $v_{\mathrm{OP}}^{\mathrm{avg}} > v_{\mathrm{OM}}^{\mathrm{avg}}$, the reference input for the S2D amplifier is increased using the balancing OPAMP until the DC output offset voltage is zeroed. The removal of this DC-offset introduces a high-pass pole in the frequency response of the datapath. This pole must be chosen with a sufficiently low frequency, because it introduces baseline wander when sequences of consecutive identical digits (CID) are received. This wander causes a power penalty, which can be written as [37]:

$$PP = 1 + \frac{2\pi f_{\mathrm{LF}} r}{B} \tag{2.1}$$

In this equation, r is the number of consecutive identical digits (CID), B the baud rate and f_{LF} the frequency of the high-pass pole in the frequency response of the datapath. For example, using a coding scheme with a consecutive identical digits (CID) of $r = 72$ (as defined in most PON standards) at a baudrate of 25 Gbit/s while allowing a maximum power penalty of 0.1 dB requires a high-pass pole with a frequency of at most 1.3 MHz.

Because the position in the PON network (and hence the loss in the ODN) is different for each and every ONU, the gain in each receiver must be set to ensure a fixed output swing. In continuous-mode, this is often done through software using digital control settings. Alternatively, an integrated, on-chip AGC system (e.g. the one shown in Fig. 2.7) can be used, in which a power detector is used in a feedback loop to regulate the output swing to a fixed level. Receivers developed for NRZ modulation can instead use limiting post-amplifiers in their datapath. In this case, AGC can be used to extend the input dynamic range by adjusting the gain of the front-end transimpedance amplifier (TIA).

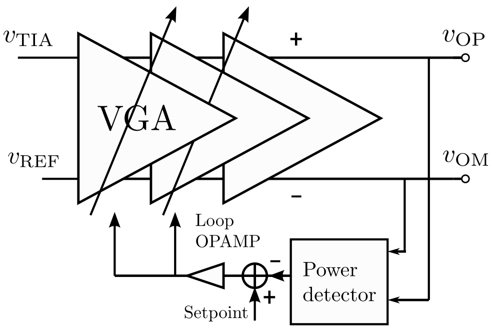

Figure 2.7: A typical continuous-mode AGC system.

Notice that when implementing both the AOC feedback loop and the AGC feedback loop in the same receiver, care must be taken to avoid loop interaction. Luckily, this dangerous situation can be easily avoided entirely in continuous-mode by ensuring that the AGC loop operates much slower than the AOC loop.

2.3 Burst-Mode PON Receivers

This dissertation focuses on the development of burst-mode receivers for the upstream-link in a PON network, placed at the OLT side. Fig. 2.8 shows the typical current received by the photodiode in a burst-mode receiver. Here, a sequence of two bursts is shown in which the first burst (e.g from ONU 1) has a power much greater than the second burst (e.g from ONU 2). Such a situation arises e.g. when a distant subscriber and a nearby subscriber transmit bursts in adjacent time slots. The burst-mode transmitter (BMTX) circuit needs to be optimized to reduce the duration of 'dead-zone', i.e. the transmitter's turn-on/turn-off time $T_{\mathrm{on}}/T_{\mathrm{off}}$, to avoid unwanted overlap with bursts assigned to other ONUs. The bursts are separated by only a small guard time (e.g. 25 ns) in which all ONU transmitters are turned off. Additionally, each burst can potentially also have a different extinction ratio, more inter-symbol interference (ISI), or a worse signal-to-noise ratio (SNR) ratio. Table 2.5 shows the burst-timing specifications as imposed by several PON-standards.

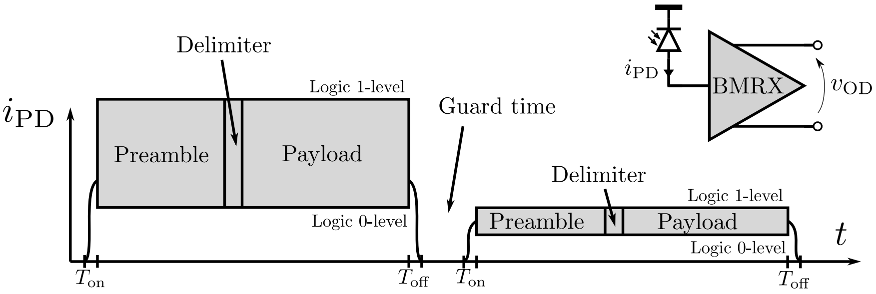

Figure 2.8: A typical burst-mode input photocurrent.

Let us first apply this signal at the input of a conventional continuous-mode receiver and consider the AOC as shown in Fig. 2.6: the resulting waveforms (averaged, not showing the data modulation) can be seen in Fig. 2.9. When the strong burst is received at $t = 0$, a large difference presents itself between $v_{\mathrm{TIA}}^{\mathrm{avg}}$ and $v_{\mathrm{REF}}^{\mathrm{avg}}$, which is amplified through the post-amplifiers in the datapath. This causes a non-zero average differential output signal $v_{\mathrm{OD}}^{\mathrm{avg}}$, which is zeroed through the feedback operation of the AOC loop. Here, the AOC loop has a gain-bandwidth product (GBWP) of 1 MHz (its choice is based on Eq. (2.1)), with a datapath gain of 10 and a maximal output swing

Standard	**Preamble time**	**Delimiter time**	**Guard time**
A-PON* [1, 5]	51.2 ns (8 bits)	-	25.6 ns (4 bits)
B-PON† [1, 5]	12.8 ns (8 bits)	-	12.8 ns (8 bits)
G-PON‡ [6]	35.2 ns (44 bits)	16 ns (20 bits)	25.6 ns (32 bits)
GE-PON [7, 38]	up to 800 ns (800 bits)	-	>25.8 ns (32 bits)
10G-EPON [8, 38]	up to 800 ns (8000 bits)	-	>25.8 ns (32 bits)
XG-PON [9]	64.3 ns (160 bits)	12.9 ns (32 bits)	25.7 ns (64 bits)
XGS-PON [19]	128.6 ns (1280 bits)	3.2 ns (32 bits)	51.4 ns (512 bits)

* 155.52Mbps upstream values. †622.08Mbps upstream values. ‡1.25Gbps upstream values.

Table 2.5: Typical values for the burst-timings in several PON standards.

$v_{\mathrm{OD,max}}^{\mathrm{ptp}}$ of 0.5 V. The resulting settling time around 1 µs is already unacceptably long. In addition, clipping in the datapath causes the output error term $v_{\mathrm{OD}}^{\mathrm{avg}}$ to be limited, which causes linear accumulation in the balancing OPAMP. v_{REF} now approaches the new value of v_{TIA} very slow (similar to slewing), which increases the settling times even further. Because such loops have to re-settle at the start of every burst, a very long preamble would be needed which increases overhead and reduces transmission efficiency. As a result, additional control circuits need to be added, significantly increasing receiver complexity. In the next sections an overview is given of different architectures that can be used to address these challenges.

Single-ended to Differential Conversion

After the conversion of the photocurrent i_{PD} into a single-ended voltage v_{TIA}, the signal must be converted into a differential signal without any residual DC-offset. This conversion implies the choice of a reference level for the S2D amplifier, at which the signal must be centered around. As opposed to continuous-mode receivers, the generation of this reference signal is often separated from the AOC (which compensates for mismatch in later stages) in burst-mode receivers. This allows more design freedom to speed up settling time. In this section methods of generating this reference signal are dis-

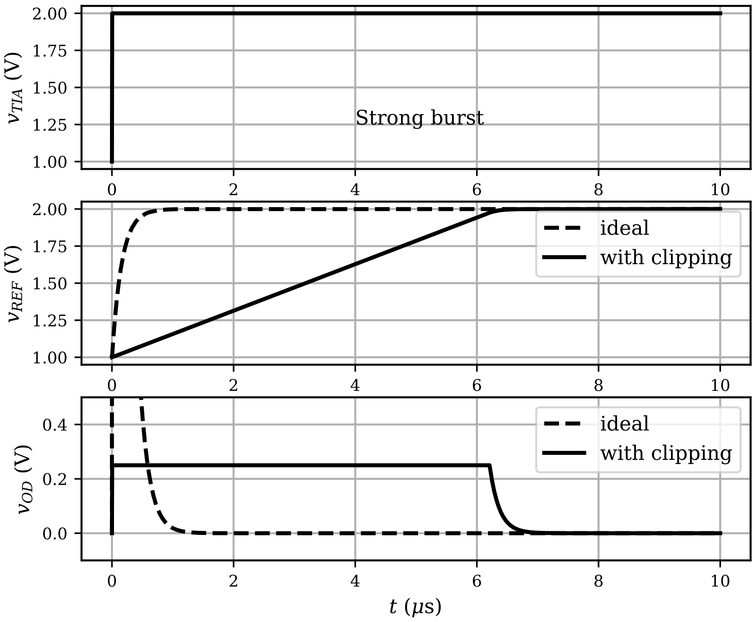

Figure 2.9: TIA voltage v_{TIA}, balancing opamp output voltage v_{REF} and differential output voltage $v_{\mathrm{OD}} = v_{\mathrm{OP}} - v_{\mathrm{OM}}$ showing the effect of clipping in the datapath.

cussed, whereas Section 2.3 discusses how to efficiently zero the remaining residual DC output offset voltage.

The reference signal can be generated through feedback as discussed in Section 2.2, or created using feedforward average detection, as shown in Fig. 2.10 [39, 40]. In order to speed up the settling-time using this method, the bandwidth of the used low-pass filter (LPF) can be switched to a smaller value after the loop has settled to reduce baseline wander.

Some burst-mode receivers propose high-speed peak detectors to quickly extract a suitable reference voltage v_{REF} [39–43]. This method is illustrated in Fig. 2.11. Here, a postive peak-detector (PPD) and negative peak-detector (NPD) are used to generate a proper reference level for the S2D. The use of peak-detectors allow for quick threshold extraction, while in the ideal case completely eliminating baseline wander. Notice that in this case, the peak-detectors must

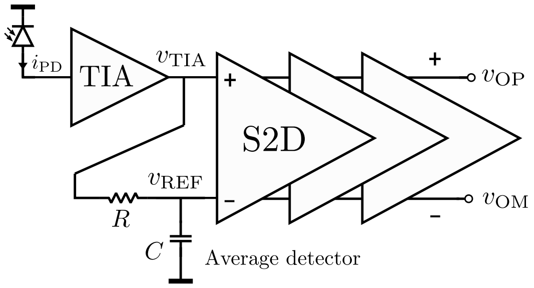

Figure 2.10: S2D reference level generation using feedforward.

be reset at the end of the burst. In addition, peak detectors become increasingly inaccurate at higher baud-rates.

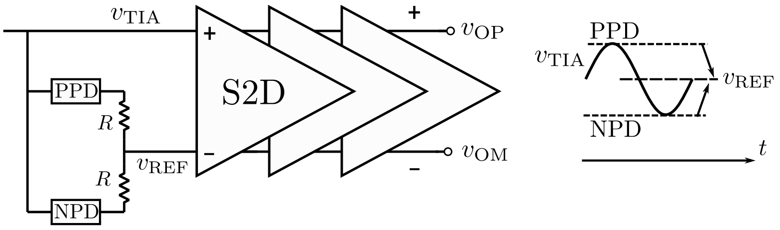

Figure 2.11: S2D reference level generation using feedforward and peak-detectors.

The reference signal can also be generated by building a feedback loop around the front-end TIA as shown in Fig. 2.12. Here, a DC-current is subtracted from the photocurrent i_{PD}, bringing the average v_{TIA} towards the chosen reference voltage v_{REF}. Here, the GBWP of the loop can be reduced after it has settled. Alternatively, the average photocurrent can be extracted and used in a matched replica TIA, which provides a suitable reference level v_{REF} for the S2D amplifier (Fig. 2.13).

Some specific architectures do not require a reference level to be generated. In [44] the output signal can be generated by using edge-detection circuitry, as shown in Fig. 2.14. Here, a delay line is used to generate pulses on the rising and falling edges of a signal, which are then again converted into a NRZ signal by using a hysteresis comparator. In double-sampling receivers such as [45], the two samplers reconstruct the original NRZ pattern from the TIA-integrated

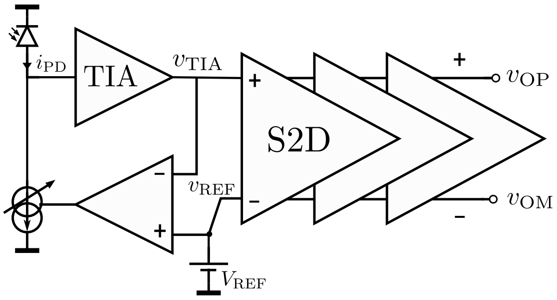

Figure 2.12: S2D reference level generation using feedback around a front-end TIA.

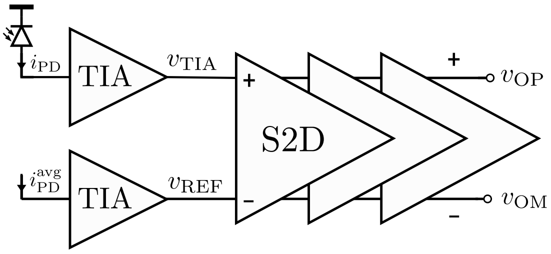

Figure 2.13: S2D reference level generation using a replica TIA.

signal, as shown in Fig. 2.15.

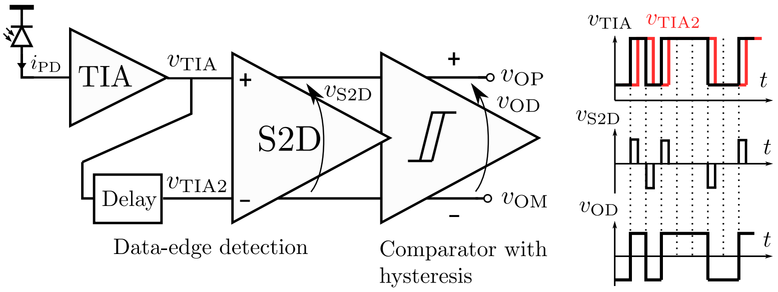

Figure 2.14: Edge-detection based receivers.

Automatic Offset Control

Even when the input of the S2D is perfectly balanced, mismatch in the post-amplifier stages can still cause an offset to occur at the out-

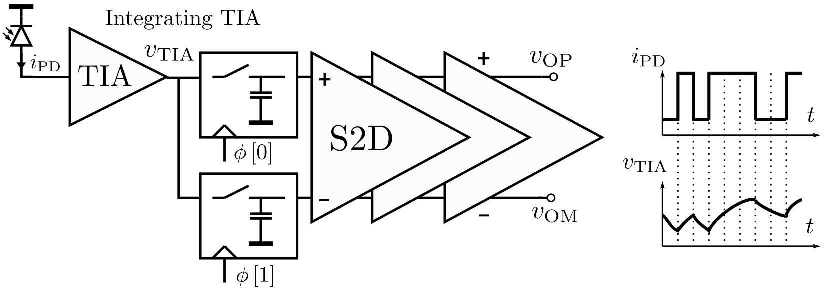

Figure 2.15: Double-sampling based receivers.

put of the receiver. An AOC system ensures that the DC-offset output voltage is zeroed. AOC can be obtained by AC-coupling the different post-amplifiers together, as shown in Fig. 2.16. Alternatively, the stages can be AC-coupled through active feedback, as shown in Fig. 2.17 [39].

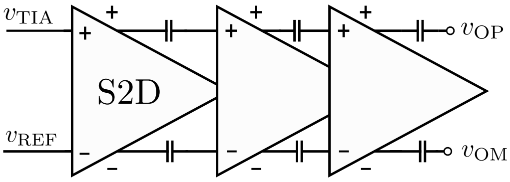

Figure 2.16: AC-coupled post amplifiers.

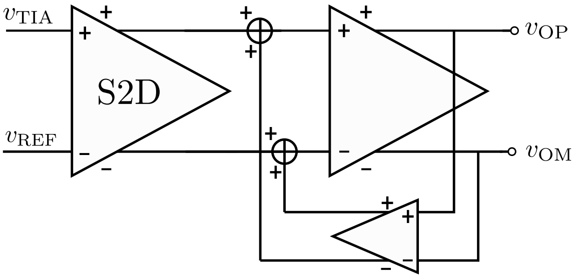

Figure 2.17: Active AC-coupling.

The highest allowable high-pass pole frequency that was obtained using Eq. (2.1) can only be realized using coupling capacitors in the order of several nF (combined with typical input and output impedances of the amplifiers), which immediately eliminates on-chip implementation of Fig. 2.16. On the other hand, active feedback (Fig. 2.17) allows much lower frequencies through the use of reduced GBWP OPAMPS via capacitance multipliers, or operational transconductance amplifiers with ultra-low G_m.

Unfortunately, the presence of this low-frequency high-pass pole is detrimental for burst-mode operation, in that the AOC will need a very long settling time, much longer than what is allowed by the preamble of each burst. Additionally, the gain-bandwidth product of the AOC feedback loop is proportional with the datapath gain. For PON applications the BMRX must be able to adapt the datapath gain over a very wide range, which complicates the AOC feedback loop design.

Several solutions have been proposed to implement a fast but accurate AOC. In [46], an active AOC feedback is used which is toggled between two time constants to allow for faster settling while maintaining CID tolerance. Another way to reduce the settling time is to distribute the AOC feedback corrections over multiple post-amplifiers [47]. Because fewer parasitic poles are now present in each loop, they require less compensation and hence can be made much faster. In addition, loop design is easened because of the smaller datapath gain variation in each amplifier.

A multi-stage feedforward AOC can also be implemented by using high-speed negative peak detectors (NPD) in combination with a differential difference amplifier (DDA), as shown in Fig. 2.18 [48–50]. Here, it can be seen how the reference voltages are generated, providing a balanced input signal for the next post-amplifier. As a result, the residual DC-offset to amplitude ratio is reduced along the chain of amplifiers, eventually zeroing the final differential output offset voltage.

Another method is shown in Fig. 2.19, in which a compensation voltage is added in series with the reference voltage v_REF. The voltage is generated through feedback operation, so stability must be considered in its design. Unlike the solution proposed in Fig. 2.6, the required compensation range is much smaller, so clipping during loop setting (see Fig. 2.9) is less likely to occur. Then similarly as before, the GBWP can be switched between two values to speed up

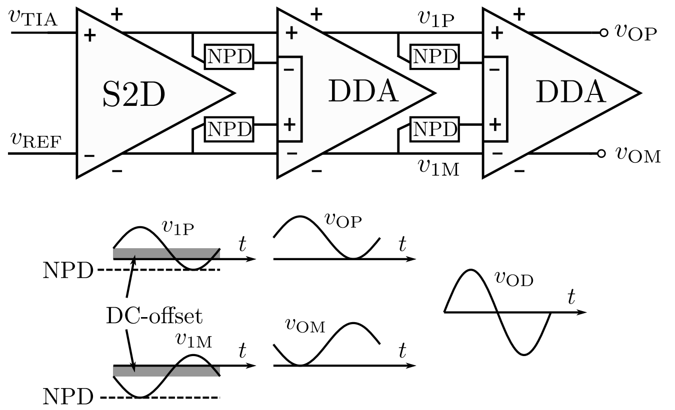

Figure 2.18: Multi-stage feedforward AOC.

settling time.

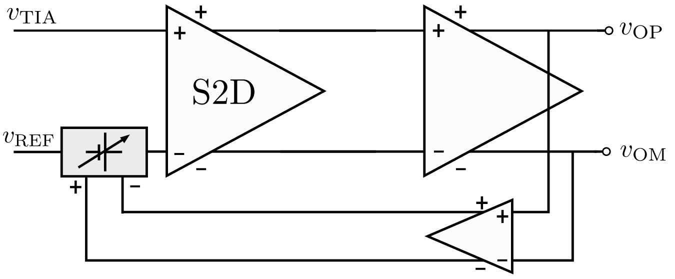

Figure 2.19: Series AOC at the input of the S2D amplifier.

Automatic Gain Control

When bursts of significantly varying strength are received, significant adjustments in the gain of the data path are necessary to obtain a constant output swing and/or to avoid overloading the receiver. AGC can be implemented using feedback (as shown in Fig. 2.7) or through feedforward:

Fig. 2.20 uses feedforward to reduce the gain when the input power is increased. The power detector can be based on the output voltage of the single-ended TIA, but can also be an estimate of the average photocurrent at the input of the TIA. Notice that in this case a

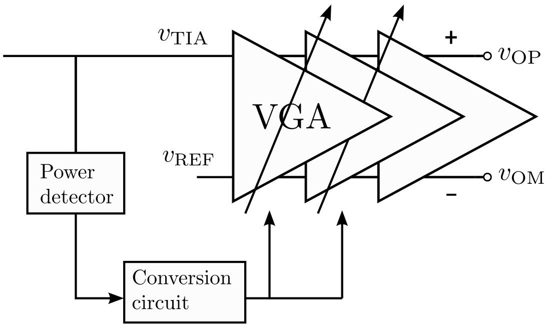

Figure 2.20: Feedforward AGC.

conversion circuit is required to generate an inversely proportional drive signal for the variable-gain-amplifiers (VGAs).

Due to the fact that most BMRX are non-linear receivers mainly designed for NRZ operation, AGC is mainly intended to avoid overloading of the BMRX, in which case the AGC is centered around the front-end TIA as shown in Fig. 2.21. Again, the power detection can be done using the average photocurrent estimate or the average output signal of the TIA itself.

The front-end TIA gain could be adjusted over a continuous range of values (e.g. [50, 51]). At bandwidths above 10 GHz however, it becomes increasingly difficult to adjust the front-end gain while maintaining a constant bandwidth, peaking and group delay variation. TIA design can be significantly simplified by only providing a few discrete transimpedance gains (e.g. [42]), also referred to as step AGC in [40].

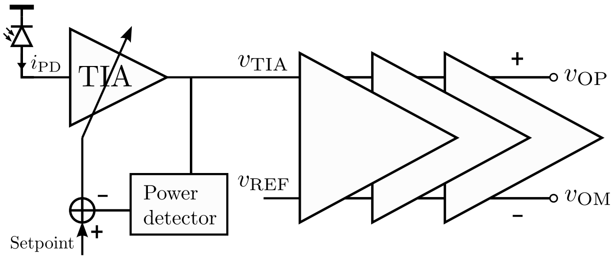

Figure 2.21: AGC feedback around the front-end TIA.

In [50], a continuous feedforward AGC system is implemented in a 10 Gbit/s linear BMRX, which uses the average photocurrent measured at the cathode of a photodiode.

Note that combining the feedback AGC with feedback AOC in burst-mode receivers is quite challenging as opposed to continuous-mode receivers (see Section 2.2) due to the simple fact that one loop can not simply be made much slower, as both loops need to settle within only a limited amount of time. Because both loops will interact, and a more detailed analysis will be necessary.

Consider what happens when the AOC from Fig. 2.7 is combined with the AGC from Fig. 2.6, resulting in the theoretical model depicted in Fig. 2.22. Here, the AOC is obtained through a feedback loop, which generates a voltage v_{BAL} in series with v_{REF} (= v_{REFT}) at the input of the S2D amplifier to zero the low-frequent output offset voltage $v_{\mathrm{OD}} = v_{\mathrm{OP}} - v_{\mathrm{OM}}$.

Meanwhile, the RMS-value $v_{\mathrm{OD}}^{\mathrm{rms}}$ of the differential output voltage v_{OD} is measured and compared to a reference level $V_{\mathrm{OD,goal}}^{\mathrm{rms}}$, which is used to drive a feedback loop which adds or removes gain to/from the VGA. Fig. 2.23 shows what happens when a burst-mode signal v_{TIA} (with $v_{\mathrm{REF}} = v_{\mathrm{TIA}}^{\mathrm{avg}}$ when no burst is present) is applied to the input of the post-amplifier datapath.

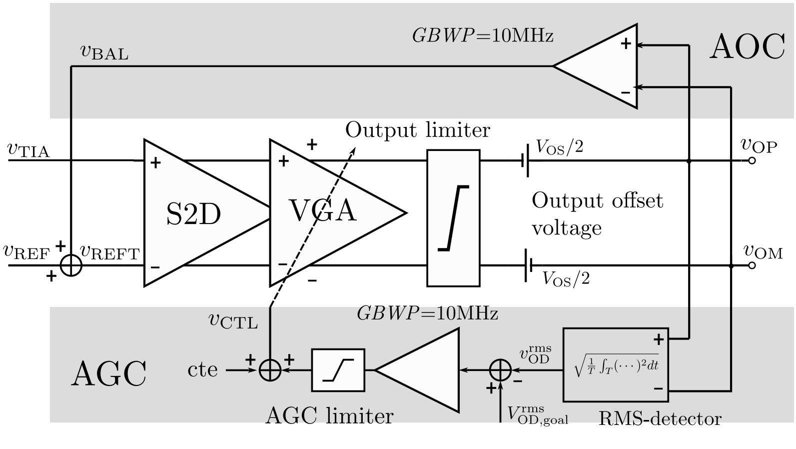

Figure 2.22: Theoretical model with simultaneous feedback AOC and AGC.

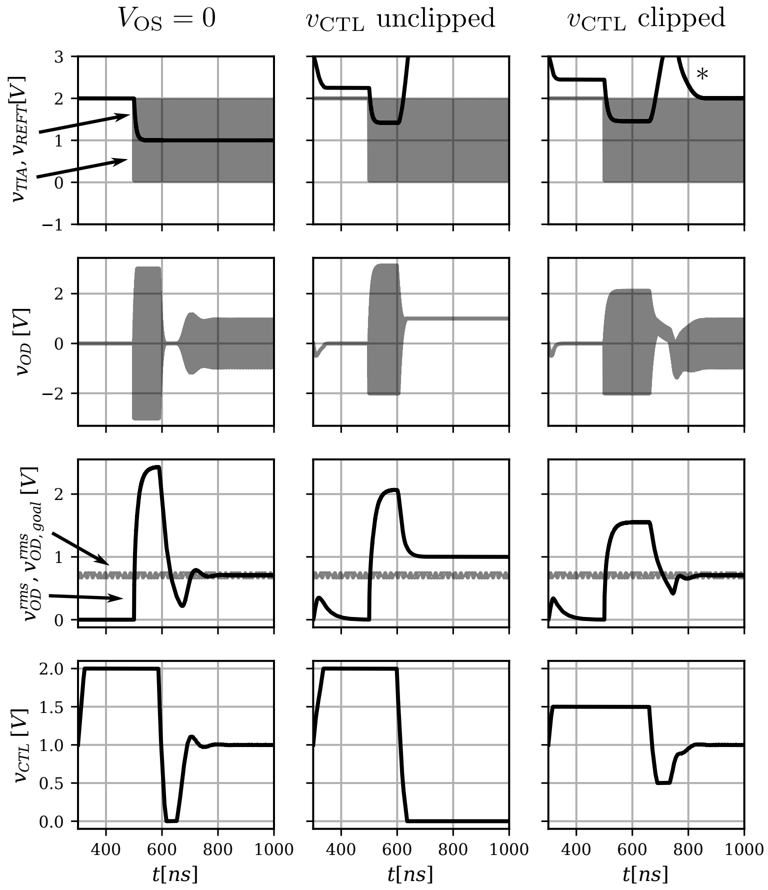

Figure 2.23: Waveforms with simultaneous feedback AOC/AGC.

First, we look at the left column, in which the datapath is perfectly symmetrical and $V_{OS} = 0$. In this case, upon arrival of a burst, v_{REFT} is quickly repositioned towards the center of v_{TIA} through the feedback AOC loop. At the same time, the AGC reduces the gain (using control signal v_{CTL}) as the measured RMS-power lies above the desired level $v_{\mathrm{OD,goal}}^{\mathrm{rms}}$.

The second column shows the situation in which mismatch is present in the datapath, resulting in a non-zero output offset voltage (modeled using a series output voltage V_{OS}). When the offset is sufficiently large ($V_{\mathrm{OS}} > v_{\mathrm{OD,goal}}^{\mathrm{rms}}$), the AGC feedback loop senses the offset as actual signal output swing and starts reducing the gain of the datapath. As this does not necessarily decreases the output offset voltage V_{OS}, the gain of the datapath is being completely collapsed, which prevents the AOC feedback loop to fix the offset issue in time due to the lack of loop gain. As a result, the output signal completely clips to one side, rendering the receiver into an unusable state.

By limiting the output range of the AGC to be only a fraction of what the bias gain (*cte*) provides, a minimum datapath gain can always be guaranteed. This is illustrated in the rightmost column; Here, $cte = 1V$ and the output range of the AGC is limited to ±0.5 V. In this case, the AGC loop initially settles in the wrong direction, but the process is quickly reversed (indicated by * in Fig. 2.23) as the AOC has completed its job: as a result, only a slight increase in settling time is observed.

Digital Burst-Mode AGC/AOC

In the last few years, several burst-mode receivers have been developed in advanced deep sub-micron CMOS nodes, where AOC and/or AGC can be implemented partly in the digital domain, as shown in Fig. 2.24 [52–55].

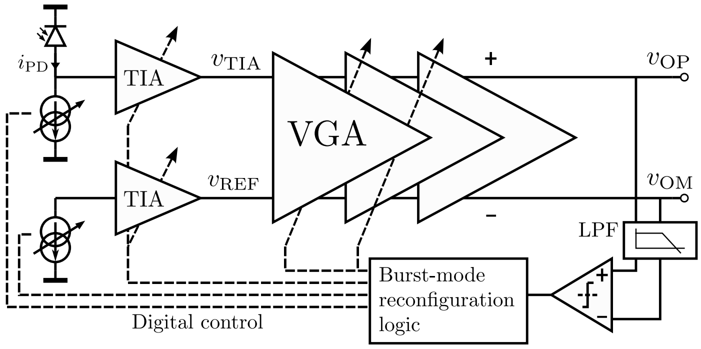

Figure 2.24: AGC and AOC implemented using digital logic.

Because these receivers are mainly used for NRZ operations targeting data center applications (e.g. optical packet switching), a high-speed comparator can be used instead of a power- or average detector to drive the AOC and AGC. At the start of each burst, the burst-mode reconfiguration logic block initiates a form of successive approximation algorithm to set the correct input offset current and VGA gain, in only a few clock cycles. In this case, the limiting factor is the bandwidth of the LPF, and the speed at which the comparator toggles.

Burst-Mode Signaling

In order to trigger the analog or digital AOC and AGC control loops, the start of each burst needs to be detected by a so-called SOB detector. In its most simple form, this can be a comparator which triggers when the average input photocurrent or TIA output exceeds a certain threshold. More complex solutions make use of the edges of the signal instead, by preceding the comparator by a high-pass filter and amplifier. Typically, these circuits are placed at the beginning of the datapath chain, to reduce the impact of clipped amplifier stages.

The very wide dynamic range at the input of the BMRX makes the SOB detector design very challenging, in particular when a weak burst is preceeded by a very strong one, with only little amount of guard time. In such cases an EOB detector can be used which monitors the output of the BMRX for line inactivity. In addition, its output can also be used for interfacing with the MAC layer of the PON network.

Burst-Mode Equalization

Equalization has been widely used to increase the optical link budget by extending the reach of the fiber through EDC, or by extending the bandwidth of the low-cost ONUs transmitters. Applying equalization on the upstream data link in a PON requires the use of a BMEQ, which is able to adapt the equalizer parameters on a burst-to-burst basis. Fixed equalizer structures have been co-integrated together with a burst-mode receiver to compensate e.g. an APD [55], but at the time of writing, no real-time high speed BMEQ implementations exist, but the ever-increasing demand for bandwidth will eventually push the upstream PON transmission link to higher baudrates, requiring BMEQ to be deployed.

Extensive research [56–59] has already investigated the requirements of these BMEQ solutions, typically proposing a 3- to 7-taps FFE combined with a 2-taps DFE to eliminate post-cursor ISI: such an equalizer is shown in Fig. 2.25.

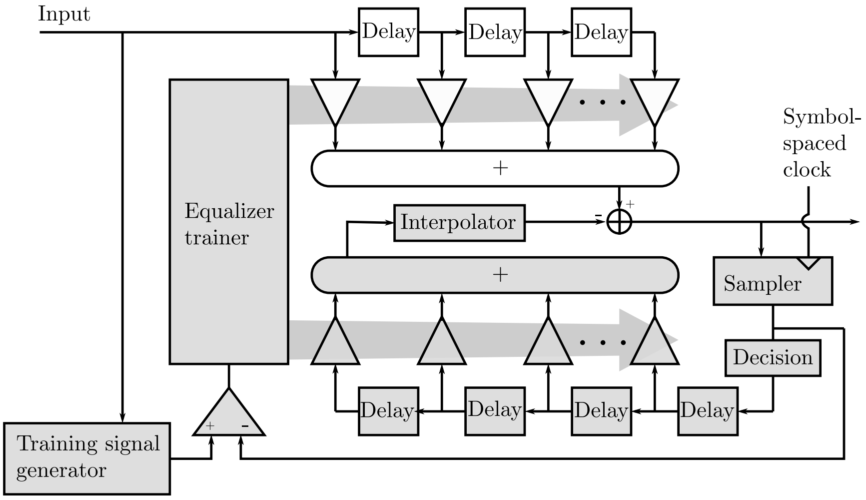

Figure 2.25: Proposed architecture of a BMEQ.

During the preamble of each burst, the equalizer trains its parameters using an adaptive algorithm. Typically, least-mean-squares (LMS) is considered in favor of the more complex recursive-least-squares (RLS), keeping real-time implementation in mind. The reference signal used for the training can be taken from the output of the BMEQ (blind training, which assumes a sufficiently low BER), or generated using a training signal generator.

The training signal generator needs to generate a known pilot sequence aligned with the received training sequence during the preamble of each burst. Ideally, this generator should be able to align with heavily degraded signals, favoring correlation-based techniques.

Burst-Mode Clock- and Data Recovery

In order to extract the actual data from the processed signal, a time-reference is needed which determines the sampling instant in the decision process. Typically, this reference is extracted from the received signal using a clock- and data-recovery (CDR) circuit. In burst-mode applications, these circuits need a short response time and a large CID tolerance. The development of these burst-mode clock- and data-recovery (BMCDR) circuits lies outside the scope of this dissertation.

References

[1] L. Kazovsky, N. Cheng, W. Shaw, D. Gutierrez, and S. Wong, *Broadband Optical Access Networks*. Wiley, 2011.

[2] C. Lam, *Passive Optical Networks: Principles and Practice*. Elsevier Science, 2011.

[3] Ron Heron, Ana Pesovic. (2019) TWDM-PON: Taking Fiber to New Wavelengths. [Online]. Available: https://www.nokia.com/blog/twdm-pon-taking-fiber-new-wavelengths/

[4] FSAN. The FSAN Standards Roadmap 2.0. [Online]. Available: http://www.fsan.org/roadmap/

[5] ITU-T Recommendation G.983.1. (2010) Broadband optical access systems based on Passive Optical Networks (PON). [Online]. Available: https://www.itu.int/rec/T-REC-G.983.1-200501-I/

[6] ITU-T Recommendation G.984.2. (2012) Gigabit-capable passive optical networks (GPON): Physical Media Dependent (PMD) layer specification. [Online]. Available: https://www.itu.int/rec/T-REC-G.984.2

[7] IEEE P802.3ah Ethernet in the First Mile Task Force. (2009) Ethernet in the first mile. [Online]. Available: http://www.ieee802.org/3/efm/

[8] IEEE 802.3av-2009. (2009) IEEE Standard for Information technology– Local and metropolitan area networks– Specific requirements– Part 3: CSMA/CD Access Method and Physical Layer Specifications Amendment 1: Physical Layer Specifications and Management Parameters for 10 Gb/s Passive Optical Networks.

[9] ITU-T Recommendation G.987. (2012) 10-Gigabit-capable passive optical network (XG-PON) systems. [Online]. Available: https://www.itu.int/rec/T-REC-G.987/en

[10] *40-Gigabit-capable passive optical networks (NG-PON2): Definitions, abbreviations and acronyms*, ITUT-T Recommendation G.989, 2015.

[11] ITU-T Recommendation G.9807. (2016) 10-Gigabit-capable symmetric passive optical network (XGS-PON) systems. [Online]. Available: https://www.itu.int/rec/T-REC-G.9807.1-201606-I/en

[12] IEEE P802.3ca 50G-EPON Task Force, "Physical Layer Specifications and Management Parameters for 25Gb/s and 50Gb/s Passive Optical Networks." [Online]. Available: http://www.ieee802.org/3/ca/

[13] G.hsp.50Gpmd. (2017) Higher Speed Passive Optical Networks: 50G PMD. [Online]. Available: https://www.itu.int/rec/T-REC-G.989/en

[14] Technavio. (2018) Global Passive Optical Network Market 2018-2022 | Increase in Internet Traffic to Boost Growth. [Online]. Available: https://apnews.com/fb263f982cd64cbe83cf44907b883092

[15] Kagan Media Research Group. (2017) GPON Equipment Market Research 2016-2022. [Online]. Available: https://www.fiberoptictel.com/gepongpon-equipment-market-research-2017-2022-brief/

[16] Ana Pesovic (Nokia Blog). (2018) XG-PON or XGS-PON: dont make a costly spelling mistake. [Online]. Available: https://www.nokia.com/blog/xg-pon-or-xgs-pon-dont-make-costly-spelling-mistake/

[17] Daniel Grossman (Broadband World News). (2019) Will NGPON2 Be 'Real' in 2019? It Depends. [Online]. Available: http://www.broadbandworldnews.com/author.asp?section_id=714&doc_id=750251

[18] Stephen Hardy (Lightwave Online). (2018) Residential 10G PON deployments wait until 2020: Broadbandtrends study.

[19] ITU-T Recommendation G.9807.1. (2016) 10-Gigabit-capable symmetric passive optical network (XGS-PON). [Online]. Available: https://www.itu.int/rec/T-REC-G.9807.1

[20] R. Bonk, W. Poehlmann, H. Schmuck, and T. Pfeiffer, "Crosstalk in twdm-pon beyond ng-pon2," in *2015 Optical Fiber Communications Conference and Exhibition (OFC)*, March 2015, pp. 1–3.

[21] P. Ossieur, C. Antony, A. M. Clarke, A. Naughton, H. Krimmel, Y. Chang, C. Ford, A. Borghesani, D. G. Moodie, A. Poustie, R. Wyatt, B. Harmon, I. Lealman, G. Maxwell, D. Rogers, D. W. Smith, D. Nesset, R. P. Davey, and P. D. Townsend, "A 135-km 8192-split carrier distributed dwdm-tdma pon with $2\times 32\times 10$ gb/s capacity," *Journal of Lightwave Technology*, vol. 29, no. 4, pp. 463–474, Feb 2011.

[22] E. Säckinger, *Broadband Circuits for Optical Fiber Communication*. Wiley, 2005.

[23] ZeitgeistLab.ca. (2018) 10G-EPON Ethernet Passive Optical Networks.

[24] E. Harstead, D. V. Veen, V. Houtsma, and P. Dom, "Technology Roadmap for Time Division Multiplexed Passive Optical Networks (TDM PONs)," *Journal of Lightwave Technology*, pp. 1–1, 2018.

[25] Y. Yi, S. Verschuere, Z. Lou, P. Ossieur, J. Bauwelinck, X. Qiu, and J. Vandewege, "Simulations and experiments on the effective optical gain of fec in a gpon uplink," *IEEE Photonics Technology Letters*, vol. 19, no. 2, pp. 82–84, Jan 2007.

[26] D. T. van Veen and V. E. Houtsma, "Proposals for Cost-Effectively Upgrading Passive Optical Networks to a 25G Line Rate," *Journal of Lightwave Technology*, vol. 35, no. 6, pp. 1180–1187, March 2017.

[27] N. Brandonisio, S. Porto, D. Carey, P. Ossieur, G. Talli, N. Parsons, and P. Townsend, "Forward error correction analysis for 10gb/s burst-mode transmission in tdm-dwdm pons," in *2017 Optical Fiber Communications Conference and Exhibition (OFC)*, March 2017, pp. 1–3.

[28] V. H. Dora van Veen, "FEC code for 25/50/100G EPON (IEEE P802.3ca 100G-EPON Task Force Meeting)," 2017.

[29] M. N. Sakib and O. Liboiron-Ladouceur, "A Study of Error Correction Codes for PAM Signals in Data Center Applications," *IEEE Photonics Technology Letters*, vol. 25, no. 23, pp. 2274–2277, Dec 2013.

[30] L. M. Zhang and F. R. Kschischang, "Low-Complexity Soft-Decision Concatenated LDGM-Staircase FEC for High-Bit-Rate Fiber-Optic Communication," *Journal of Lightwave Technology*, vol. 35, no. 18, pp. 3991–3999, Sep. 2017.

[31] K. Gunnam, J. M. Catala Perez, and F. Garcia-Herrero, "Algorithms and VLSI Architectures for Low-Density Parity-Check Codes: Part 1-Low-Complexity Iterative Decoding," *IEEE Solid-State Circuits Magazine*, vol. 8, no. 4, pp. 57–63, Fall 2016.

[32] D. v. V. Vincent Houtsma, "Impact of pre-coding and high gain FEC on 25, 50 and 100G EPON," 2016.

[33] J. S. W. Zheng Liu, Junwen Zhang, "FEC for Upstream: 8K LDPC Code (IEEE 802.3ca Task Force Meeting)," 2018.

[34] M. Yang, L. Li, X. Liu, and I. B. Djordjevic, "Fpga-based real-time soft-decision ldpc performance verification for 50g-pon," in *2019 Optical Fiber Communications Conference and Exhibition (OFC)*, March 2019, pp. 1–3.

[35] E. Harstead, D. van Veen, and V. Houtsma, "F25G/50G/100G EPON wavelength plan)," 2016.

[36] J. Verbrugghe, R. Vaernewyck, B. Moeneclaey, X. Yin, G. Maxwell, R. Cronin, G. Torfs, X. Qiu, C. P. Lai, P. Townsend, and J. Bauwelinck, "Multichannel 25 Gb/s Low-Power Driver and Transimpedance Amplifier Integrated Circuits for 100 Gb/s Optical Links," *Journal of Lightwave Technology*, vol. 32, no. 16, pp. 2877–2885, Aug 2014.

[37] E. Säckinger, *Broadband Circuits for Optical Fiber Communication*. Wiley, 2005.

[38] X. Qiu, X. Yin, J. Verbrugghe, B. Moeneclaey, A. Vyncke, C. Van Praet, G. Torfs, J. Bauwelinck, and J. Vandewege, "Fast Synchronization 3R Burst-Mode Receivers for Passive Optical Networks," *Journal of Lightwave Technology*, vol. 32, no. 4, pp. 644–659, Feb 2014.

[39] K. Hara, S. Kimura, H. Nakamura, N. Yoshimoto, and H. Hadama, "New AC-Coupled Burst-Mode Optical Receiver Using Transient-Phenomena Cancellation Techniques for 10 Gbit/s-Class High-Speed TDM-PON Systems," *Journal of Lightwave Technology*, vol. 28, no. 19, pp. 2775–2782, Oct 2010.

[40] M. Noda, N. Suzuki, S. Yoshima, M. Nogami, and J. Nakagawa, "Technology progress of high-speed burst-mode 3R receiver for PON applications," in *OFC/NFOEC*, March 2012, pp. 1–3.

[41] M. Noda, S. Yoshima, K. Ishii, S. Shirai, M. Nogami, and J. Nakagawa, "Dual-rate optical transceiver incorporating fully optimized burst-mode AGC/ATC functions for 10G-EPON systems," in *36th European Conference and Exhibition on Optical Communication*, Sep. 2010, pp. 1–3.

[42] T. De Ridder, P. Ossieur, B. Baekelandt, C. Melange, J. Bauwelinck, C. Ford, X. Qiu, and J. Vandewege, "A 2.7V 9.8Gb/s Burst-Mode TIA with Fast Automatic Gain Locking and Coarse Threshold Extraction," in *2008 IEEE International Solid-State Circuits Conference - Digest of Technical Papers*, Feb 2008, pp. 220–221.

[43] P. Ossieur, T. De Ridder, J. Bauwelinck, C. Melange, B. Baekelandt, Xing-Zhi Qiu, J. Vandewege, G. Talli, C. Antony, P. Townsend, and C. Ford, "A 10 Gb/s burst-mode receiver with automatic reset generation and burst detection for extended reach PONs," in *2009 Conference on Optical Fiber Communication - incudes post deadline papers*, March 2009, pp. 1–3.

[44] M. Nogawa, Y. Ohtomo, S. Kimura, K. Nishimura, T. Kawamura, and M. Togashi, "A 10Gb/s burst-mode adaptive gain select limiting amplifier in 0.13/spl um CMOS," in *2006 IEEE International Solid State Circuits Conference - Digest of Technical Papers*, Feb 2006, pp. 940–949.

[45] M. H. Nazari and A. Emami-Neyestanak, "A 24-Gb/s Double-Sampling Receiver for Ultra-Low-Power Optical Communication," *IEEE Journal of Solid-State Circuits*, vol. 48, no. 2, pp. 344–357, Feb 2013.

[46] J. Put, X. Yin, J. Gillis, X. Z. Qiu, J. Bauwelinck, J. Vandewege, H. . Krimmel, and P. Vetter, "10 Gbit/s burst-mode limiting amplifier with switched time constants for fast settling and large CID tolerance," *Electronics Letters*, vol. 47, no. 17, pp. 970–972, August 2011.

[47] M. Nogawa, K. Nishimura, J. Terada, M. Nakamura, S. Nishihara, and Y. Ohtomo, "A 10-Gb/s burst-mode limiting amplifier using a two-stage active feedback circuit," in *2009 Symposium on VLSI Circuits*, June 2009, pp. 18–19.

[48] P. Ossieur, D. Verhulst, Y. Martens, Wei Chen, J. Bauwelinck, Xing-Zhi Qiu, and J. Vandewege, "A 1.25-gb/s burst-mode receiver for GPON applications," *IEEE Journal of Solid-State Circuits*, vol. 40, no. 5, pp. 1180–1189, May 2005.

[49] T. D. Ridder, P. Ossieur, C. Melange, B. Baekelandt, J. Bauwelinck, X. Z. Qiu, and J. Vandewege, "10 Gbit/s burst-mode post-amplifier with automatic reset," *Electronics Letters*, vol. 44, no. 23, pp. 1371–1373, November 2008.

[50] P. Ossieur, N. A. Quadir, S. Porto, C. Antony, W. Han, M. Rensing, P. O'Brien, and P. D. Townsend, "A 10 Gb/s Linear Burst-Mode Receiver in 0.25um SiGe:C BiCMOS," *IEEE Journal of Solid-State Circuits*, vol. 48, no. 2, pp. 381–390, Feb 2013.

[51] J. Nakagawa, M. Nogami, N. Suzuki, M. Noda, S. Yoshima, and H. Tagami, "10.3Gb/s burst-mode 3R receiver incorporating full AGC optical receiver and 82.5GS/s sampling CDR for 10G-EPON systems," in *2009 35th European Conference on Optical Communication*, Sep. 2009, pp. 1–2.

[52] A. Rylyakov, J. E. Proesel, S. Rylov, B. G. Lee, J. F. Bulzacchelli, A. Ardey, B. Parker, M. Beakes, C. W. Baks, C. L. Schow, and M. Meghelli, "A 25 gb/s burst-mode receiver for low latency photonic switch networks," *IEEE Journal of Solid-State Circuits*, vol. 50, no. 12, pp. 3120–3132, Dec 2015.

[53] A. Rylyakov, J. Proesel, S. Rylov, B. Lee, J. Bulzacchelli, A. Ardey, B. Parker, M. Beakes, C. Baks, C. Schow, and M. Meghelli, "22.1 A 25Gb/s burst-mode receiver for rapidly reconfigurable optical networks," in *2015 IEEE International Solid-State Circuits Conference - (ISSCC) Digest of Technical Papers*, Feb 2015, pp. 1–3.

[54] I. Ozkaya, A. Cevrero, P. A. Francese, C. Menolfi, M. Braendli, T. Morf, D. Kuchta, L. Kull, M. Kossel, D. Luu, M. Meghelli, Y. Leblebici, and T. Toifl, "A 56gb/s burst-mode nrz optical receiver with 6.8ns power-on and cdr-lock time for adaptive optical links in 14nm finfet cmos," in *2018 IEEE International Solid - State Circuits Conference - (ISSCC)*, Feb 2018, pp. 266–268.

[55] K. Chen and A. Emami, "A 25gb/s apd-based burst-mode optical receiver with 2.24ns reconfiguration time in 28nm cmos," in *2018 IEEE Custom Integrated Circuits Conference (CICC)*, April 2018, pp. 1–4.

[56] S. Porto, C. Antony, A. Jain, D. Kelly, D. Carey, G. Talli, P. Ossieur, and P. D. Townsend, "Demonstration of 10 Gbit/s burst-mode transmission using a linear burst-mode receiver and burst-mode electronic equalization [invited]," *IEEE/OSA Journal of Optical Communications and Networking*, vol. 7, no. 1, pp. A118–A125, Jan 2015.

[57] S. Porto, C. Antony, G. Talli, D. Carey, P. Ossieur, and P. D. Townsend, "Demonstration of 10Gb/s burst-mode transmission using a linear burst-mode receiver and burst-mode electronic equalization," in *OFC 2014*, March 2014, pp. 1–3.

[58] P. Ossieur, C. Melange, T. De Ridder, J. Bauwelinck, B. Baekelandt, X. Qiu, and J. Vandewege, "Burst-Mode Electronic Equalization for 10-Gb/s Passive Optical Networks," *IEEE Photonics Technology Letters*, vol. 20, no. 20, pp. 1706–1708, Oct 2008.

[59] P. Torres-Ferrera, V. Milite, V. Ferrero, M. Valvo, R. Mercinelli, and R. Gaudino, "Burst-Mode Equalization Strategies in 25 Gbps US-PON using Duobinary and 10G-Class APD for 20-km in C-Band," in *2019 Optical Fiber Communications Conference and Exhibition (OFC)*, March 2019, pp. 1–3.

3

A 50Gbit/s PAM-4 Linear Burst-Mode Transimpedance Amplifier with Discrete Lookup-Table based AGC/AOC

Various options such as PAM-4 [1, 2], multilevel interleaving [3], duobinary modulation [4], compensation of chromatic dispersion or bandwidth limitations of 10G-class optics [5] (e.g. through equalization [6]) are considered to investigate the feasibility of next-generation time-division multiplexed PONs. However, these options require the use of a linear BMRX. Such a BMRX needs to be able to quickly (within a few 10s of nanoseconds) measure the amplitude of incoming bursts and set its internal DC-offset (AOC) and gain (AGC) to maintain a linear response.

For this purpose, we present in this chapter a first-generation 50 Gbit/s PAM-4 linear burst-mode transimpedance amplifier (LBMTIA) for the upstream traffic in TDM-PONs, where AOC and AGC are set using a digitally controllable datapath with a simple LUT. First, we present its architecture, followed by a summary of results, discussing both its continuous- and burst-mode operation. In Chapter 5 the receiver will be used to further investigate the requirements of future BMEQs. This contents of this chapter are based on the paper, entitled:

G. Coudyzer, P. Ossieur, L. Breyne, M. Matters, J. Bauwelinck, and X. Yin, “A 50 Gbit/s PAM-4 Linear Burst-Mode Transimpedance Amplifier,” *IEEE Photonics Technology Letters*, vol. 31, no. 12, pp. 951–954, June 2019.

3.1 Receiver Architecture

The LBMTIA architecture is shown in Fig. 3.1: it consists of a fixed-gain TIA front-end, a S2D amplifier, two VGAs and an output driver (OD). The front-end TIA has a fixed gain of 160 Ω (44 dB Ω and is implemented using a shunt-feedback topology as in [7, 8]. The S2D amplifier, VGAs use a simple cascoded differential pair, with adjustable load and emitter degeneration resistors to vary the gain between 3 dB and 8 dB. The gain of the output pair differential pair can be varied between 0 dB and 2 dB. As a result, the gain of the datapath can be digitally switched between different discrete values, with total transimpedance gains ranging from 0.45 kΩ to 3.0 kΩ. In the same way, constant bandwidth is ensured by switching appropriate capacitors to the internal amplifier nodes. The DC offset of the amplifier chain can be compensated using a voltage (generated using a digital-to-analog converter (DAC)) in series with the reference voltage at the input of the S2D.

All digital settings are stored in a LUT with 4 slices S_0 to S_3, which are configured to contain appropriate settings that optimize the data path gain and frequency response for different input power levels.

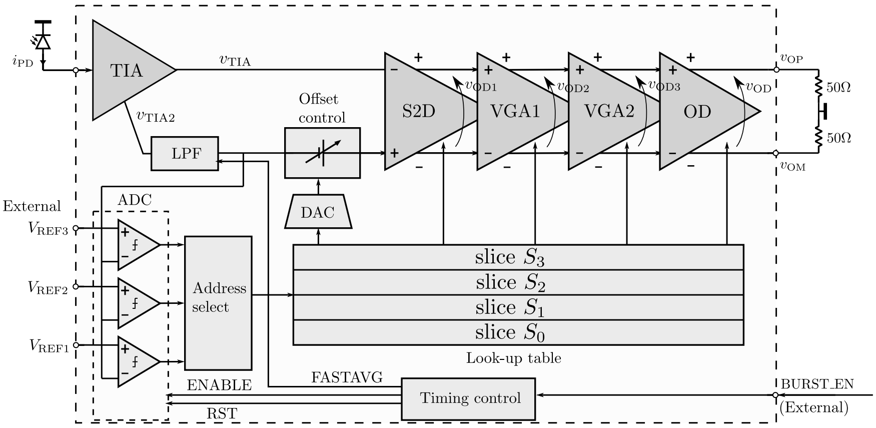

Figure 3.1: Overall architecture of the LBMTIA.

When an upstream burst arrives at the input of the LBMTIA, the average burst power is determined by low-pass filtering the output of the TIA front-end. Upon assertion of an external burst-enable (BURST_EN) signal, this signal is sensed with a flash analog-to-digital converter (ADC) with 3 externally applied reference levels. The ADC then selects the corresponding slice in the LUT. The same signal is also used as a reference voltage for the S2D. This setup allows to perform rapid AGC and AOC during a short preamble at the start of each burst.

As shown in Chapter 2, using low-pass filtering to detect the average burst power faces a difficult trade-off. On one hand, to ensure rapid (within a few 10s of nanoseconds) measurement of the average burst power a sufficiently fast (high bandwidth) low-pass filter is required. On the other hand, the detected average burst signal level is used as a reference to perform S2D conversion. Hence, to avoid excessive baseline wander, a low-pass filter with sufficiently low bandwidth is required.

Here, this trade-off is broken by making the time-constant of the low-pass filter switchable: during the preamble of each burst, the bandwidth of the LPF is set to 130 MHz. After the preamble, during normal data reception, the bandwidth of the LPF is reduced to 0.8 MHz. With this bandwidth, the theoretical power-penalty due to baseline wander in the payload is negligible (e.g. less than 0.03 dB for 31 CID - see Chapter 2) [7]. To avoid baseline wander during the preamble which would make the detected average burst-mode level inaccurate, the preamble contents are required to be balanced, e.g. a 101010... pattern for NRZ, or alternation of the lowest and highest order PAM symbols for PAM-4.

The LBMTIA was designed and fabricated using the 0.25um SiGe:C BiCMOS-technology from NXP, whose bipolar transistors have an f_T of 180GHz. A complete layout of the chip is shown in Fig. 3.2.

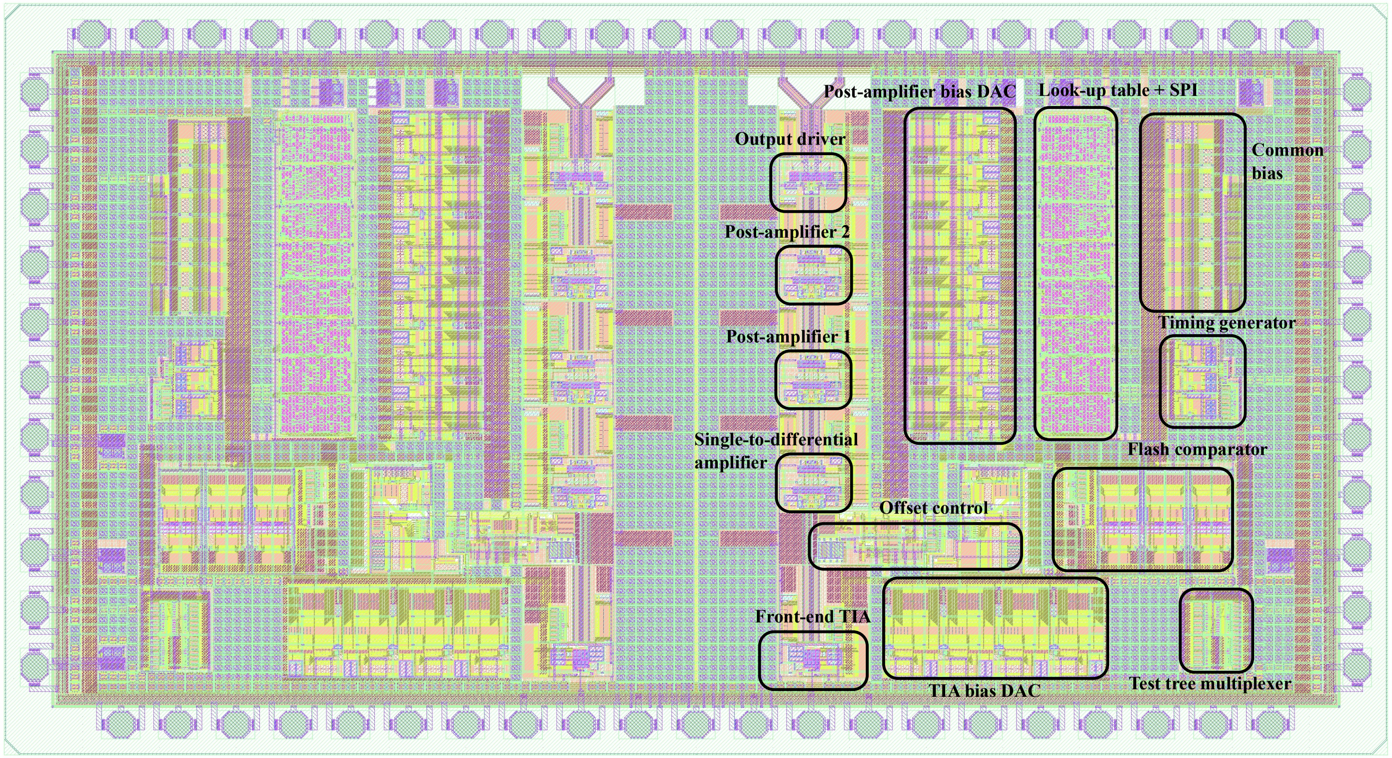

Figure 3.2: Top-level layout of the first-generation LBMTIA. 2 channels are implemented on a die with dimensions 3.62mm × 1.97mm.

3.2 Experimental Results

The receiver is characterized using the setup shown in Fig. 4.26. A MZM is used to modulate the light from a laser source, operating at 1310 nm. It is driven with a high-speed arbitrary waveform generator (AWG), which generates pseudo-random binary sequence (PRBS) $2^{10} - 1$ data, modulated as 25 Gbit/s NRZ or 50 Gbit/s PAM-4 using Gray-mapping. A relatively short pattern was chosen here to limit the length of the burst payload section and hence the needed memory in the pattern AWG.

The burst power is modulated using an SOA driven by a function generator, in sync with the high-speed AWG. The resulting optical signal is split and sent to a reference receiver and our LBMTIA. The chip is wirebond-assembled with the Albis PIN photodetector as shown in Fig. 3.4; its electrical output was measured using a GSSG RF-probe.

Using a real-time-oscilloscope (RTO), the BER of the different burst packets is computed off-line: sampling occurs at a fixed symbol-spaced interval, and the decision levels are chosen optimally. No further digital signal processing (DSP) is used to optimize the eye diagrams for the LBMTIA.

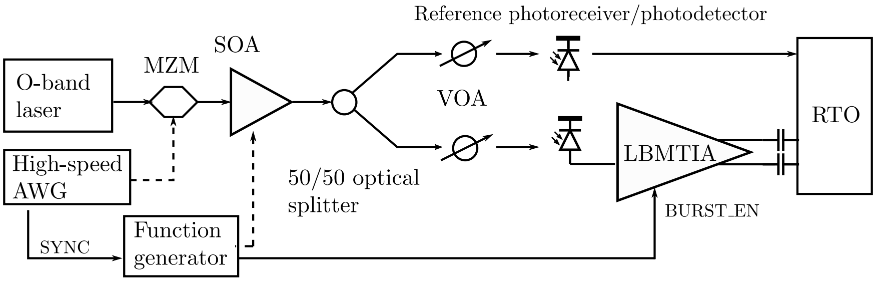

Figure 3.3: Experimental setup used to test the LBMTIA. Burst data AWG: Keysight M8195A, O-band laser source: Tunics T100S-HP, MZM: iXblue MX1300-LN-40, SOA: Inphenix IPSAD1301, Envelope/BURSTEN AWG: Tektronix AFG3102, variable optical attenuator (VOA): Keysight N7762A, DC-coupled reference photoreceiver: HP11982 Lightwave Converter, AC-coupled reference photodetector: Finisar XPDV21X0R, LBMTIA photodetector = Albis PD40, RTO = Keysight DSA-Z 634A.

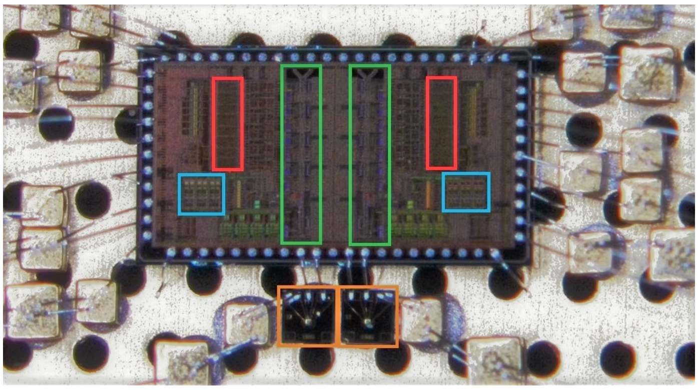

Figure 3.4: Wirebonded printed circuit board (PCB) assembly. Green: datapath, blue: flash ADC, red: LUT. Albis photodetectors are shown in orange. 2 channels are implemented on a die with dimensions 3.62mm × 1.97mm.

In a first step to characterize the performance of the LBMTIA, the BER as a function of optical input power is measured for the four LBMTIA gain- and offset-control settings ($S_3 \rightarrow S_0$) in continuous-mode (no bursts). The fast AGC and AOC lookup circuitry is disabled and the gain- and offset-control settings are applied continuously to the high-speed data path for each BER-curve. The results are shown in Fig. 3.5 for both 25 Gbit/s NRZ and 50 Gbit/s PAM-4.

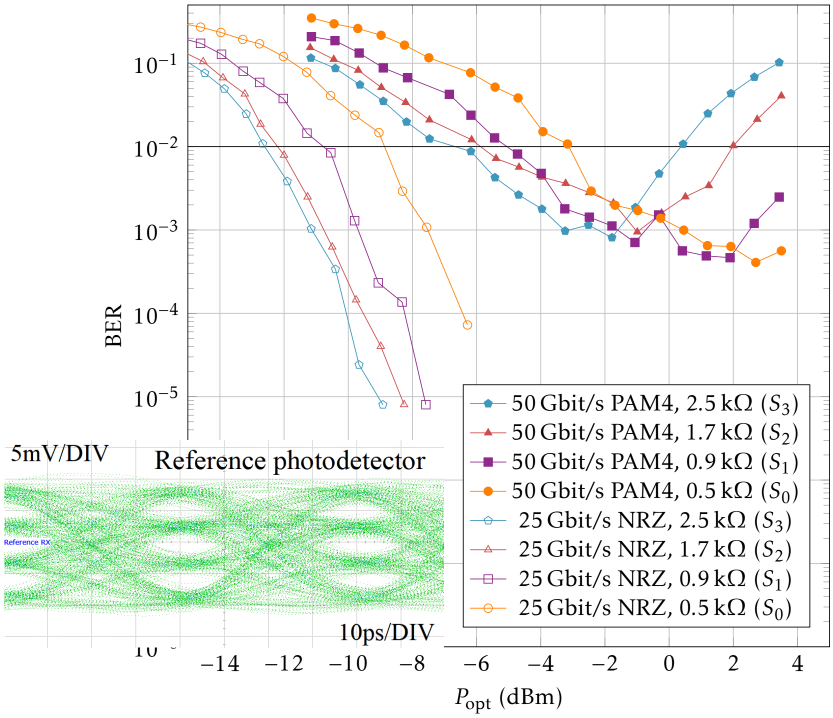

Figure 3.5: BER for NRZ and PAM-4 as a function of received optical input power in continuous-mode, for 4 fixed gain settings of the receiver. Measured extinction ratio of the MZM = 6.9 dB.

A reference BER-level of 1×10^{-2} is chosen with LDPC (17% overhead) in mind (see Table 2.4), according to upcoming 25 Gbit/s and 50 Gbit/s PON-standards [9, 10]. At this level, the best sensitivity for NRZ (achieved at highest gain) is measured to be −12.7 dBm. This reduces for the lower gain settings due to the higher input referred noise current at these settings, of which the lowest was measured to be 4.6 μA. At increasing power levels, no bit errors were measured in 250,000 bits. For PAM-4 and again at the same 1×10^{-2} BER-level, the sensitivity is now −6.6 dBm, close to the theoretical 4.9 dB difference in NRZ and PAM-4 sensitivity. For higher input powers, the BER-level rises again, mainly attributed to the increasing non-linearity of the high-speed data path, compressing the PAM-4 signal.

Note how reducing the gain by switching between gain-settings in the data path now helps to improve the performance for high input powers. By switching between all four gain- and offset slices in the LUT, a continuous-mode input dynamic range of at least 10 dB is achieved. Moreover, at the maximum optical power that could be generated by the testbench, the BER-level is still well below the FEC-limit. Over this range, the lowest achievable BER is 4.1×10^{-4} and the output dynamic range is reduced to 4.3 dB. For comparison with the eye diagrams in Fig. 3.7, a reference eye diagram captured with the Finisar XPDV21X0R 50GHz photodetector using the same transmitter setup is also shown as an inset in Fig. 3.5.

In a next step to characterize the LBMTIA, the reference voltages $V_{\mathrm{REF1,2,3}}$ (which serve to select which of the four slices are used for a particular incoming burst) are calibrated. This is done by setting the pattern AWG to a fixed 101010.. pattern, and generating stepwise stronger bursts. The burst-enable (BURST_EN) signal is applied to the LBMTIA to signal the start and end of the incoming bursts. The resulting burst-mode gain- and offset control can be seen in Fig. 3.6, where the gain is reduced upon assertion of the BURST_EN signal (middle trace) when the optical input signal (upper trace) exceeds selected thresholds.

During measurements it appeared that slice S_2 never activated, attributed to a fabrication fault in the LBMTIA chip assembly. Therefore, the LUT was modified to use only 3 slices. Although the resulting gain-configurations (1.9 kΩ in S_3, 0.8 kΩ in S_1, and 0.3 kΩ in S_0) have caused the output dynamic range to increase to 7.9 dB, demonstrating the burst-mode behavior of the LBMTIA is independent of the actual number of slices. In particular, when a desired input dynamic range is reached, adding more slices will merely reduce the output dynamic range (provided that the minimum and maximum gain can no longer be extended). In a next fabrication iteration of the LBMTIA, the issue can be readily solved.

Finally, the pattern AWG is configured to generate burst-mode data, consisting of a 2000-symbol long 1010-preamble (80 ns), followed by a 16000-symbol long NRZ or PAM-4 PRBS $2^{10}-1$ payload (640 ns).

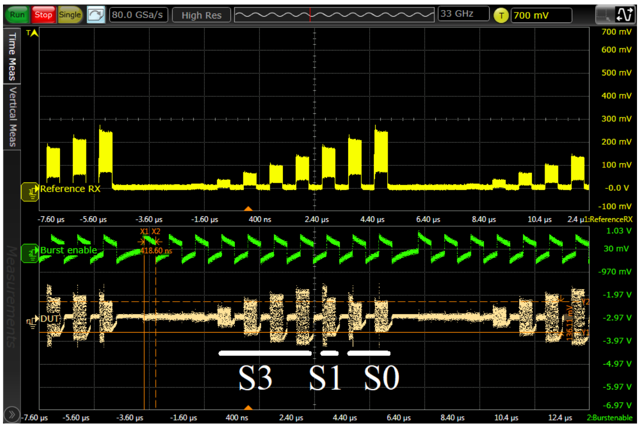

Figure 3.6: DC-coupled reference photoreceiver output voltage, externally applied BURST_EN control signal, and differential output voltage of the LBMTIA.

The SOA is driven to alternate between strong and weak bursts, emulating transmission from 2 distinct ONUs. The bursts are transmitted in rapid succession, with 40 ns of guard time.

In Fig. 3.7 the output voltages of the DC-coupled photoreceiver and the LBMTIA are shown, with a close-up in Fig. 3.8 showing the external BURST_EN and internal control signals (ADC_RST, ADC_EN and FAST_LPF, which are derived from BURST_EN using simple logic and timers).

Upon assertion of the BURST_EN signal, the internal ADC is reset using ADC_RST and the LUT switches to S_3, which is the highest gain setting. Then, during ADC_EN, the average TIA output voltage is sensed and the corresponding slice activated (in this case S_1). Finally, the bandwidth of the low-pass filter is reduced using FAST_LPF. For this process, a total reconfiguration time of 48 ns was needed.

A change in common-mode voltage in the output voltages of the LBMTIA can be noticed, which is due to the change in tail current in the output driver, needed to accomodate a wider input dynamic range. The peak visible at 1.11 μs is due to the drop in optical power,

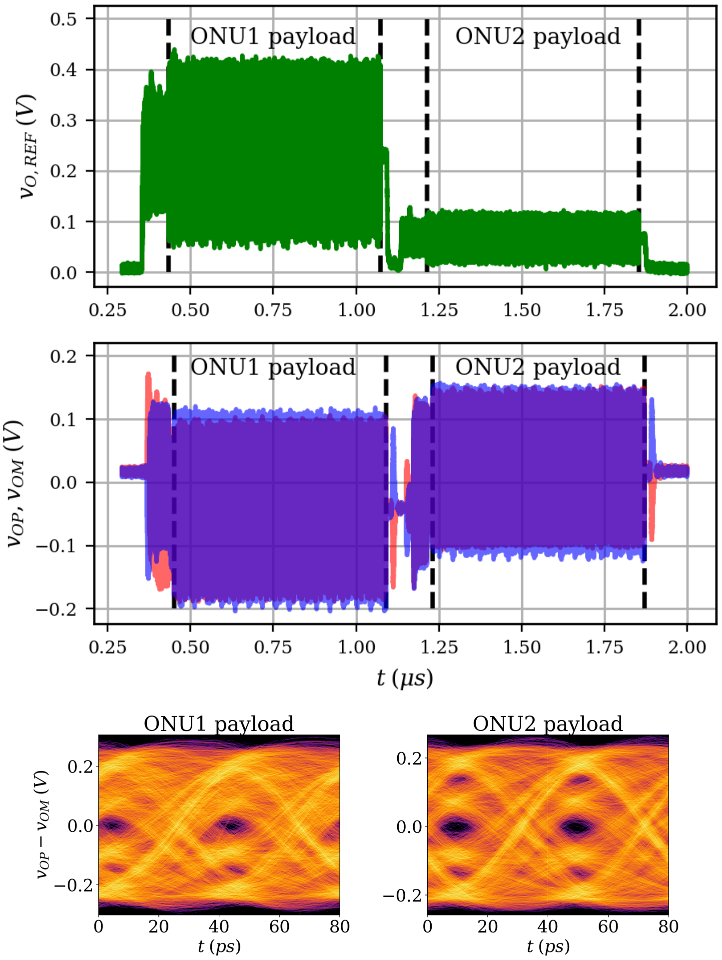

Figure 3.7: Succession of bursts from 2 different ONUs, as seen through the output of the DC-coupled reference photoreceiver and the LBMTIA. $P_{\mathrm{opt}}^{\mathrm{ONU1}} = 5.5\,\mathrm{dBm}$ and $P_{\mathrm{opt}}^{\mathrm{ONU2}} = 0.1\,\mathrm{dBm}$.

10 ns after the last data symbols have been received.

Finally, Fig. 3.7 also shows the PAM-4 eye diagrams for the payload section of each burst. Notice that for the strong burst, the topmost eye is already closed, resulting an overload situation. It is followed by the weaker burst, in which this is not the case.

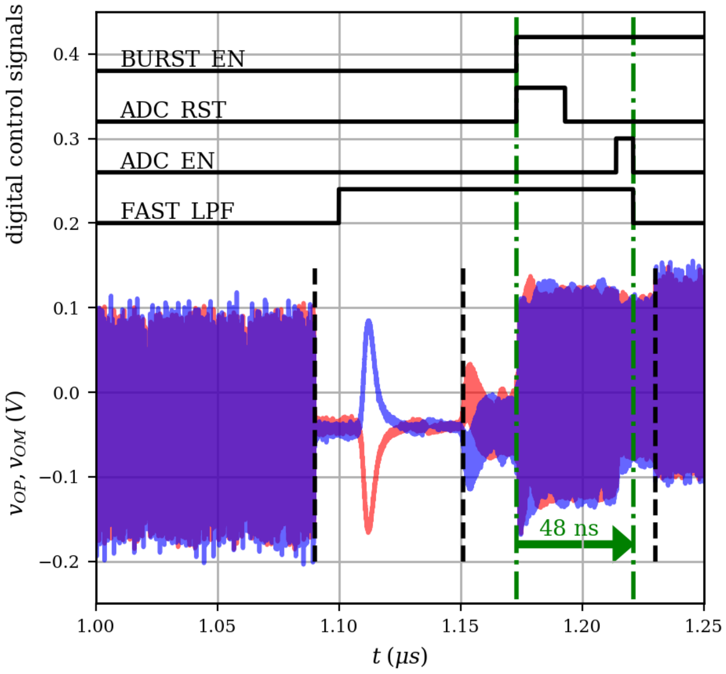

Figure 3.8: Close-up of the strong-weak burst transition in Fig. 3.7, and the internal digital control signals.

With this setup, a number of burst-mode BER-curves are measured. Here, the power of the bursts is swept and the BER in the payload of the second burst is computed. In a first curve, the power of the 2 bursts are set equal: $P_{\text{opt}}^{\text{ONU1}} = P_{\text{opt}}^{\text{ONU2}}$. In the other curve, $P_{\text{opt}}^{\text{ONU1}} = 5.5\,\text{dBm}$ to measure if there is any burst-mode penalty due to a stronger burst preceding the weaker burst. The experiment is performed for both NRZ and PAM-4 payload sections. The resulting BER-curves can be seen in Fig. 3.9.

Despite the reduction of the number of slices, the BER stays below the 1×10^{-2} limit from −13.8 dBm up until at least 3.9 dBm for NRZ, and −5.4 dBm up until 5.5 dBm for PAM-4. The burst-mode penalty due to a strong 5.5 dBm burst is found to be 0.6 dB for the 25 Gbit/s NRZ case, and negligible for the 50 Gbit/s PAM-4 case.

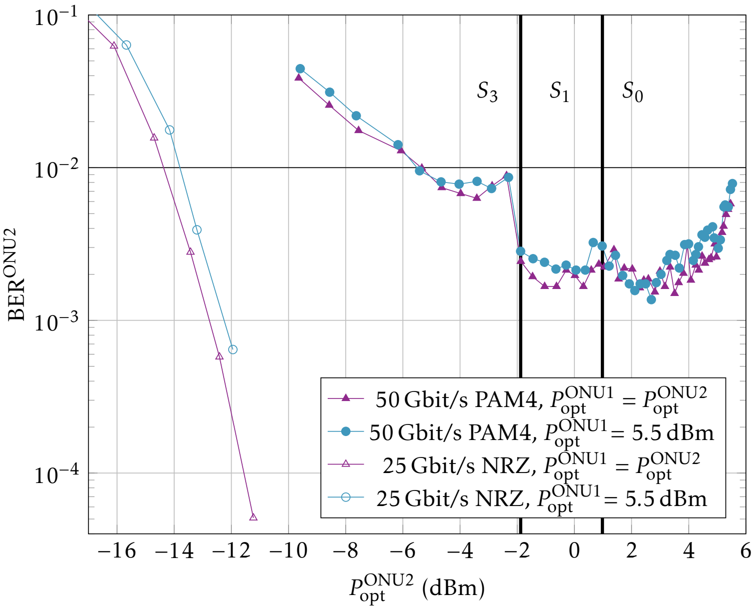

Figure 3.9: Aggregate BER of 5 received ONU2 packets received by the OLT as a function of the optical received power of those packets. $S_0 \rightarrow S_3$ = configuration slices, from weak gain to strong gain.

Note how the measurement results show a 2 dB sensitivity improvement for burst-mode NRZ versus continuous-mode NRZ, as well as a a 1.6 dB penalty for burst-mode PAM-4 versus continuous-mode PAM-4. These penalties cannot necessarily be attributed only to the burst-mode operation itself, but also to drifts in the experimental setup.

3.3 Conclusion

In this chapter, a linear burst-mode receiver is presented capable of receiving 50 Gbit/s PAM-4, targeting upstream transmission in high-rate TDM-PONs. The receiver is demonstrated with a sensitivity level of −13.8 dBm for NRZ and −5.4 dBm for PAM-4, while an input dynamic range of at least 17.7 dB for NRZ and 10.9 dB for PAM-4 was obtained (at the LDPC FEC threshold of 1×10^{-2}). The settling time is measured to be 48 ns with negligible burst-mode penalty on weak bursts from a strong preceding burst. The presented LBMTIA can be used as the front-end of a linear burst-mode receiver, as will be required for upcoming 25 Gbit/s and 50 Gbit/s capable TDM-PONs.

References

[1] J. Zhang, J. S. Wey, J. Yu, Z. Tu, B. Yang, W. Yang, Y. Guo, X. Huang, and Z. Ma, “Symmetrical 50-Gb/s/λ PAM-4 TDM-PON in O-band with DSP and Semiconductor Optical Amplifier Supporting PR-30 Link Loss Budget,” in *2018 Optical Fiber Communications Conference and Exposition (OFC)*, March 2018, pp. 1–3.

[2] J. Zhang, X. Xiao, J. Yu, J. S. Wey, X. Huang, and Z. Ma, “Real-Time FPGA Demonstration of PAM-4 Burst-Mode All-Digital Clock and Data Recovery for Single wavelength 50G PON Application,” in *2018 Optical Fiber Communications Conference and Exposition (OFC)*, March 2018, pp. 1–3.

[3] M. Dalla Santa, C. Antony, G. Talli, and P. D. Townsend, “Power Budget Improvement in Passive Optical Networks Using PAM4 Hierarchical Modulation,” *IEEE Photonics Technology Letters*, vol. 29, no. 20, pp. 1747–1750, Oct 2017.

[4] Xin Yin, J. Verbist, T. De Keulenaer, B. Moeneclaey, J. Verbrugghe, Xing-Zhi Qiu, and J. Bauwelinck, “25Gb/s 3-level burst-mode receiver for high serial rate TDM-PONs,” in *2015 Optical Fiber Communications Conference and Exhibition (OFC)*, March 2015, pp. 1–3.

[5] D. T. van Veen and V. E. Houtsma, “Proposals for Cost-Effectively Upgrading Passive Optical Networks to a 25G Line Rate,” *Journal of Lightwave Technology*, vol. 35, no. 6, pp. 1180–1187, March 2017.

[6] P. Ossieur, C. Melange, T. De Ridder, J. Bauwelinck, B. Baekelandt, X. Qiu, and J. Vandewege, “Burst-Mode Electronic Equalization for 10-Gb/s Passive Optical Networks,” *IEEE Pho-*

tonics Technology Letters, vol. 20, no. 20, pp. 1706–1708, Oct 2008.

[7] E. Säckinger, *Broadband Circuits for Optical Fiber Communication*. Wiley, 2005.

[8] E. Sackinger, *Analysis and Design of Transimpedance Amplifiers for Optical Receivers*. Wiley, 2017.

[9] IEEE P802.3ca 50G-EPON Task Force, "Physical Layer Specifications and Management Parameters for 25Gb/s and 50Gb/s Passive Optical Networks." [Online]. Available: http://www.ieee802.org/3/ca/

[10] V. H. Dora van Veen, "FEC code for 25/50/100G EPON (IEEE P802.3ca 100G-EPON Task Force Meeting)," 2017.

4

A 50Gbit/s PAM-4 Linear Burst-Mode Receiver with Analog AGC/AOC

In the previous chapter, a 50 Gbit/s LBMTIA was presented which uses a look-up table and few discrete datapath settings to obtain coarse AGC/AOC. Mainly developed as a first-generation LBMTIA, many signals such as the SOB and the power level comparisons are provided externally, to maximize the flexibility in experiments. By using a rather low gain front-end transimpedance, very strong input signals can be received without overloading the LBMTIA. As a result, many aspects of this receiver still have lots of room for improvement.

The experience and insights gained during the development and characterization of this LBMRX were used in the development of a second-generation, fully-featured LBMRX operating at 25 Gbaud NRZ or PAM-4. As opposed to before, the gain of the post-amplifier stages and DC-offsets of the datapath can be quickly adjusted in a continuous manner from one burst to the next through combined feedforward (providing rapid settling) and feedback (providing accurate gain and offset control) AGC and AOC loops. Both are driven by rapid detection of average and RMS-values of the input signal, rendering this design suitable for operation at 25 Gbaud compared to peak detector based designs as described in Chapter 2. In addition, sample-and-hold capacitors are used to fix the state of the AGC and AOC loops during the payload section of each burst, to eliminate the trade-off between settling time and power penalties caused by gain modulation and/or baseline wander.

Several circuits were added to detect and interface the SOB and EOB signals. The receiver has an improved sensitivity level, a wider input dynamic range and a near-zero output dynamic range, all while maintaining linear operation.

In this chapter, the architecture and circuit implementations of this LBMRX are described in detail. Then, the performance is validated both in continuous-mode and in burst-mode for NRZ and PAM-4 modulation formats. The detection time of the internal SOB and EOB detectors is characterized, as well as the photocurrent monitor accuracy. This contents of this chapter are based on the paper, entitled:

G. Coudyzer, P. Ossieur, J. Bauwelinck, and X. Yin, "A 50 Gbit/s PAM-4 Linear Burst-Mode Receiver with Analog Gain- and Offset Control in 0.25 µm SiGe:C BiCMOS," *IEEE Journal of Solid State Circuits*, Sept. 2019 [Submitted].

4.1 Receiver Architecture

Fig. 4.1 shows the overall architecture of the proposed BMRX. The photocurrent i_{PD} generated by a photodiode is converted into a voltage v_{TIA} using a single-ended TIA (shunt-feedback topology) with a fixed transimpedance of 480 Ω. The signal is converted into a differential signal using a S2D converter (differential-pair topology) with an attenuation switchable between 0 dB and 6 dB. Then, two VGAs (Gilbert-cell topology) are used to regulate the output swing to constant levels. A gain of up to 7 dB each can be configured with the differential control currents $i_{\mathrm{CTLx}} \triangleq i_{\mathrm{CTLxP}} - i_{\mathrm{CTLxM}}$ $(x = 1, 2)$. An output driver (differential-pair with emitter degeneration feedback) is used to drive a differential 50 Ω interface and adds an additional 1.6 dB of gain.

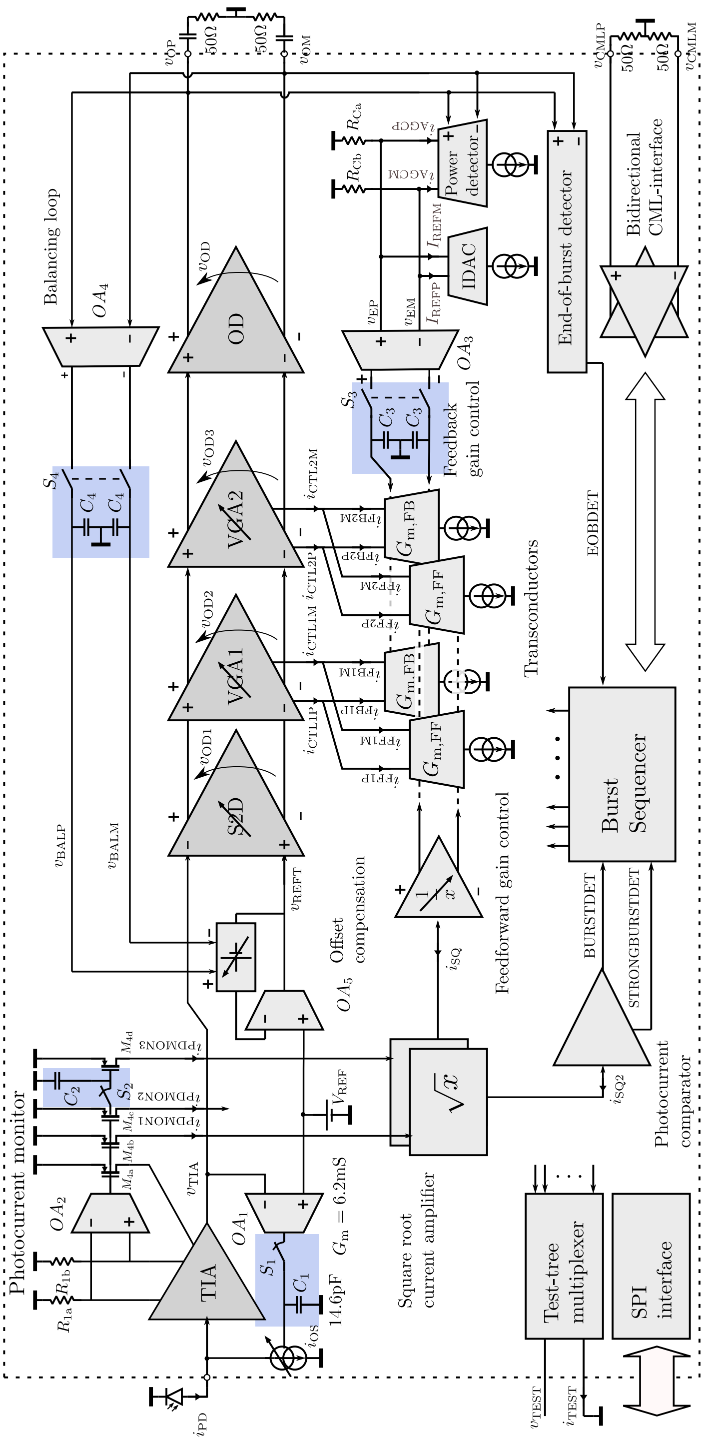

Figure 4.1: Overall architecture of the LBMRX.

The burst-mode operation is illustrated in Fig. 4.2. When the LBMRX is in idle mode (switch S_1 and S_2 closed, S_3 and S_4 opened), a feedback loop using OPAMP OA_1 keeps v_{TIA} around a chosen V_{REF} by sinking an input offset current i_{OS}. The loop is made sufficiently fast (GBWP of 1.4 GHz and DC loop-gain of 80 dB) to quickly respond to an incoming burst. When a burst is received, the loop quickly re-centers v_{TIA} around V_{REF}: this ensures that a symmetrical input is provided to the S2D amplifier. This rapid acquisition requires that the preamble symbol pattern does not contain long sequences of consecutive identical digits, which is achieved using a 101010.. pattern.

At the same time, a replica of the average photocurrent (= i_{PDMON3}) (during the preamble phase) is used to reduce the gain in the datapath for stronger bursts by creating an inversely proportional drive current for the VGAs by using analog translinear square root and inversion circuits and transconductors $G_{\mathrm{m,FF}}$.

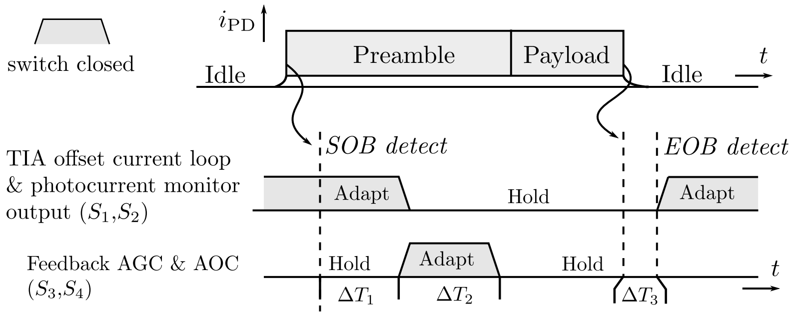

Figure 4.2: Burst timing diagram.

A second replica (= i_{PDMON1}) is used in a current comparator as a SOB detector. In order to increase the precision at weaker photocurrents, the square root circuit from the feedforward AGC is conveniently reused here (= i_{SQ2}). The SOB detector triggers a burst sequencer, which opens S_1 and S_2 after a fixed time delay ΔT_1 (digitally configurable from 6 ns to 14.3 ns).

The charges stored in the sample-and-hold capacitors C_1 and C_2 are now used for input offset correction and feedforward gain control for the remainder of the burst. After the time delay ΔT_1 has elapsed, switches S_3 and S_4 are closed, activating two feedback loops.

In the first loop the output of a power detector (represented by $i_{\mathrm{AGC}} \triangleq i_{\mathrm{AGCP}} - i_{\mathrm{AGCM}}$) is compared to a reference level (represented by $I_{\mathrm{REF}} \triangleq I_{\mathrm{REFP}} - i_{\mathrm{IREFM}}$). The resulting error current is converted into a voltage (represented by $v_{\mathrm{E}} \triangleq v_{\mathrm{EP}} - v_{\mathrm{EM}}$) and amplified by OPAMP OA_3, which modifies the drive current (and gain) of the VGAs using a second transconductor $G_{\mathrm{m,FB}}$ placed in parallel with the feedforward transconductors $G_{\mathrm{m,FF}}$.

The second loop (driven by OPAMP OA_4) is responsible for removing any unwanted residual DC offset voltage in v_{OD} caused by mismatch in the later stages of the datapath, which is done by adding a voltage in series with V_{REF} ($= v_{\mathrm{REFT}}$). These two loops are made active for a brief period of time ΔT_2 (digitally configurable from 14.5 ns to 69.3 ns), after which their state is fixed for the remainder of the burst by using sample-and-hold capacitors C_3 and C_4. All control loops are now fixed and the LBMRX is ready to receive the payload section of the burst.

Meanwhile, the EOB detector is activated, which monitors the differential output signal v_{OD} for line inactivity. After the EOB is detected, an additional time delay ΔT_3 (digitally configurable from 2.9 ns to 17.1 ns) is used to ensure that the SOB does not immediately re-triggers while the receiver is recovering from a burst. The EOB detector resets the burst sequencer, resetting the different control loops and prepares the LBMRX for the next burst. Note that during operation, only a single value of ΔT_1, ΔT_2 and ΔT_3 are chosen; its tunability is merely added for debugging and optimization purposes.

Through a bidirectional current-mode logic (CML) interface the SOB and EOB signals can be externally provided if desired, as well as monitoring the status of these when the on-chip detectors are used. Additionally, the receiver can be reconfigured to support continuous-mode operation (e.g. for downstream PON transmission), in which a second set of slower OPAMP's (gain-bandwidth products around 1 MHz) are used for the balancing and input offset control loops (OA_1,OA_3). In this case, the switches S_1 and S_4 are always closed. The gain is fixed by applying constant differential control currents i_{CTLx} ($x = 1, 2$) into the VGAs instead of being driven by the burst-mode circuitry.

The chip is implemented in a 0.25 µm SiGe:C BiCMOS-technology, whose bipolar transistors have an f_T of 180 GHz. A complete layout of the chip is shown in Fig. 4.3. A power consumption breakdown of the chip operating in burst-mode is given in Section 4.1. In total, using a supply voltage of 2.5 V, the receiver consumes 280 mW of power, of which over 65 % is used for the data path.

Block	Power	Contribution
Datapath	184 mW	65.8 %
AGC circuits	41 mW	14.6 %
AOC circuits	16 mW	5.7 %
CML-interface	24 mW	8.6 %
SOB/EOB detection	7 mW	2.5 %
Other	8 mW	2.8 %
Total	280 mW	100 %

Table 4.1: Power consumption breakdown of the LBMRX.

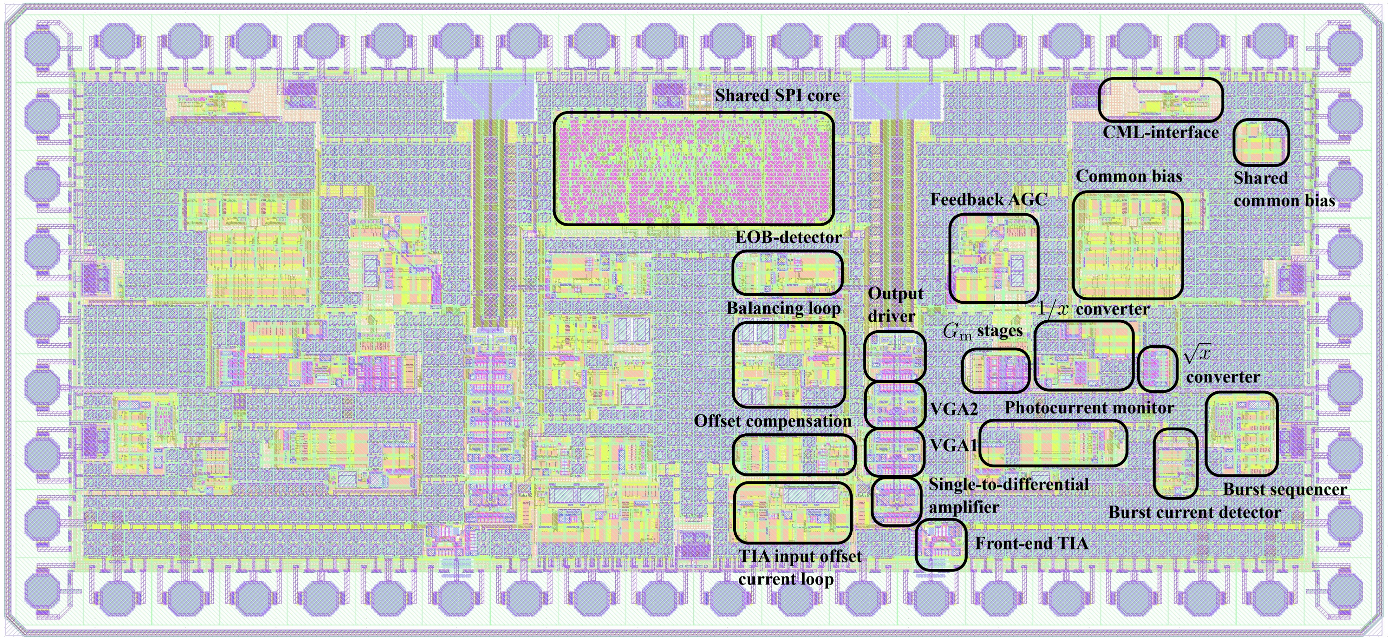

Figure 4.3: Top-level layout of the second-generation LBMRX. 2 channels are implemented on a die with dimensions 3.05mm × 1.4mm.

Front-End Transimpedance Amplifier

The TIA converts the input photocurrent into a single-ended output voltage and is implemented using a commonly used shunt-feedback topology [1, 2], as shown in the non-shaded area of Fig. 4.4.

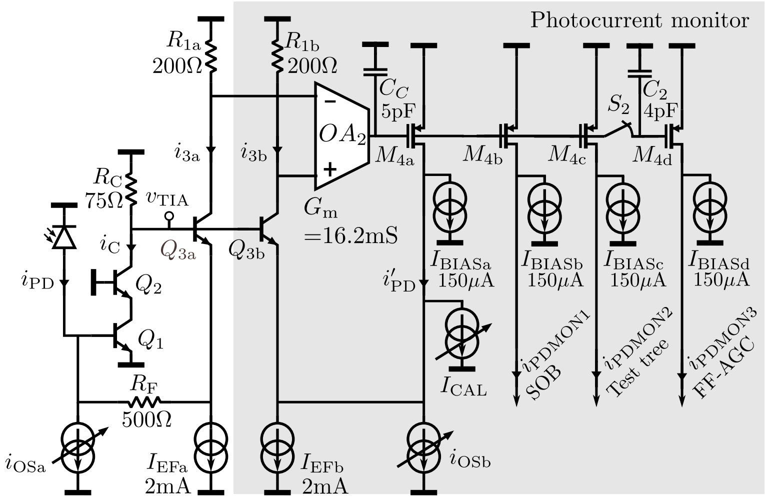

Figure 4.4: Transimpedance amplifier and photocurrent monitor.

The DC output voltage v_{TIA} and the collector current i_C of input transistor Q_1 of the TIA are determined through self-biased operation and (neglecting base currents) can be calculated as:

$$v_{TIA} = v_{BE1} - R_F i_{PD} + R_F i_{OSa} + v_{BE3a} \tag{4.1}$$

$$i_C = \frac{V_{DD} - v_{TIA}}{R_C} \tag{4.2}$$

Because $i_{OS} \triangleq i_{OSa} = i_{OSb}$ are controlled by the offset feedback loop with opamp OA_1 (see Fig. 4.1), the average value of v_{TIA} is centered around V_{REF}. Its value must be chosen to satisfy the input common-mode range of the S2D amplifier, the allowed output swing in the positive direction (limited by $V_{DD} - v_{TIA}$) or the allowed output swing in the negative direction (limited by saturation of cascode transistor Q_2).

The low-frequency, small-signal transimpedance R_t can be controlled through the feedback operation of R_F around a common-emitter amplifier:

$$R_\mathrm{t} = -R_\mathrm{F}\frac{T_\mathrm{dc}}{1+T_\mathrm{dc}} \tag{4.3}$$

where the DC loop gain T_dc can be written as

$$T_\mathrm{dc} = \frac{g_\mathrm{m1}R_\mathrm{C}}{1+g_\mathrm{m1}R_\mathrm{E}} = \frac{i_\mathrm{C1}R_\mathrm{C}}{U_T + i_\mathrm{C1}R_\mathrm{E}} = \frac{V_\mathrm{DD}-v_\mathrm{TIA}}{U_T + (V_\mathrm{DD}-v_\mathrm{TIA})\frac{R_\mathrm{E}}{R_\mathrm{C}}} \tag{4.4}$$

In this equation, g_m1 is the transconductance of Q_1 and R_E is its internal emitter resistance. Care must be taken to ensure that sufficient loop gain is present for the entire output range of v_TIA.

Each node in the circuit attributes to a different pole in the approximated frequency response in the loop gain:

$$T \approx T_\mathrm{dc}\underbrace{\frac{1}{1+sC_\mathrm{I}R_\mathrm{F}}}_{\substack{\text{dominant}\\\text{input pole}}}\underbrace{\frac{1}{1+sC_\mathrm{p1}/g_\mathrm{m2}}}_{\substack{\text{cascode}\\\text{input pole}}}\underbrace{\frac{1}{1+sC_\mathrm{p2}R_\mathrm{C}}}_{\substack{\text{output}\\\text{pole}}}\underbrace{\frac{1}{1+sC_\mathrm{p3}/g_\mathrm{m3a}}}_{\substack{\text{emitter}\\\text{follower pole}}} \tag{4.5}$$

In this equation, $C_\mathrm{px}(x=1,2,3)$ represents the parasitic capacitances at each of the relevant circuit nodes, C_I represents the total capacitance at the input of the TIA (photodiode, bondpad, input transistor and parasitics), g_m2 is the transconductance of the cascode transistor Q_2, and g_m3a is the transconductance of the emitter follower transistor Q_3.

The feedback loop gain T must be carefully designed to provide adequate bandwidth while limiting the amount of peaking in Eq. (4.3), and maintaining stability. Through careful layout and proper sizing, the parasitic poles can be shifted to higher frequencies, which allows us to approximate the TIA bandwidth from the GBWP constructed from the dominant pole in the loop gain expression:

$$BW_{R_t} \approx GBWP_T \approx \frac{T_\mathrm{dc}}{2\pi R_\mathrm{F}C_\mathrm{I}} \tag{4.6}$$

Given a specified input capacitance C_I, increasing the bandwidth requires us to increase the loop gain (which increases power consumption) or reduce the transimpedance through R_F (which increases the input-referred noise).

Here, the receiver is designed for 25 Gbaud NRZ or PAM-4 operation. As such, a ideal bandwidth of $\frac{2}{3}25\,\mathrm{GHz} \approx 16\,\mathrm{GHz}$ is targeted [1]. Assuming an input capacitance of $C_\mathrm{I} \approx 200\,\mathrm{fF}$ (100 fF for the photodiode and 100 fF to account for input node parasitics), this bandwidth can be realized with a loop gain of $T_\mathrm{dc} \approx 20\,\mathrm{dB}$ and a shunt resistance $R_\mathrm{F} = 500\,\Omega$.

For an input current range of $i_\mathrm{PD} = 0 \cdots 1.6\,\mathrm{mA}$ and proper DC-offset current subtraction, an swing of $\pm 0.8\,\mathrm{mA} \cdot R_\mathrm{F} = \pm 0.4\,\mathrm{V}$ is to be expected around v_TIA. Choosing 1.85 V as the quiescent TIA output voltage v_TIA leaves sufficient margin on both sides when the supply voltage is 2.5 V and the base voltage of Q_2 is set to 1.8 V. With $v_\mathrm{BEx} \approx 0.8\,\mathrm{V}$, obtaining this v_TIA requires around 270 µA of quiescent offset current in i_OSa.

Notice that shifting the TIA output voltage by introducing a larger input offset current i_OSa introduces extra noise, directly in parallel with the input-referred noise of the TIA. Its contribution can be estimated by assuming an NMOS transistor in strong inversion (with $g_\mathrm{m}/i_\mathrm{OS} \approx 10$) as the output of the current source:

$$S_{i_n,i_\mathrm{OS}}(f) = 4kT\frac{2}{3}\left(\frac{g_\mathrm{m}}{i_\mathrm{OS}}\right)i_\mathrm{OS} = 3 \times 10^{-23}\mathrm{A}^2/\mathrm{Hz} \tag{4.7}$$

Assuming a noise bandwidth equal to the targeted 3dB-bandwidth above, an input-referred noise of 0.7 µA is obtained. A lower bound on the input-referred noise current of the TIA itself on the other hand, can be calculated as:

$$S_{i_n,\mathrm{TIA}}(f) = \frac{4kT}{R_F} = 3.3 \times 10^{-23}\mathrm{A}^2/\mathrm{Hz} \tag{4.8}$$

which is equivalent to an input-referred noise current of 0.75 µA. The input offset current thus introduces a significant noise penalty. limiting the sensitivity of the TIA. Finally, the emitter followers Q_3a and Q_3b are sized with a bias current of 2 mA (keeping a high f_T and sufficient voltage drop over R_1a and R_1b in mind).

Next, the TIA input branch is iteratively optimized around these initial sizings w.r.t. maximizing TIA bandwidth and minimizing the input-referred noise current, leading to an optimal collector current $i_{C1} = 8.7\,\mathrm{mA}$, an input transistor with $R_E \approx 6\,\Omega$ and a collector resistance $R_C = 75\,\Omega$. The resulting frequency response of the open-loop gain T and the closed-loop transimpedance R_t is shown as the black curves in Fig. 4.5.

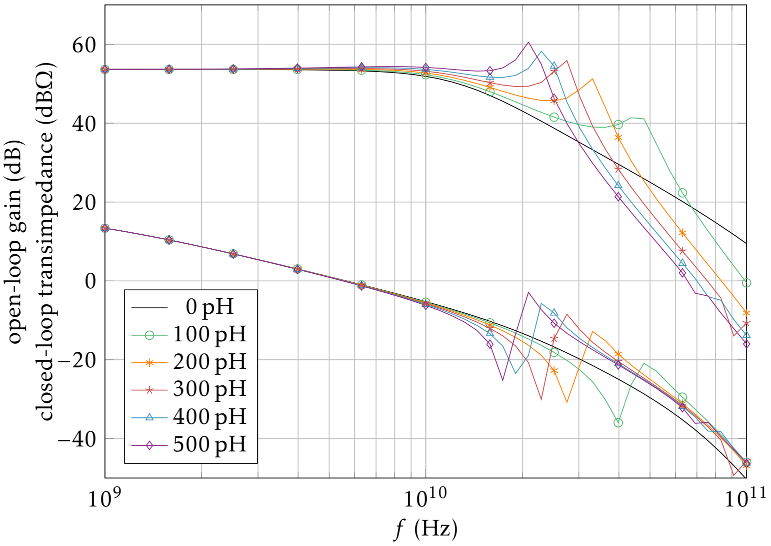

Figure 4.5: Simulated frequency response of the transimpedance R_t (top) and loop gain T (bottom) of the front-end TIA for different self-inductances of the bondwire.

The simulated transimpedance of the front-end TIA is $R_t = 480\,\Omega$, the simulated bandwidth is 12 GHz, and the simulated DC loop gain is $T_{dc} = 17.9\,\mathrm{dB}$. Notice that both the GBWP of the loop gain and the resulting bandwidth of the TIA are significantly lower than expected. Luckily, the bandwidth of the TIA can be increased by advantageously employing the self-inductance of the bondwire at the TIA input. Additionally in Fig. 4.5, the simulated frequency response for several different bondwire inductances are shown. Between 300 and 400 pH, an optimum front-end TIA bandwidth of 26.5 GHz is obtained. Due to the large manufacturing variations of wirebonding, further fine-tuning is of little added value.

The linearity of the receiver is examined through total harmonic distortion (THD) simulations: Fig. 4.6 shows the THD as a function of the front-end TIA output swing when the bias point is chosen as 1.85 V, which remains below 3 % for output swings up to at least 900 mV.

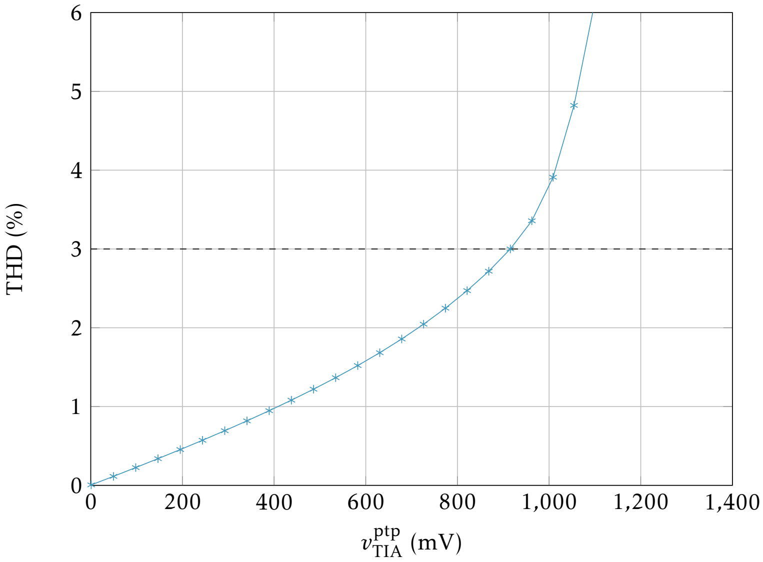

Figure 4.6: Simulated THD of the front-end TIA stage as a function of the peak-to-peak front-end TIA output swing v_{TIA}.

Photocurrent Monitor

To generate the SOB and to set the feedforward AGC path, an estimate of the average photocurrent is necessary. This can be done at the cathode of the photodiode but requires additional interfacing and is not trivial when using high-voltage APD devices. Alternatively, the photocurrent can be extracted from i_{OS} but requires that $V_{\mathrm{REF}} = v_{\mathrm{TIA}}$. Instead, in the proposed receiver the photocurrent estimate is extracted by replication of the emitter follower current instead in the shaded area of Fig. 4.4.

To reconstruct the average of the photocurrent i_{PD}, note how the collector current $i_{3\mathrm{a}}$ of $Q_{3\mathrm{a}}$ equals $I_{\mathrm{EFa}} + i_{\mathrm{OSa}} - i_{\mathrm{PD}}$ (neglecting base currents). To copy this current, a replica emitter follower branch ($Q_{3\text{b}}$ - I_{EFb}) is added to the main shunt-feedback TIA (common-emitter input stage Q_1, cascode Q_2 and R_C followed by emitter follower $Q_{3\text{a}}$), with $Q_{3\text{b}}$ sharing the same base voltage v_{TIA} as $Q_{3\text{a}}$. Two matched resistors $R_{1\text{a}}$ and $R_{1\text{b}}$ are added in the collectors of emitter followers $Q_{3\text{a}}$ and $Q_{3\text{b}}$. Using OPAMP OA_2 which controls the gate voltage of PMOS current source $M_{4\text{a}}$, the current through $Q_{3\text{b}}$ is adjusted such that $i_{3\text{a}} \approx i_{3\text{b}}$. Note how the current generated by the PMOS $M_{4\text{a}}$ now contains the (averaged within the loop bandwidth) photocurrent i_{PD}. This circuit allows accurate copying of the average photocurrent over a wide dynamic range compared to e.g. simple current mirroring. By copying the output transistor M_{4a}, several replicas of the average photocurrent i_{PDMONx} $(x = 1,2,3)$ can be created.

Because a new photocurrent estimate is needed at the start of every burst, the circuit needs to settle very quickly. Its settling time can be related to the GBWP of the feedback loop, which can be approximated by only considering the dominant pole at the output of OA_2:

$$GBWP = \frac{G_{\text{m}} g_{\text{m4a}} R_{1\text{b}}}{2\pi (C_{\text{C}} + C_2)} \tag{4.9}$$

where G_{m} is the transconductance of OA_2 and g_{m4a} the transconductance of MOSFET $M_{4\text{a}}$. Again, the simulated GBWP is significantly lower than the approximated value: Fig. 4.7 shows the frequency response of the loop gain for zero and maximum input current $i_{\text{PD}} = 0.8\,\text{mA}$.

The lowered DC loop gain at the maximum current is due to a reduction in the output resistance R_{o} of OA_2, caused by a shift in operating point. The feedback loop operates with a nominal GBWP of 145 MHz to 295MHz at the highest photocurrent, and a DC loop gain of at least 22 dB. The worst-case phase margin was simulated as 57°.

Notice that after the loop has settled, S_2 is opened, removing part of the compensation capacitance C_2. Care must be taken to ensure that the loop still remains stable under these conditions. This is verified through simulation: when the switch is opened, the loop remains stable with a phase margin of 45°.

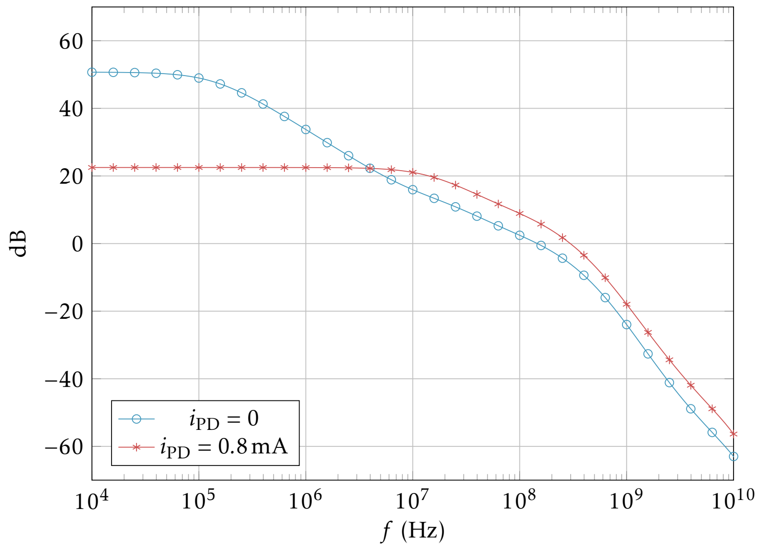

Figure 4.7: Simulated frequency response of the loop gain of the photocurrent monitor.

At weak photocurrents, base currents can no longer be neglected. As Q_1 carries a strong collector current, its base current significantly reduces the replicated photocurrent i'_{PD}. The static error can be zeroed by adding a current I_{CAL} (generated by an 8-bit current DAC) in parallel with i'_{PD}, which is then replicated into i_{PDMONx} ($x = 1, 2, 3$). Fig. 4.8 shows the relative error (i_{PDMON2} versus the average i_{PD}) of the photocurrent monitor, indicating that by changing I_{CAL} the relative error can be minimized, improving the accuracy of the feedforward gain correction. In addition, part of the calibration current I_{CAL} can be used to fine-tune the feedforward AGC: this part of the current will be denoted in the next section as I_H.

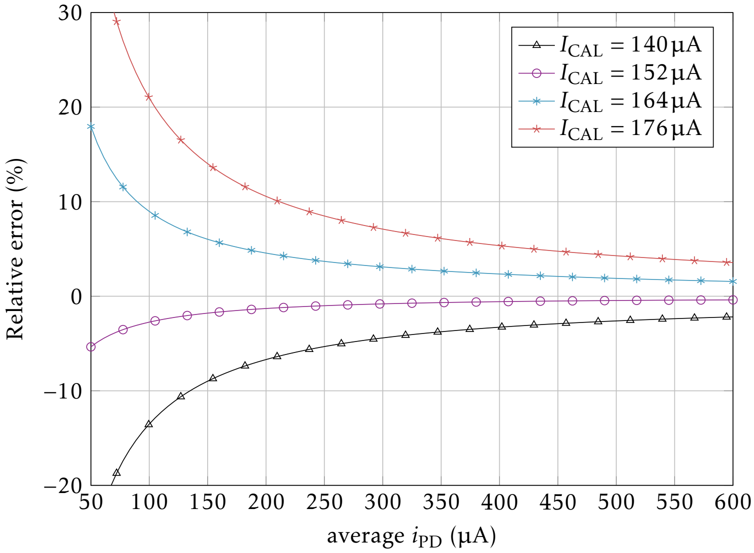

Figure 4.8: Simulated photocurrent estimate i_{PDMON2} versus the average of the photocurrent i_{PD} for different I_{CAL} settings.

Feedforward Automatic Gain Control

At the start of each burst, the estimate i_{PDMON3} of the average photocurrent is used to reduce the gain of the VGAs through a feedforward path. This is done to prevent clipping in the datapath, which would severely distort the input signal and would cause the feedback AGC loop to become intolerably slow when strong bursts are received (as explained in Chapter 2). However, such a feedforward AGC path requires an inversely proportional drive current to be generated. In practice, this path is implemented using the translinear circuits shown in Fig. 4.9 and Fig. 4.10. In these circuits, the photocurrent $i_{\mathrm{PDMON3}} \approx i_{\mathrm{PD}}^{\mathrm{avg}} + I_{\mathrm{H}}$ is converted into:

$$i_{\mathrm{SQ}} = \sqrt{i_{\mathrm{PDMON3}} I_{\mathrm{SQRT}}} \approx \sqrt{(i_{\mathrm{PD}}^{\mathrm{avg}} + I_{\mathrm{H}}) I_{\mathrm{SQRT}}} \tag{4.10}$$

$$i_{\mathrm{A}} = I_{\mathrm{DIV2}} - \frac{I_{\mathrm{DIV1}} I_{\mathrm{DIV2}}}{\sqrt{(i_{\mathrm{PD}}^{\mathrm{avg}} + I_{\mathrm{H}}) I_{\mathrm{SQRT}}}} \tag{4.11}$$

$$i_{\mathrm{B}} = I_{\mathrm{DIV2}} + \frac{I_{\mathrm{DIV1}} I_{\mathrm{DIV2}}}{\sqrt{(i_{\mathrm{PD}}^{\mathrm{avg}} + I_{\mathrm{H}}) I_{\mathrm{SQRT}}}} \tag{4.12}$$

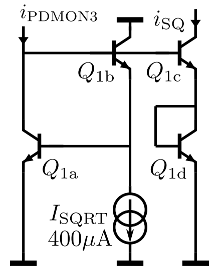

Figure 4.9: Feed-forward AGC $\sqrt{x}$ circuit.

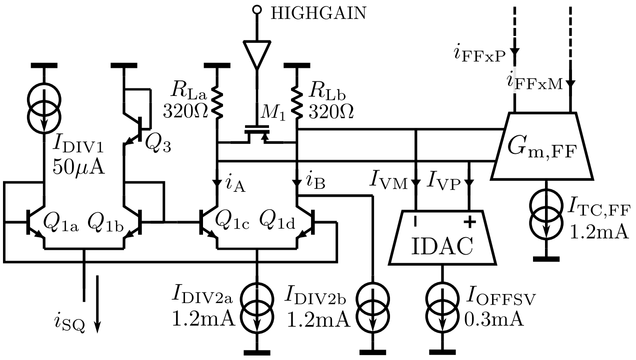

Figure 4.10: Feed-forward AGC $1/x$ circuit.

With $I_{\text{DIV2a}} = I_{\text{DIV2b}} \triangleq I_{\text{DIV2}}$. Optionally, a positive or negative offset can be added ($I_{\text{V}} \triangleq I_{\text{VP}} - I_{\text{VM}}$) to fine-tune the feedforward AGC precision if desired. These currents are then converted into a differential voltage using load resistors $R_{\text{La}} = R_{\text{Lb}} \triangleq R_{\text{L}}$ (ignoring M_1 for now), driving the $G_{\text{m,FF}}$-transconductor to obtain the differential feedforward drive current $i_{\text{FFx}} \triangleq i_{\text{FFxP}} - i_{\text{FFxM}}$ ($x = 1, 2$):

$$i_{\text{FFx}} = 2R_L G_{\text{m,FF}} \left(\frac{I_{\text{DIV1}} I_{\text{DIV2}}}{\sqrt{(i_{\text{PD}}^{\text{avg}} + I_{\text{H}}) I_{\text{SQRT}}}} - I_{\text{V}} \right) \tag{4.13}$$

When the gain in the VGAs is assumed to be linearly proportional with this drive current, the output swing of the LBMRX can be written as:

$$v_{\text{OD}}^{\text{ptp}} = i_{\text{PD}}^{\text{ptp}} R_t A_{\text{S2D}} K_{\text{VGA}}^2 \left(i_{\text{FFx}} + i_{\text{FBx}} \right)^2 A_{\text{OD}} \tag{4.14}$$

In which R_t is the transimpedance of the front-end TIA, A_{S2D} the gain of the S2D converter, K_{VGA} the gain proportionality constant of the VGAs and A_{OD} the gain of the output driver. Combining Eq. (5.1) and Eq. (5.2) while zeroing the feedback contribution $i_{\mathrm{FBx}} \triangleq i_{\mathrm{FBxP}} - i_{\mathrm{FBxM}}$ $(x = 1,2)$, as well as zeroing the optional input and output offset currents I_{H} and I_{V}, gives:

$$\begin{aligned} v_{\mathrm{OD}}^{\mathrm{ptp}} &= \frac{i_{\mathrm{PD}}^{\mathrm{ptp}}}{i_{\mathrm{PD}}^{\mathrm{avg}}} R_{\mathrm{t}} A_{\mathrm{S2D}} K_{\mathrm{VGA}}^2 \frac{4R_L^2 G_{\mathrm{m,FF}}^2 I_{\mathrm{DIV1}}^2 I_{\mathrm{DIV2}}^2}{I_{\mathrm{SQRT}}} A_{\mathrm{OD}} \\ &= 2\frac{ER-1}{ER+1} R_t A_{\mathrm{S2D}} K_{\mathrm{VGA}}^2 \frac{4R_L^2 G_{\mathrm{m,FF}}^2 I_{\mathrm{DIV1}}^2 I_{\mathrm{DIV2}}^2}{I_{\mathrm{SQRT}}} A_{\mathrm{OD}} \end{aligned}$$

In this equation, ER is the extinction ratio of the received modulated signal. Although the i_{PD} terms have dropped from the equations, the extinction ratio ER can vary from burst to burst, however its penalty in the gain correction is relatively small (e.g. < 2.6 dB for an $ER > 8.2$ dB as defined in the ITU-T G.989.2 PON-standard [3]) and can be corrected using the feedback correction term i_{FBx}.

The switchable PMOS-load M_1 is used to increase the gain of each VGA by 3 dB when the S2D converter attenuates the signal by 6 dB. This is done to reduce overload on the VGAs: by using a fixed-gain front-end TIA, the S2D converter needs to handle a possibly large input signal (up to 800 mV) and has to reduce the signal swing for very strong bursts. Ideally, gain switching should occur within the TIA instead. In this technology however, modifying R_{F} through MOS-switches introduces too many bandwidth limitations. But because only the strongest bursts are attenuated, its impact on the sensitivity is still limited. The switch is then triggered by the burst sequencer when the current $i_{\mathrm{SQ2}} = \sqrt{i_{\mathrm{PDMON1}} I_{\mathrm{SQRT}}}$ exceeds a second configurable threshold level in the current comparator.

Fig. 4.11 shows the differential control current i_{CTLx} $(x = 1,2)$ and resulting output swing $v_{\mathrm{OD}}^{\mathrm{ptp}}$ when only the feedforward AGC is used in combination with a fixed i_{FBx}. At around 350 µA, the gain of the S2D amplifier has been reduced with 6 dB, while the feedforward gain control signals have been increased with 3 dB. A jump in the feedforward-only AGC output swing can be observed, due to the difficulties in matching the on-resistance of M_1 to R_{L}.

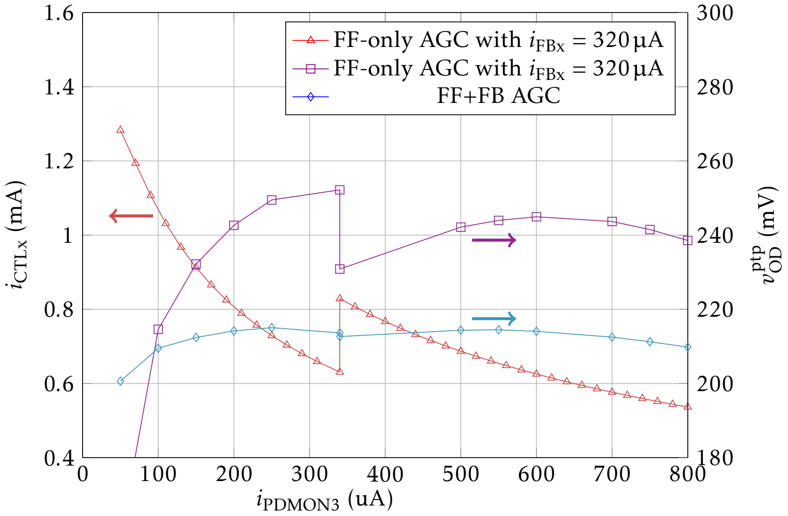

Figure 4.11: Simulated characteristics of the feedforward and feedback AGC loops as a function of the photocurrent i_{PDMON3}.

Feedback Automatic Gain Control

After the feedforward gain control signals have been fixed, a feedback AGC now corrects for any deviations in the relatively inaccurate feedforward path, caused by the burst-to-burst varying extinction ratios, the base current contributions and emitter degeneration effects in the translinear circuits. A Gilbert-cell configured as a power detector (shown in Fig. 4.12) is used to measure the output power of the LBMRX. It is used to estimate the output swing during the 1010.. pattern during the preamble for settling of the feedback AGC loop.

The Gilbert cell generates a current $i_{\mathrm{AGC}} \triangleq i_{\mathrm{AGCP}} - i_{\mathrm{AGCM}}$, proportional to the square of the LBMRX output swing v_{OD}:

$$i_{\mathrm{AGC}} = A_{\mathrm{v}} I_{\mathrm{B1}} \tanh^2\left(\frac{v_{\mathrm{OD}}}{2U_T}\right) \tag{4.15}$$

In this equation, A_{v} is introduced by the buffer in front of the power detector (which attenuates by 1.2 dB). The signal i_{AGC} is then averaged through the bandwidth of the feedback loop, resulting in an average $i_{\mathrm{AGC}}^{\mathrm{avg}}$. A closed-form expression is difficult to obtain; instead its numerical evaluation is shown in Fig. 4.13, for a sinusoidal

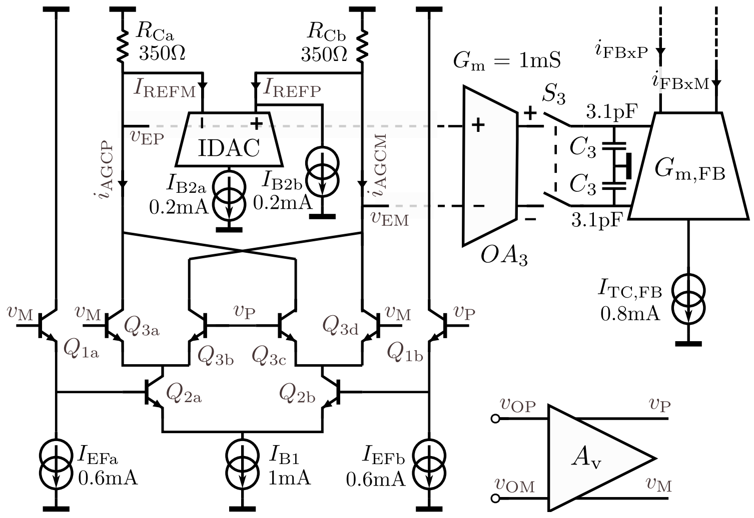

Figure 4.12: Feedback AGC implementation.

1010.. preamble input signal $v_{\mathrm{OD}} = \frac{1}{2}v_{\mathrm{OD}}^{\mathrm{ptp}}\sin(2\pi f t)$, as well as for a constant DC input signal $v_{\mathrm{OD}} = \frac{1}{2}v_{\mathrm{OD}}^{\mathrm{ptp}}$.

The average current $i_{\mathrm{AGC}}^{\mathrm{avg}}$ is compared to a reference level $I_{\mathrm{REF}} \triangleq I_{\mathrm{REFP}} - I_{\mathrm{REFM}}$ (digitally configurable using a current DAC) and converted into a voltage $v_{\mathrm{E}} \triangleq v_{\mathrm{EP}} - v_{\mathrm{EM}}$ through resistors $R_{\mathrm{Ca}} = R_{\mathrm{Cb}} \triangleq R_{\mathrm{C}}$. The error term is amplified using an OPAMP: the sample-and-hold capacitors C_3 connected to its outputs are conveniently used as the dominant pole of the feedback AGC loop, which has a GBWP of 229 MHz and a DC-loop gain of 49 dB (at maximum datapath gain).

Depending on the initial value of i_{FFx} set during the feedforward phase and the differential setpoint current I_{REF}, the datapath gain will now be either increased or decreased. When the loop-gain is sufficiently large, v_{E} acts as a nullator node, and $i_{\mathrm{AGC}}^{\mathrm{avg}} \approx I_{\mathrm{REF}}$: the relationship in Fig. 4.13 can then simply be inverted to evaluate the output swing as a function of the configured reference current I_{REF}. This is shown in Fig. 4.14.

The analysis above only holds when the emitter resistances have been neglected. As a result, the theoretical model significantly differs from the simulated trace shown in Fig. 4.14, in particular for larger input swings. Just as in the case of simple emitter-degenerated

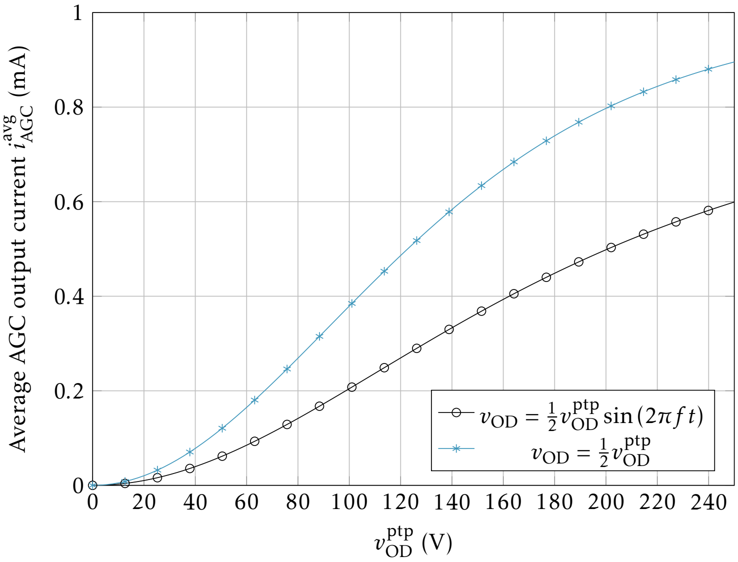

Figure 4.13: Theoretically derived average AGC output current $i_{\mathrm{AGC}}^{\mathrm{avg}}$ versus peak-to-peak input voltage $v_{\mathrm{OD}}^{\mathrm{ptp}}$.

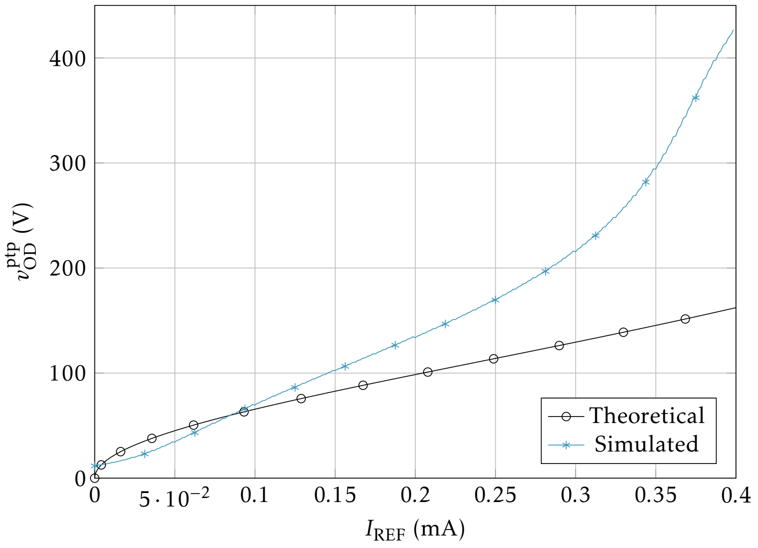

Figure 4.14: Theoretical and simulated output swing $v_{\mathrm{OD}}^{\mathrm{ptp}}$ as a function of the configured AGC-current I_{REF}.

BJT differential pairs, a closed-form expression of Eq. (4.15) cannot be established [4]. As a result, the theoretical model significantly differs from the simulation at larger input swings $v_{\mathrm{OD}}^{\mathrm{ptp}}$. Luckily, this compression of the measurement range benefits us as a larger range of output swings can now be configured. Although the resulting transfer function is now significantly non-linear, this only impacts the actual output swing versus the configured one (and can easily be corrected through software).

A third trace in Fig. 4.11 shows the output swing as a function of the average input photocurrent $i_{\mathrm{PD}}^{\mathrm{avg}}$ with feedback enabled, illustrating how the use of the presented feedback AGC (combined with the already settled feedforward AGC) reduces the output dynamic range to only $< 0.7\,\mathrm{dB}$ (for an input dynamic range of 24 dB).

Post-Amplifier Datapath

The feedforward- and feedback gain control systems are used to set the gain in the post-amplifier datapath, both through continuous gain control in the VGAs (using i_{CTLx}), as well as an additional switchable gain in the S2D converter. An output driver is then used to drive an external 50 Ω load.

Fig. 4.15 shows the implementation of the S2D converter: a large tail current is used for linearity, while no gain is provided. A 6 dB attenuation is obtained by reducing the load resistance through a PMOS-transistor M_1 operating in triode: Doing so slightly increases the 3 dB-bandwidth from 23.2 GHz to 26.4 GHz while keeping peaking below 0.5 dB.
The VGAs are implemented using the circuit shown in Fig. 4.16: the circuit consists of a Gilbert-cell (in which the gain is altered by controlling the cascode voltages of transistors $Q_{1\mathrm{x}}$), followed by a pair of emitter followers.

Neglecting emitter resistances, the output voltage can be written as:

$$v_{\mathrm{OD}} = I_{\mathrm{TAIL}} \tanh\left(\frac{v_{\mathrm{ID}}}{2U_T}\right) \tanh\left(\frac{v_{\mathrm{CTL}}}{2U_T}\right) \tag{4.16}$$

Through emitter degeneration of the bottom pair transistors (R_{Ea},R_{Eb}), the input range and linearity are increased to support PAM-4 operation. The control voltage $v_{\mathrm{CTL}} \triangleq v_{\mathrm{CTLP}} - v_{\mathrm{CTLM}}$ is typically generated

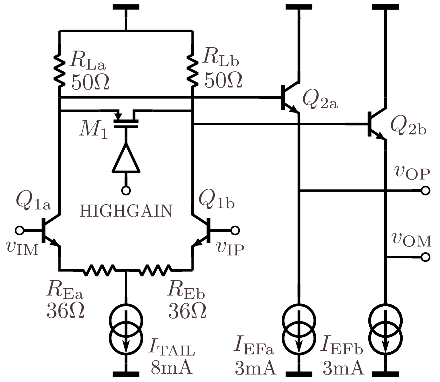

Figure 4.15: S2D converter implementation.

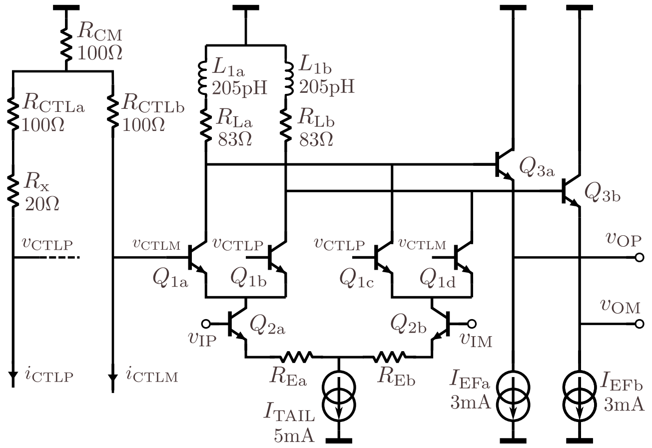

Figure 4.16: Variable gain amplifier used in the datapath.

using a predistortion element such as a diode to compensate for the hyperbolic tangent transfer characteristic [4]. This linearization of the gain versus drive current improves the accuracy of the feedforward AGC. However, with the addition of a feedback AGC, these were later replaced by resistors $R_{\text{CTLa}} = R_{\text{CTLb}} \triangleq R_{\text{CTL}}$, as they could be sized to provide a higher gain. Although this reduces the gain-linearity of the VGA, the presence of the feedback AGC mitigates the imperfections in the feedforward gain control precision.

Notice that it is possible to invert the phase of the output by changing the sign of the drive current. This can lead to positive feedback when used in combination with the feedback AGC and AOC loops. Although the sign inversions cancel with two cascaded VGAs driven with the same control signals, having a datapath with near-zero gains and mismatch between the two VGAs is still a dangerous situation. In conjunction with Monte-Carlo simulations, a small resistor R_x was added in series to ensure that this sign-changing does not occur.

Fig. 4.17 shows the simulated frequency response of the gain for different control currents i_{CTL}. Notice that the bandwidth slightly drops for lower gains, which is caused by the additional parasitic capacitance at the output load due to the activation of the anti-parallel branch Q_{1a} and Q_{1d}. Fig. 4.18 shows the THD for a single VGA stage, showing < 5% THD for input swings up to around 340 mV. The inductors L_{1a} and L_{1b} were added to enhance the bandwidth, at the cost of an additional group delay variation of 12 ps. In faster technologies these would not be necessary, which would prove beneficial, in particular for multilevel modulation formats such as PAM-4.

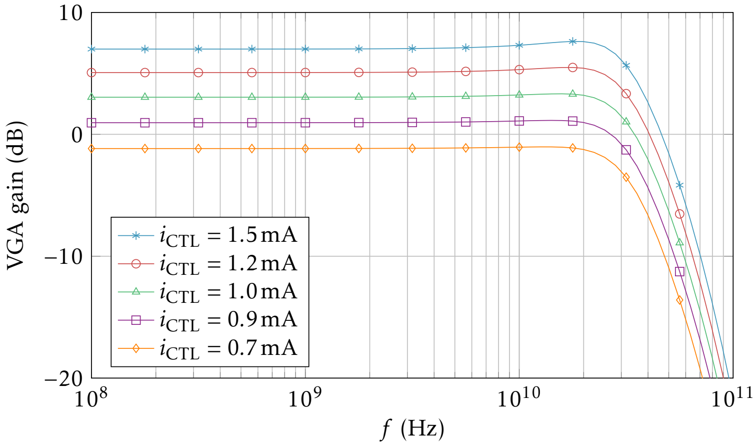

Figure 4.17: Simulated frequency response of a single VGA stage, configured for all practical values of the input dynamic range. The 3 dB-bandwidth varies from 36.2 GHz at the highest gain to 33.3 GHz at the lowest gain.

The output driver is implemented as a differential pair similar to the one used in Fig. 4.15 and provides a final fixed gain of 1.6 dB while

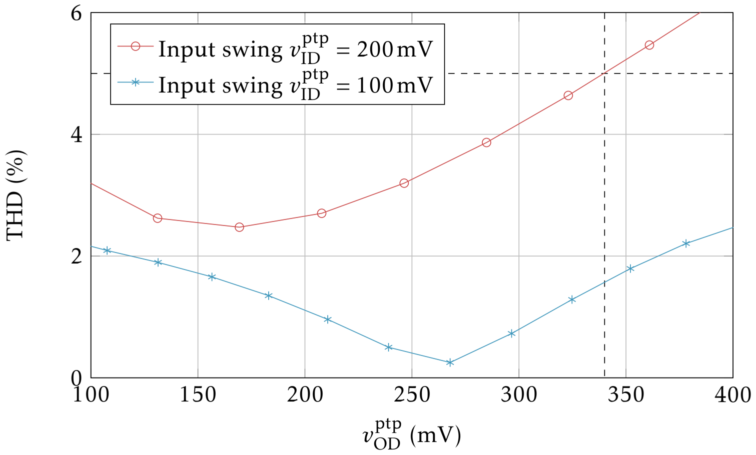

Figure 4.18: Simulated THD of a single VGA stage as a function of the peak-to-peak output swing (with an applied input swing v_{ID} of 100 mV and 200 mV).

capable of providing at least 250 mV of output swing.

Sweeping the input photocurrent swing $i_{\mathrm{PD}}^{\mathrm{ptp}}$ while using the AGC to maintain a 250 mV swing leads to a total datapath THD curve as shown in Fig. 4.19. The simulations were performed twice: with and without attenuation in in the S2D converter. Notice that for linearity, the gain needs to be reduced at around 700 µA peak-to-peak (or 350 µA average) photocurrent, which coincides with the threshold chosen and shown in Fig. 4.11: this brings the $< 5\%$ THD range to 1.3 mA peak-to-peak photocurrent. As already discussed, this is to avoid overloading the VGAs and to maintain linearity.

Balancing the Output Signal

The balancing loop shown in Fig. 4.21 corrects errors caused by the static error of the input offset current loop in the TIA (causing a difference between V_{REF} and the average of v_{TIA}) and the mismatch in the post-amplifiers. Just as in the case of the AGC feedback loop, the dominant pole at the output of the OPAMP OA_4 consists of the charge capacitors C_4 which are switched off using S_4 to retain the state of the loop after settling.

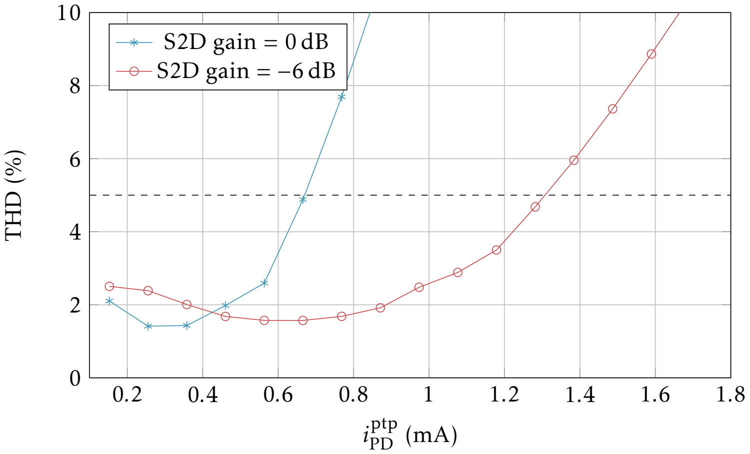

Figure 4.19: Simulated THD of the full datapath as a function of the peak-to-peak input current $i_{\mathrm{PD}}^{\mathrm{ptp}}$ with the AGC fixing the output swing to 250 mV.

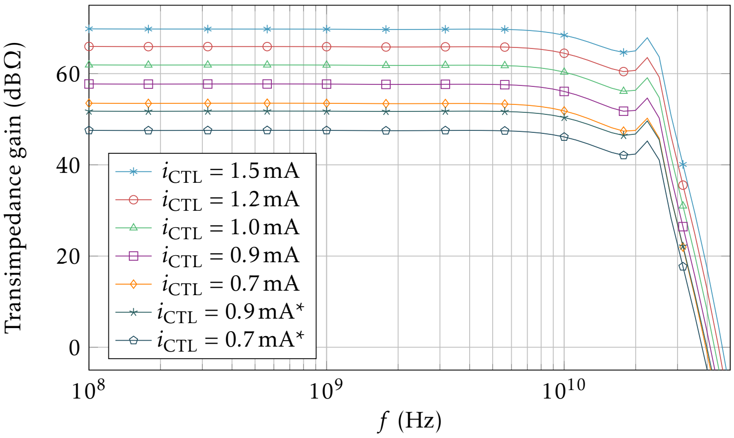

Figure 4.20: Simulated frequency response of the total transimpedance Z_t used for all practical values of the input dynamic range. (*)-lines have the S2D gain set to −6 dB instead of 0 dB. The 3 dB-bandwidth varies from 26.9 GHz to 24.8 GHz.

The offset voltage in series with V_{REF} is generated by introducing a voltage drop over a resistor R_{OS} as shown in the shaded area of Fig. 4.21: any non-zero correction voltage $v_{\mathrm{BAL}} \triangleq v_{\mathrm{BALP}} - v_{\mathrm{BALM}}$ causes

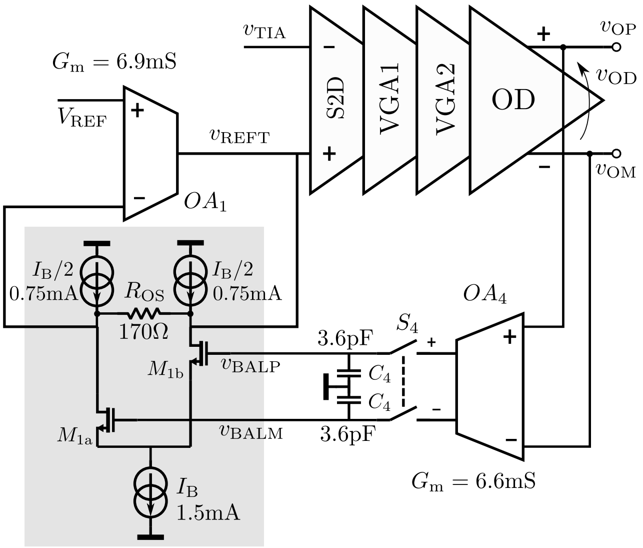

Figure 4.21: Balancing loop of the output signal.

a current of $\frac{g_{m1} v_{BALD}}{2}$ to flow through R_{OS} (with g_{m1} the transconductance of M_1). Neglecting the input offset voltage of the follower OPAMP OA_1 and mismatch in the bias currents, the reference voltage at the input of the S2D amplifier can be written as:

$$v_{REFT} = V_{REF} - R_{OS} \frac{g_{m1} v_{BAL}}{2} \tag{4.17}$$

An average $v_{OD} > 0$ will cause v_{BAL} to rise, which causes v_{REFT} to lower. This in tern reduces v_{OD} again, effectively zeroing the DC output offset voltage. The feedback loop operates with a simulated GBWP of 544 MHz and DC-loop gain of 80.3 dB at the highest datapath gain. Notice that from the burst-mode operation, the worst-case settling time occurs during the highest input burst power, at which the datapath gain has been reduced by the AGC.

SOB Detection

As shown in Fig. 3.1, the SOB is detected by comparing the square root of the estimated average photocurrent i_{PDMON1} to a configurable reference current. In this design, a simple current comparator (shown in Fig. 4.22b) is used.

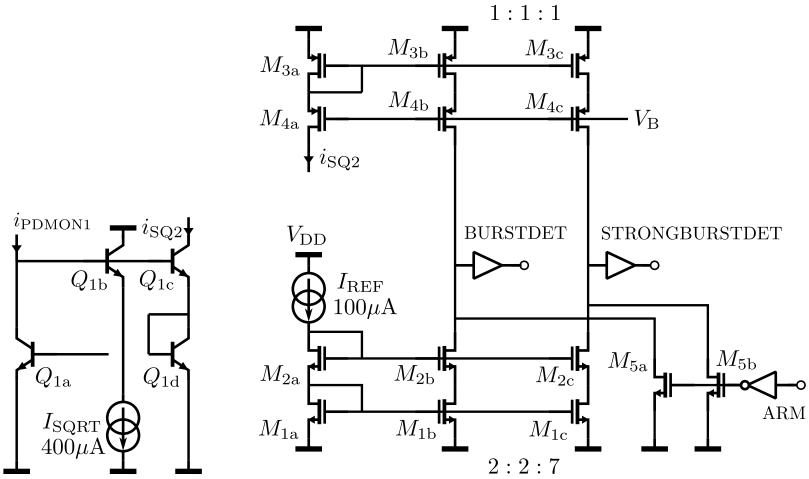

(a) $\sqrt{x}$ circuit.

(b) Burst current detector.

Figure 4.22: Burst current detection using square root of average photocurrent.

The $\sqrt{x}$ translinear circuit from Fig. 4.9 is reused as a compressing current amplifier to increase the input range. With the comparison reference set to $I_{\mathrm{REF1}} = I_{\mathrm{REF}} = 100\,\mu\mathrm{A}$ (and $I_{\mathrm{SQRT}} = 400\,\mu\mathrm{A}$), the theoretical SOB threshold can be calculated from Eq. (4.10):

$$i_{\mathrm{PD,th}}^{\mathrm{avg}} = I_{\mathrm{REF1}}^2 / I_{\mathrm{SQRT}} = 25\,\mu\mathrm{A} \tag{4.18}$$

Which corresponds to around −13 dBm of optical input power at 0.5 A/W photodiode responsivity. A second reference level is used to distinguish between weak and strong bursts to switch the gain in the S2D amplifier, as mentioned before. This level has been set to $I_{\mathrm{REF2}} = \frac{7}{2} I_{\mathrm{REF}} = 350\,\mu\mathrm{A}$ (and $I_{\mathrm{SQRT}} = 400\,\mu\mathrm{A}$). Again, the corresponding photocurrent threshold can be calculated:

$$i_{\mathrm{PD,th2}}^{\mathrm{avg}} = I_{\mathrm{REF2}}^2 / I_{\mathrm{SQRT}} = 306\,\mu\mathrm{A} \tag{4.19}$$

This level corresponds to −2.1 dBm of optical input power at 0.5 A/W photodiode responsivity. To avoid noise penalties due to the lowered S2D gain, it is best to only reduce the gain to maintain linearity and to reduce overload in the VGAs, so switching should only occur at higher input power levels.

The speed at which the SOB detector asserts is dependent on the relative difference between the input current i_{PDMON1} and the reference current I_{REFx}. A larger difference will charge the internal parasitic nodes faster, causing a faster toggling of the logic gates following the detector. Fig. 4.23 shows the simulated response time of the SOB detector (for the two reference levels I_{REF1} and I_{REF2}) as a function of the average input photocurrent i_{PD}, converted through the square-root translinear circuits.

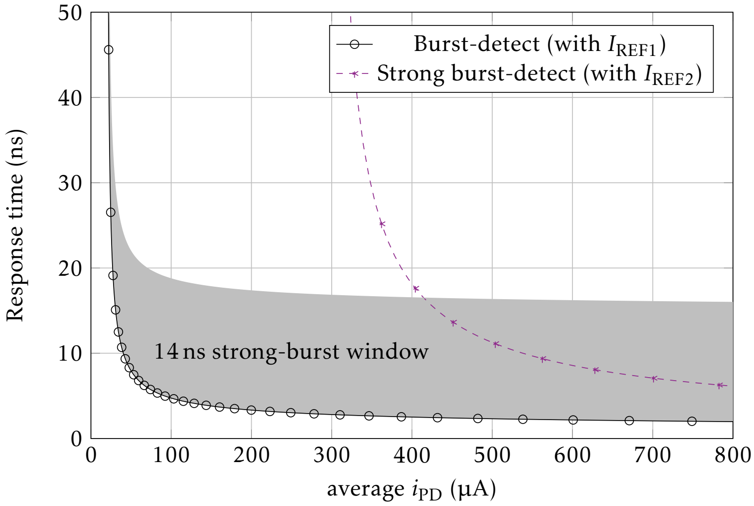

Figure 4.23: Response time of the SOB detector as a function of the average input photocurrent i_{PD}.

For input currents very close to the reference levels, the detection time can be unacceptably long. When this happens, the burst sequencer is initiated too late, and the receiver will not have properly set its AOC and AGC because the preamble has already ended. For the detection of strong bursts, this situation can be avoided by allowing a maximum detection time, starting from the moment a burst has been detected by the first reference level. Asserts occurring beyond this window are then simply ignored. In this design, this window is programmable between 6 ns and 14 ns (starting from the SOB assertion); for the maximum time configuration, the corresponding window is shaded in gray in Fig. 4.23.

Notice that this time-constrained assertion requires a higher photocurrent than what was calculated in Eq. (4.19), which must be accounted for when choosing a proper reference level I_{REF2}.

The fundamental trade-off between the response time and the burst-detect sensitivity level can negatively impact the performance of the LBMRX. Pre-amplifying the current in a square-root translinear circuit can help to increase the SOB detector sensitivity, but noise spikes in the photocurrent can still cause false positives. For this reason, the SOB can be alternatively provided externally through the CML interface.

At the end of a burst, charge remains present on the internal comparison nodes in Fig. 4.24. To quickly reset the SOB detector, transistors $M_{5\mathrm{a}}$ and $M_{5\mathrm{b}}$ are added in parallel to quickly discharge these nodes upon EOB detection, to prepare the receiver for the next burst.

EOB Detection

Because the gain- and offset loops have already been configured during the preamble, the differential output signal $v_{\mathrm{OP}}-v_{\mathrm{OM}}$ (in Fig. 4.1) can be used to trigger the EOB detector. This allows for a rapid detection of the EOB (especially at weaker input power levels) which reduces the minimum needed guard time between bursts.

The EOB detection circuit shown in Fig. 4.24 triggers if $v_{\mathrm{OM}} > v_{\mathrm{OP}}$ for a predetermined amount of time. First, the input voltage is converted into a current $i_{\mathrm{EOB}} \approx \frac{v_{\mathrm{OP}}-v_{\mathrm{OM}}}{2R_E}$ using a degenerated differential input pair Q_1 - R_E as transconductor. A current DAC is added in parallel to compare the generated current to a configurable threshold current. The current difference is then converted into a voltage using an invertor-based shunt-feedback TIA:

$$v_{\mathrm{T}} \approx V_{GS1} - R_{\mathrm{F}}\left(\frac{I_{\mathrm{B1}}}{2} - I_{\mathrm{DAC}} - \frac{v_{\mathrm{OP}} - v_{\mathrm{OM}}}{2R_E}\right) \tag{4.20}$$

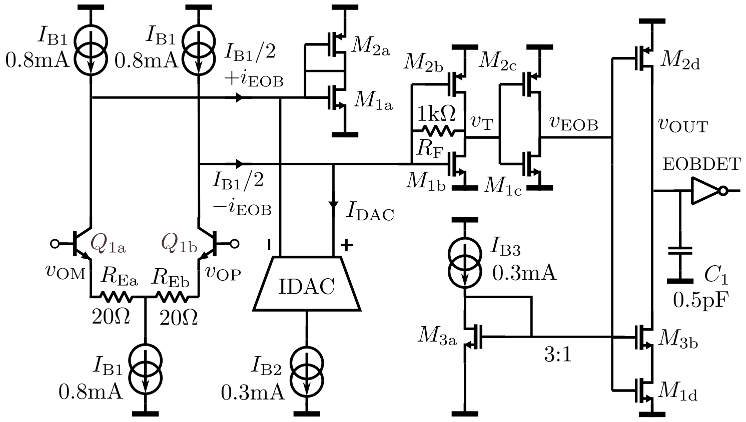

Figure 4.24: EOB detection circuit.

Having $v_{OP} < v_{OM}$ decreases v_T, which causes v_{EOB} to go high and v_{OUT} to go low, as illustrated in Fig. 4.25. Notice that the downward slope of v_{OUT} after the burst is deliberately slewed by using a current starved sink element (M_3 and C_1). This causes an EOB to be only signaled if $v_{OP} < v_{OM}$ for a sufficiently long time. On the other hand, when $v_{OP} > v_{OM}$ for only a brief moment (e.g. a logic high after a series of logic zeros), C_1 recharges very quickly.

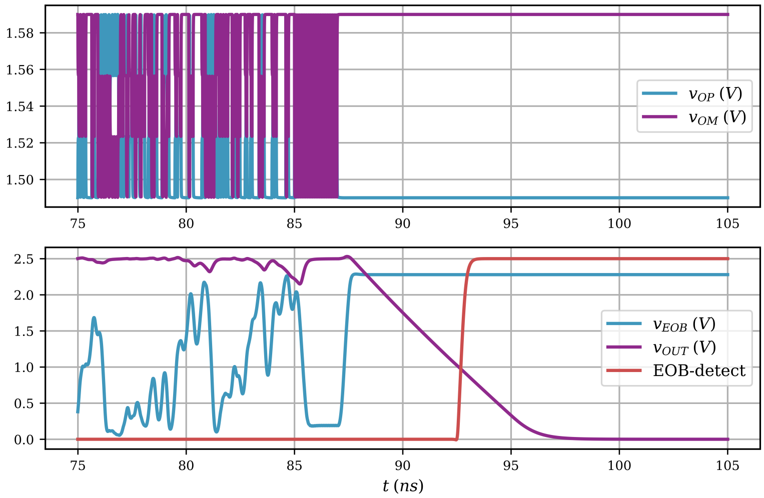

Figure 4.25: Transient simulation of the EOB-detector, showing an EOB-detection after 5 ns of inactivity.

4.2 Experimental Results

To evaluate the receiver performance, the developed chip is wire-bonded together with a PIN-photodiode (with a nominal responsivity 0.5 A/W) on an PCB assembly, as shown in Fig. 4.27. A micrograph of the receiver core can be seen in Fig. 4.28. Through optical probing, the assembly is then characterized using the setup shown in Fig. 4.26.

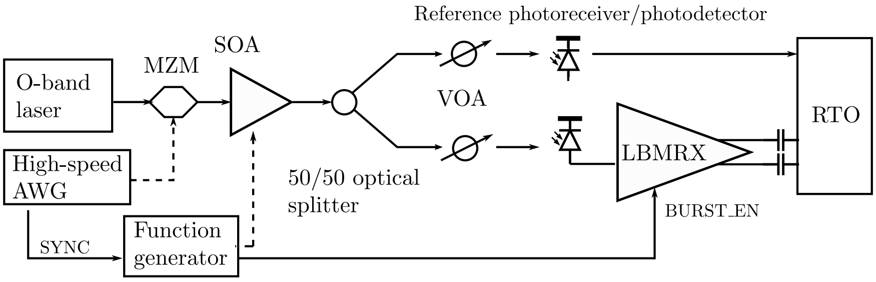

Figure 4.26: Experimental setup used to test the LBMRX. Burst data AWG: Keysight M8195A, O-band laser source: Tunics T100S-HP, SOA: Inphenix IPSAD1301, Envelope AWG: Tektronix AFG3102, MZM: MX-1300-40-LN, VOA: Keysight N7762A, Reference photodiode: Finisar XPDV21x0RA, Photodiode = Albis PD40, RTO = Lecroy LabMaster 10-36Zi-A / Keysight DSA-Z 634A.

In the high-speed AWG, a (burst-mode) $2^{15} - 1$ PRBS sequence data stream is generated which is Gray-mapped onto NRZ or PAM-4 transmit pulses. The MZM is then driven by this signal, which modulates a data pattern into the 1310 nm laser beam emitted from the continuous-wave (CW) laser source. The different burst packets are then carved into this signal by using a SOA driven by a function generator. Isolators were added to prevent reflections from disturbing the SOA operation, which is especially critical at the output side of the SOA. The outputs of the LBMRX are captured by a RTO, which allows offline computation of the resulting BER (without using any kind of equalization). A reference photodiode is used to measure the extinction ratio of the transmitter and to compare eye diagrams. In these measurement, the eye diagrams and their extinction ratios are shown in Fig. 4.29.

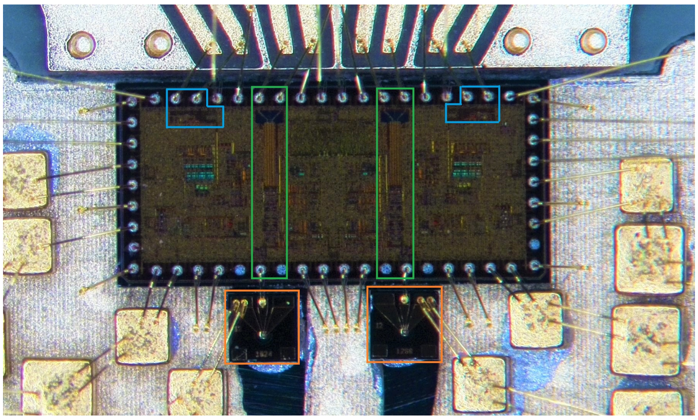

Figure 4.27: Wirebonded PCB-assembly. Green: datapath. Blue: CML-interface. Albis photodetectors are shown in orange. 2 channels are implemented on a die with dimensions 3.05mm × 1.4mm.

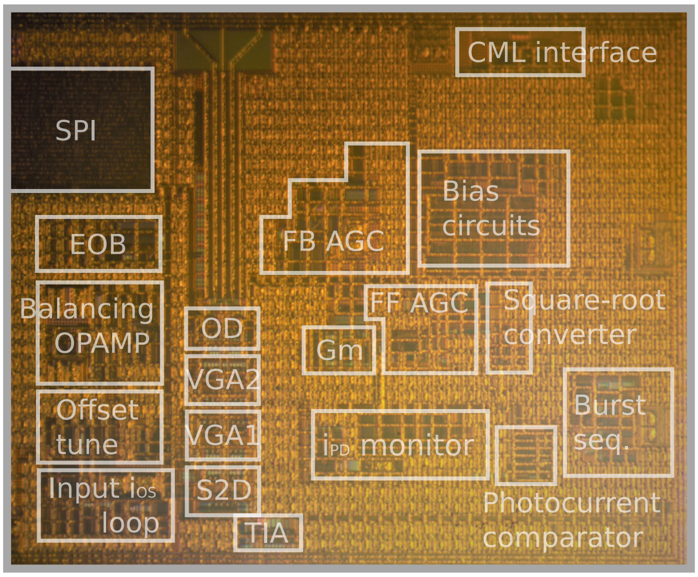

Figure 4.28: Receiver core micrograph.

Continuous-Mode Operation

First, the LBMRX is configured in continuous-mode with different fixed transimpedance gains by providing fixed control currents i_{CTLx} for the VGAs. The BER is then measured as a function of the re-

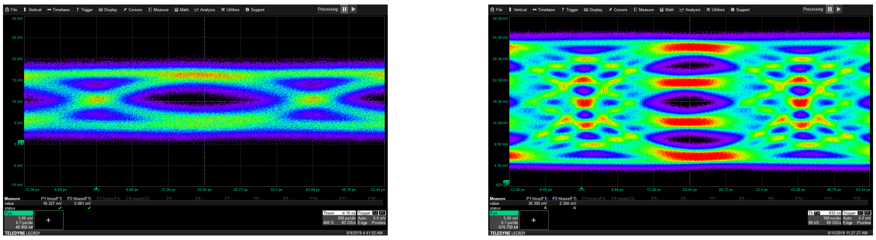

(a) 25 Gbit/s NRZ reference at 0 dBm. Measured extinction ratio = 5.1 dB

(b) 50 Gbit/s PAM-4 reference at 3 dBm. Measured extinction ratio = 5.9 dB

Figure 4.29: Reference eye diagrams.

ceived optical power. The results are shown in Fig. 4.30 for 25 Gbit/s NRZ and 50 Gbit/s PAM-4.

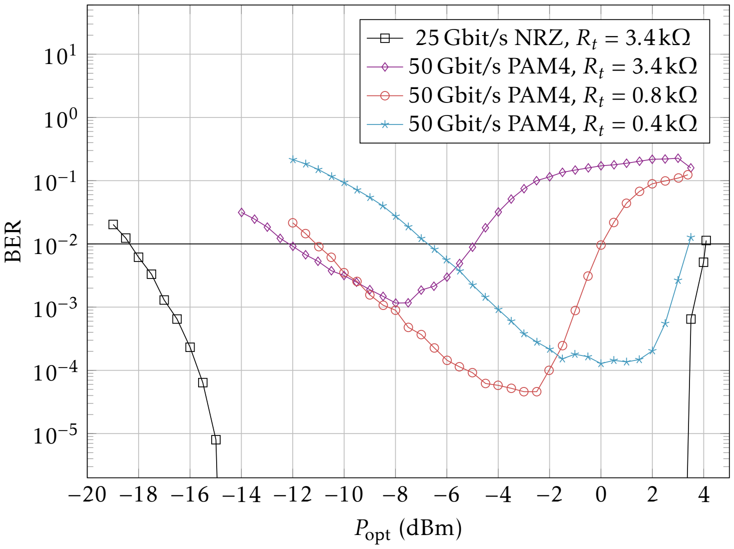

Figure 4.30: BER for NRZ and PAM-4 as a function of received optical input power in continuous-mode, for different fixed gain settings in the datapath.

A reference BER-level of 1×10^{-2} is chosen with LDPC (17% overhead) in mind (see Table 2.4), according to upcoming 25 Gbit/s and 50 Gbit/s PON-standards [5, 6]. With the highest achievable gain, a sensitivity level of −18.3 dBm for NRZ and −12.1 dBm for PAM-4 is observed. The differential RMS output noise voltage is measured as 3.8 mV, which corresponds to an equivalent 1.1 μA of input-referred RMS noise current.

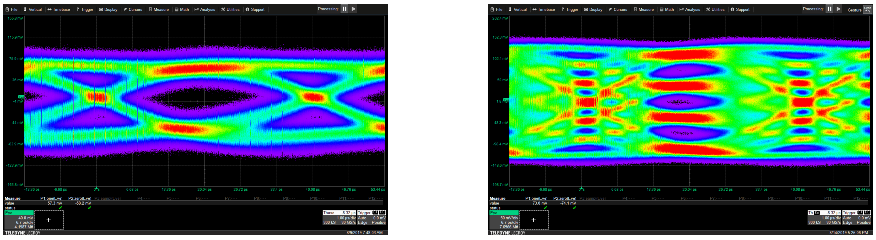

(a) 25 Gbit/s NRZ eye diagram at −12 dBm.

(b) 50 Gbit/s PAM-4 eye diagram at −4 dBm.

Figure 4.31: LBMRX continuous-mode eye diagrams.

Fig. 4.32 shows the measured frequency response of the LBMRX for the same gain settings as in Fig. 4.20. To obtain these curves, the RTO from Fig. 4.26 is replaced with a vector network analyzer (VNA). The transmitter frequency response was de-embedded by using a 70 GHz, 50 Ω terminated PIN-photodiode. Compared to the simulations, significant peaking can be observed. This is due to a larger-than-expected input bondwire inductance. Looking at the relevant wirebonding shown in Fig. 4.27 this is to be expected, because the photodiode cathode bias was designed to be provided through an on-chip connection (resulting in lower bondwire inductance) instead of the externally provided one.

Photocurrent Monitor Verification

Before evaluating the burst-mode performance of the receiver, the different control circuits are examined and optimized. First, the photocurrent monitor from Section 4.1 is characterized by applying a known optical power level and measuring the replicated photocurrent, as well as the actual photocurrent into the cathode of the PIN-photodiode. As can be seen from Fig. 4.33, the relative error can be reduced by choosing an appropriate I_{CAL}, which is needed for proper triggering of the SOB detector, as well as providing a precise

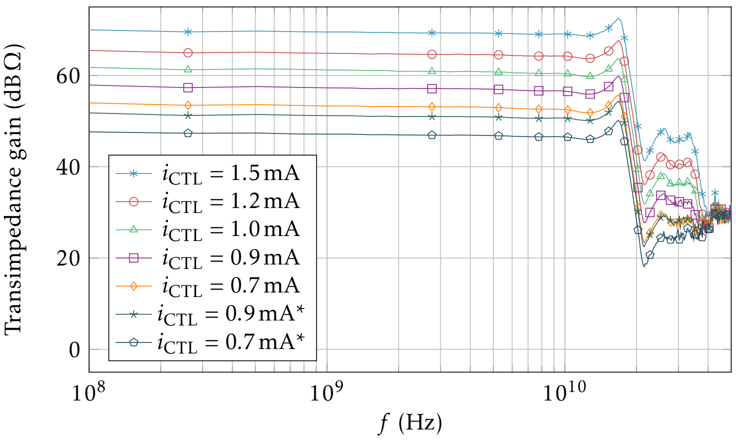

Figure 4.32: Measured frequency response of the total transimpedance Z_t used for all practical values of the input dynamic range. (*)-lines have the S2D gain set to −6 dB instead of 0 dB. The 3 dB-bandwidth varies from 18.3 GHz to 17.9 GHz.

feedforward gain correction. Compared to Fig. 4.8, a slightly higher I_{CAL} is required for optimal accuracy (176 µA instead of 152 µA).

Feedforward and Feedback Gain-Control Verification

To visualize the impact of the feedforward and feedback gain-control loops, a series of bursts with gradually increasing power levels and containing only 1010..-preamble data is generated in the experimental setup, as shown in Fig. 4.34. This shows that the needed corrections made by the AGC are quite small, as the output dynamic range is only 3.8 dB when the feedback AGC is replaced with a fixed (although optimized) value. When the feedback is added, this is further reduced to only 1.3 dB. Through extensive AGC-tunability options, the output swing can be increased, at the cost of a higher output dynamic range.

Start- and End-of-Burst Detector Verification

For the next set of experiments, the AWG is configured to generate burst-mode data, consisting of a sufficiently long 500 ns preamble, followed by a 2.5 µs / 125 µs payload containing NRZ or PAM-

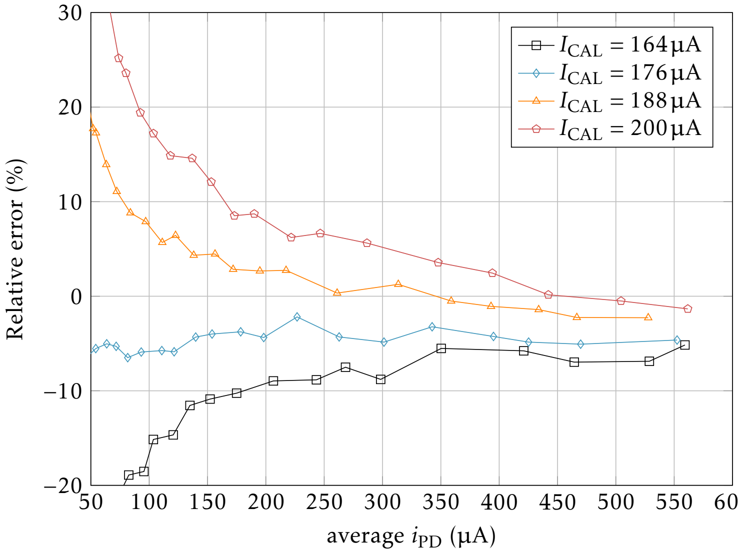

Figure 4.33: Relative error of the measured photocurrent estimate i_{PDMON2} versus the average of the photocurrent i_{PD} for different I_{CAL} settings.

4 data. The SOA is driven to control the power of the individual bursts. Fig. 4.36 shows how the SOB and EOB (red) assert low upon arrival of a burst or right after the burst has ended, respectively. [1]

Through the CML interface, these can be used for the MAC layer to facilitate interfacing or to characterize the response time of the SOB detector, as is done in Fig. 4.37. Here, the response time is measured as a function of the applied burst power: for powers below −10 dBm (theoretically predicted as −13 dBm using Eq. (4.18)), the SOB detection time grows exponentially large, causing the SOB detector to fail detection.

After the SOB has been detected, a maximum time of $\Delta T_1 + \Delta T_2 =$ 62.7 ns (see Fig. 4.2) is allocated for settling of the AGC and AOC loops. Here, ΔT_1 and ΔT_2 are configured as 11.6 ns and 51.1 ns, respectively. Allowing 20 ns for the SOB detection, this brings the total settling time to 82.7 ns. Finally, the EOB detector operates on

---

[1] Note that these figures are taken from a different experiment, in which the preamble length was 2 µs instead of 2.5 µs.

Figure 4.34: Top left: i_{PD} as measured with reference photodetector, and internally generated SOB signal (measured through v_{CMLM}). Bottom left: v_{OD} with the LBMRX operating in burst mode, but with fixed gain. Top right: feedforward AGC only. Bottom right: feedforward + feedback AGC.

the differential output signal: with AGC active and set to an output swing of 200 mV, the detector response time is measured to be 9.1 ns in the fastest setting.

25Gbit/s NRZ Burst-Mode Operation

With the burst-mode control circuits properly configured, the complete burst-mode receiver performanceis examined. For this purpose, two bursts are created in rapid succession of one another, with 50 ns of guard time. In one case, the burst powers are swept but kept equal to each other (loud-loud situation). In another case, the power of the first burst is fixed to 3 dBm and the second burst power varied (loud-soft situation). The power of these bursts is individually varied with the SOA. Fig. 4.38 shows the resulting waveforms as seen at the output of the LBMRX and the reference photodiode, for the loud-soft situation with two different follow-up burst power levels.

Fig. 4.39 shows the resulting eye diagrams and the BER of the 2.5 µs NRZ payload in the second burst as a function of its power. To verify the sensitivity beyond the −10 dBm SOB threshold, an external SOB

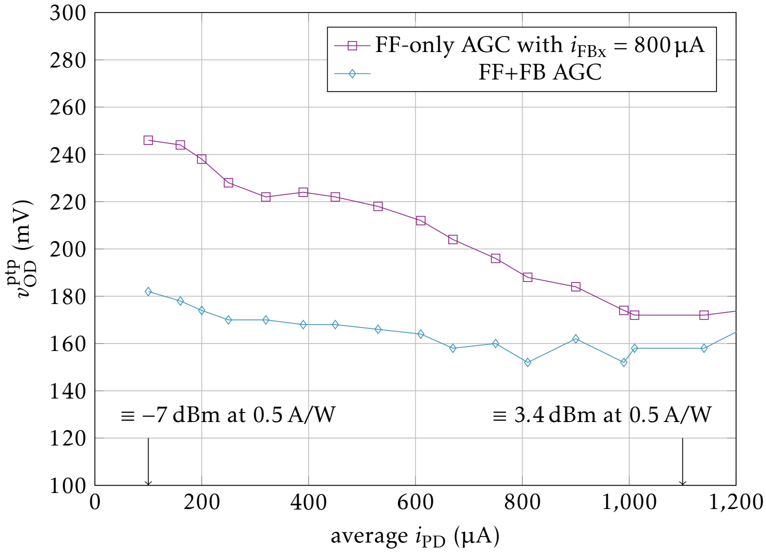

Figure 4.35: Measured characteristics of the feedforward and feedback AGC loops as a function of the average of the photocurrent i_{PD} (each point corresponds to a burst level in Fig. 4.34).

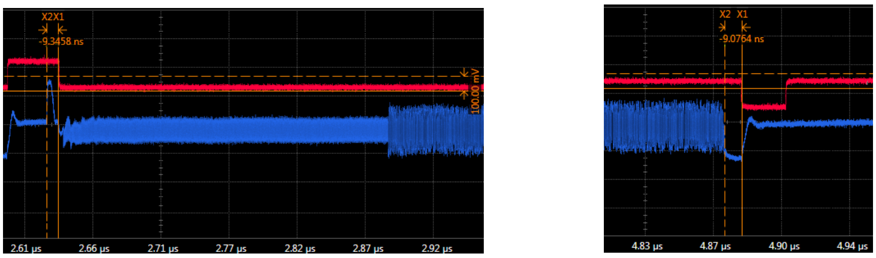

(a) SOB detection

(b) EOB detection

Figure 4.36: SOB and EOB detection (red), as measured through v_{CMLM} (Burst power ≈ −3 dBm). Blue: single-ended datapath output showing the actual burst signal.

signal is provided through the CML interface.

The BER stays below the 1×10^{-2} limit from −18.1 dBm up to at least 3.5 dBm with a loud-soft sensitivity penalty of 0.9 dB. Compared to continuous-mode (CM) operation (Fig. 4.30), a negligible penalty of

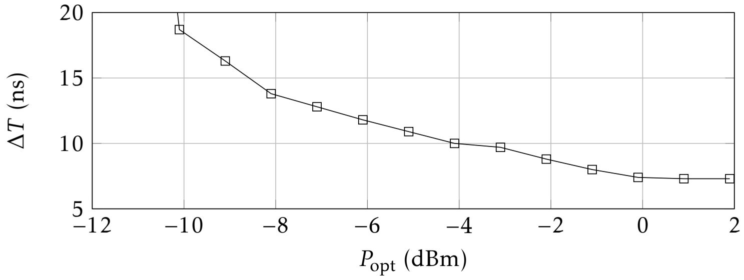

Figure 4.37: SOB response time as a function of the optical received power.

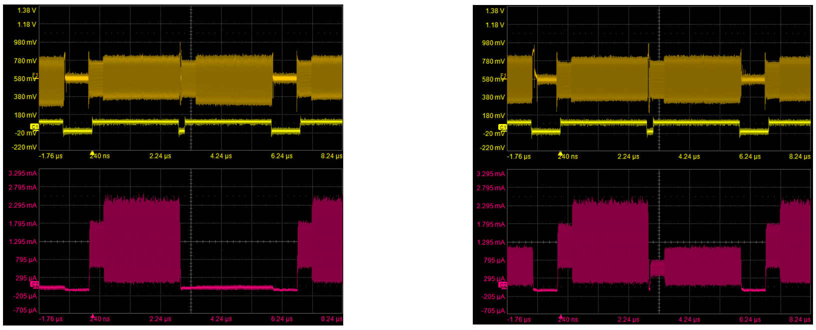

(a) Burst 2 power: −10 dBm.

(b) Burst 2 power: 0 dBm.

Figure 4.38: Captured burst-mode waveform at as seen through the LBMRX output (top) and the reference photodiode (bottom).

0.1 dB is observed. In addition, the output dynamic range is reduced to 1.4 dB over the specified −10 dBm → 3.5 dBm range (verifying the results shown in Fig. 4.35).

When using the internally generated SOB, the results are nearly identical up until around −12 dBm, at which point the receiver starts to occasionally fail detecting the burst within the 500 ns preamble. As a result, the balancing loop retains it state, typically leading to a unusable output signal in a loud-soft burst sequence.

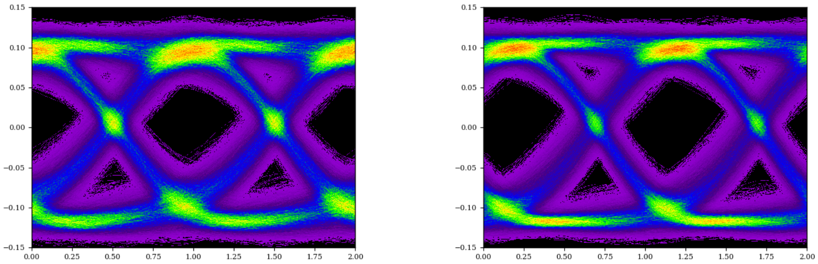

(a) Eye diagram at −10 dBm.

(b) Eye diagram at 0 dBm.

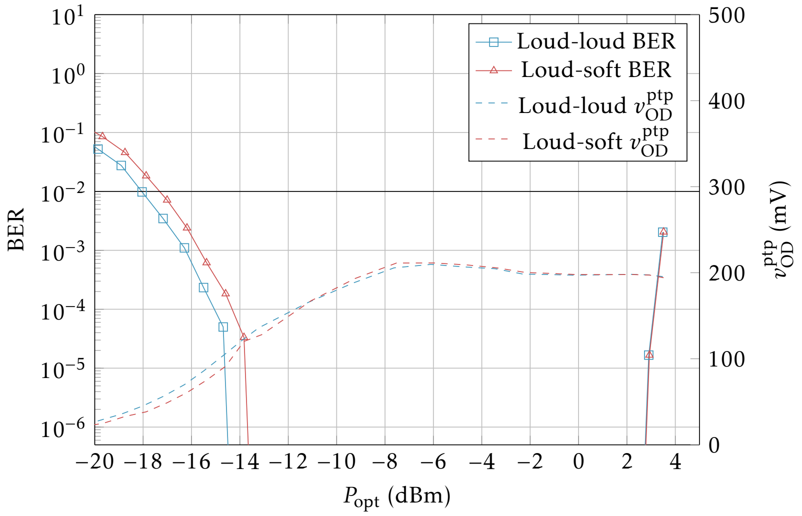

Figure 4.39: 25 Gbit/s NRZ eye diagrams and BER in the second burst payload (AGC configured to 200 mV output swing).

Long-Burst Verification

Because several sample-and-hold capacitors are used across the design, the impact of charge leakage could potentially severely impact the performance, in particular for longer bursts. Fig. 4.40 shows the impact of the payload duration on the BER of the second burst in a loud-soft burst sequence. This shows that the receiver still operates nominally for burst payload durations up until 125 µs: the worst-case observed sensitivity penalty here is 1.5 dB. Note that the resulting penalty is mostly due to AC-coupling effects when the residual

DC output offset is not completely zeroed at the start of each burst.

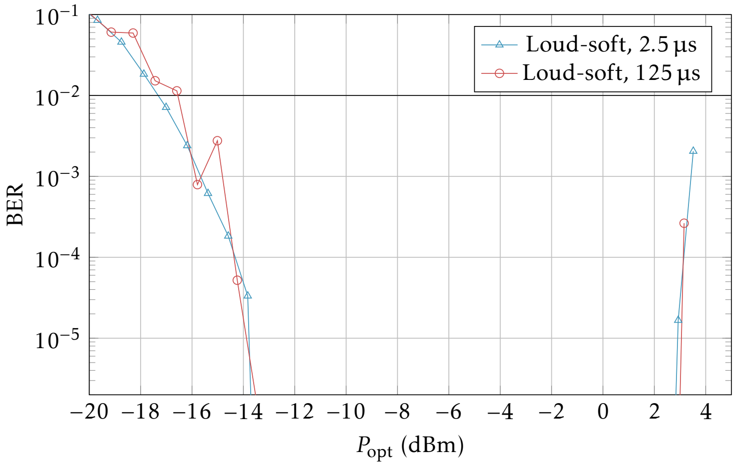

Figure 4.40: Impact of long burst payload durations on the BER performance in a loud-soft burst sequence.

50Gbit/s PAM-4 Burst-Mode Operation

In a final experiment, the linearity of the LBMRX is investigated by replacing the NRZ payload by a PAM-4 payload. As the expected receiver sensitivity is now near the SOB detector sensitivity, the internal SOB detector is used instead. Fig. 4.41 shows the eye diagrams and BER of a 1.5 µs PAM-4 payload in the second burst as a function of its power. The power of the first burst in the loud-soft case is 4.3 dBm.

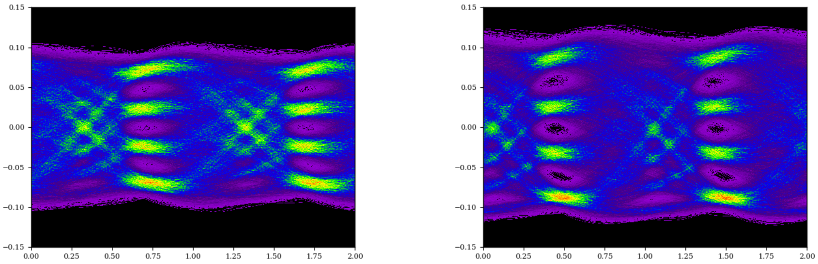

(a) Eye diagram at −10 dBm.

(b) Eye diagram at 0 dBm.

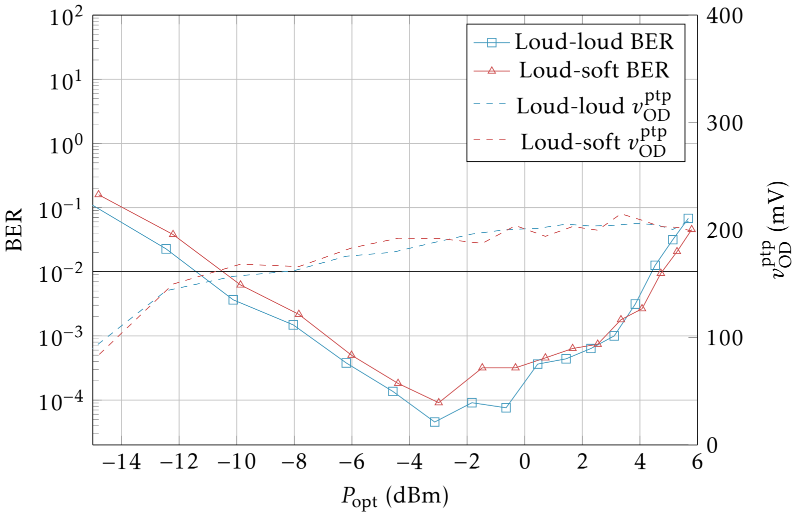

Figure 4.41: 50 Gbit/s PAM-4 eye diagrams and BER in the second burst payload (AGC configured to 200 mV output swing).

The BER stays below the 1×10^{-2} limit from −11.4 dBm up to 4.4 dBm with a loud-soft sensitivity penalty of 0.9 dB. Compared to CM operation (Fig. 4.30), a penalty of 0.7 dB (using the highest gain) is observed. In addition, the output dynamic range is reduced to 2.0 dB over the specified −10 dBm → 4.4 dBm range.

4.3 Conclusion

This chapter demonstrated a 50 Gbit/s PAM-4-linear LBMRX with a sensitivity level of −18.1 dBm for NRZ and −11.4 dBm for PAM-4, and an input dynamic range of 21.6 dB for NRZ and 15.8 dB for PAM-4. By using the analog burst-mode AGC circuits, the output dynamic range was reduced to 1.4 dB for NRZ and 2.0 dB for PAM-4. The AGC/AOC loops are allowed a (configurable) maximum settling time of 82.7 ns (20 ns for burst detection, followed by 62.7 ns for loop settling), at which point they are fixed using sample-and-hold capacitors. The reconfiguration time is compatible with upcoming standards, and power consumption is sufficiently small for integration into industry standard transceiver modules. Finally, since the BMRX is linear, it is suitable for reception of e.g. PAM-4.

References

[1] E. Säckinger, *Broadband Circuits for Optical Fiber Communication*. Wiley, 2005.

[2] E. Sackinger, *Analysis and Design of Transimpedance Amplifiers for Optical Receivers*. Wiley, 2017.

[3] *40-Gigabit-capable passive optical networks (NG-PON2): Definitions, abbreviations and acronyms*, ITUT-T Recommendation G.989, 2015.

[4] P. Gray, *Analysis and Design of Analog Integrated Circuits, 5th Edition*. Wiley Global Education, 2009.

[5] IEEE P802.3ca 50G-EPON Task Force, "Physical Layer Specifications and Management Parameters for 25Gb/s and 50Gb/s Passive Optical Networks." [Online]. Available: http://www.ieee802.org/3/ca/

[6] V. H. Dora van Veen, "FEC code for 25/50/100G EPON (IEEE P802.3ca 100G-EPON Task Force Meeting)," 2017.

5

Requirements for Adaptive Burst-Mode Equalization in >25Gbit/s PON Applications

In anticipation of emerging applications such as business services, 5G and Internet of Things (IoT), research and standardization have been working together towards next-generation 25/50Gbit/s passive optical networks. In this endeavor, two burst-mode front-end OLT receivers have been developed in the previous chapters. Both receivers are linear and are capable of handling up to 25 Gbaud data rates through direct detection.

However, several other components are required for the realization of upstream transmission in PONs. Optics currently developed for 100 Gbit/s and 400 Gbit/s data center applications (typically using 25 Gbaud and 50 Gbaud line rates) can be leveraged and serve as a starting point, however these components may not be sufficiently performant (e.g. have insufficient launch power at the transmitter side or have insufficient sensitivity at the receiver side) or may not meet the price criteria, especially at the ONU side [1]. Secondly, transmission distances are significantly longer compared to intra-data center links and hence chromatic dispersion will have significant impact at 25 Gbit/s and 50 Gbit/s line rates. Deploying transmission links in the O-band may alleviate this problem to some extent if one can stay sufficiently close to the zero-dispersion point of the deployed optical fiber, but goes with higher fiber attenuation (see Fig. 2.5 in Chapter 2).

Meeting optical budgets will be very challenging due to the reduced sensitivity of 25 Gbit/s and 50 Gbit/s optical receivers compared to today's 10 Gbit/s capable receivers. The two developed receivers from Chapter 3 and Chapter 4 have input dynamic ranges of 17.7 dB and 21.6 dB for 25 Gbit/s NRZ, and only 10.9 dB and 15.8 dB for 50 Gbit/s PAM-4. These results barely meet the specifications for the different standards listed in Table 2.2, moreover because ideal transmitters were used for the characterization of these receivers (e.g. modulation using MZM and pre-emphasis to open the reference eyes in the RX reference receiver). In addition, the obtained sensitivities are still far from those in Table 2.2. This is because the receivers were characterized using PIN-photodiodes: in reality, APDs will be needed to achieve the desired sensitivity levels.

This chapter serves as a bridge between the results obtained from previous chapters and those needed by next-generation PON standards by investigating this concept of equalization to compensate fiber dispersion (also known as EDC) or the relatively low bandwidth of the used optical components. Such equalization in the upstream burst-mode transmission in PONs has already been investigated using fixed-tap equalizers to compensate the bandwidth of the APDs-photodiode at the receive side only [2], but its full potential can only be realized by using a BMEQ which adapts the equalizer parameters on a burst-to-burst basis.

At the time of writing, no such real-time BMEQ implementations exist, but some experiments have been performed using offline processing in [3], using a LBMRX [4] at 10 Gbit/s. In this chapter, the LBMTIA from Chapter 3 is used in an experimental optical link setup using low-cost optical components and a portion of fiber of significant length, mimicking actual PON upstream transmission at 25 Gbit/s). Then, BMEQ is applied to the captured signals through offline processing, to gain insight into specific penalties and tradeoffs such as limited training time and burst-to-burst phase variation. The contents of the first part of this chapter are based on the paper, entitled:

G. Coudyzer, P. Ossieur, L. Breyne, A. La Porta, S. Paredes,
J. Bauwelinck, and X. Yin, "Study of Burst-Mode Adaptive Equalization for >25G PON Applications [Invited]," *Journal of Optical Communications and Networking*, June 2019.

5.1 The Upstream PON Experimental Setup

The experimental setup used to evaluate burst-mode equalization in upstream TDM-PON transmission links is shown in Fig. 5.2. Here, a DFB laser operating at a 1550 nm wavelength and a bandwidth of 10 GHz is directly modulated with 25 Gbit/s NRZ data using a high-speed AWG. A SOA is used to modulate the power of each burst. To synchronize the burst power modulation with the data generation, the function generator driving the SOA is triggered through the high-speed AWG. The ODN is represented by a single-mode fiber (SMF) together with a VOA to emulate the ODN losses. Finally, the LBMTIA from Chapter 3 is used as the front-end burst-mode receiver. A second assembly with this chip has been fabricated, in which the chip has been wirebonded together with two PIN-photodiodes on a PCB, as shown in Fig. 5.1.

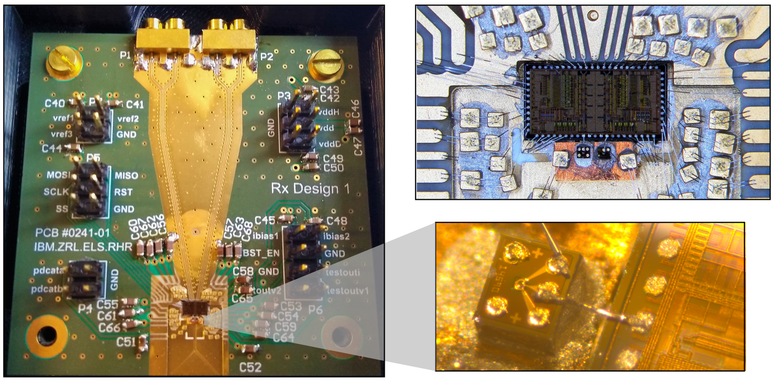

Figure 5.1: LBMTIA-assembly with PIN-photodiode.

Using the experimental setup from Fig. 5.2, a waveform has been created consisting of 2 successive bursts, where the power of the first burst is fixed and the power of the second burst is varied (as was done in the previous chapters). Each of these bursts contains 250 ns (6250 symbols) of 10101.. preamble (used for LBMTIA gain and offset adjustment), followed by a 2 µs payload section (50K symbols) with PRBS $2^{13}-1$ NRZ data. The bursts are spaced apart by a 500 ns guard time. The BER of the second, variable-power burst is then examined.

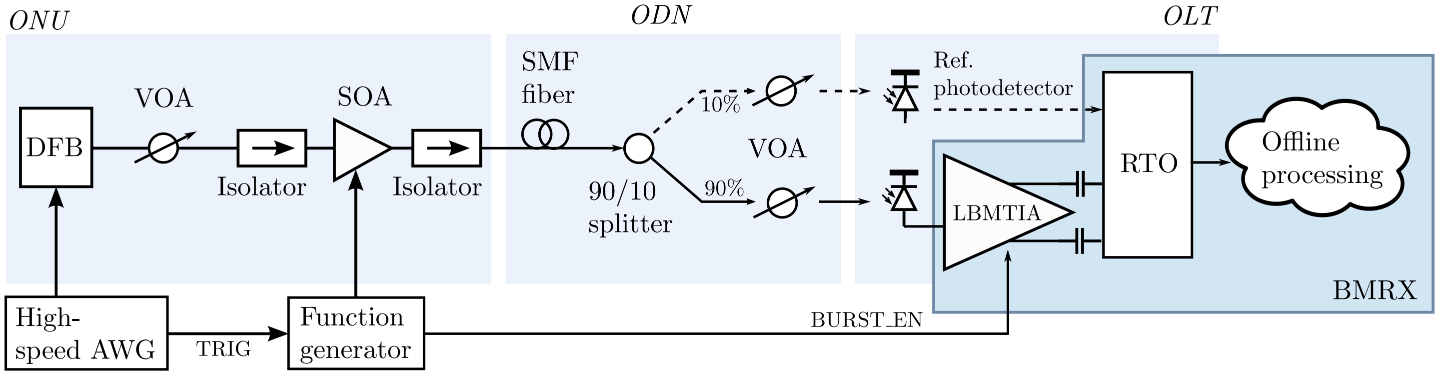

Figure 5.2: PON upstream link experimental setup. High-speed AWG: Keysight M8196A. C-band DFB: Exoptronics EX-7005. SOA: Inphenix IPSAD1504. Function generator: Tektronix AFG3102. VOA: Keysight N7762A. Reference photodetector: HP11982 Lightwave Converter. PIN-photodiode: Albis PD40. RTO: Lecroy SDA-830Zi-B.

Shown in Fig. 5.3 is the BER-performance of the link in a back-to-back configuration for the 4 configured slices with transimpedances ranging from 0.8 kΩ to 2.8 kΩ. A burst-mode / continuous-mode power penalty of 1.6 dB can be observed at the highest gain setting.

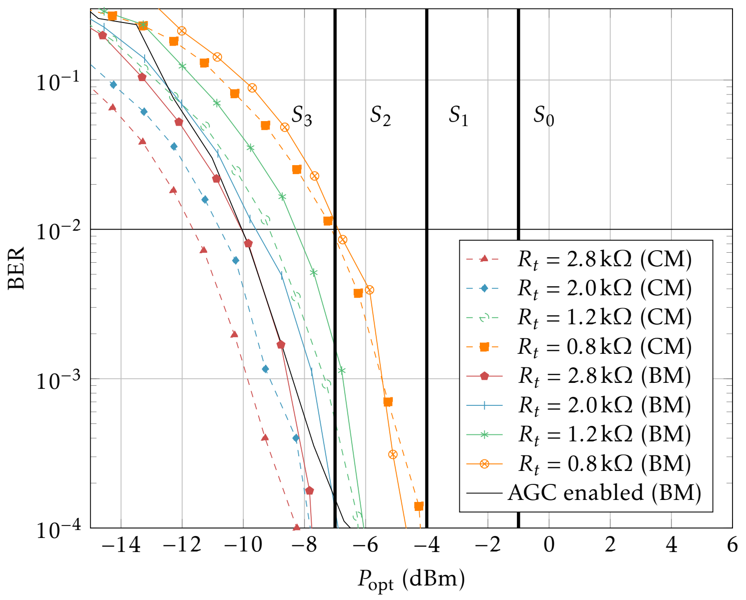

Figure 5.3: Back-to-back-BER versus the optical power for NRZ in continuous-mode and burst-mode (power of first packet fixed to $P_1 = -1.5$ dBm, power of second packet is varied), for 4 fixed gain settings of the LBMTIA and with AGC enabled.

In addition to the fixed-gain BER-curves, an additional BER-curve has been plotted, where AGC has been enabled. This AGC switches between slices when the power levels indicated by the vertical lines are exceeded. These levels can be arbitrarily chosen by setting the external reference voltages V_{REF1} through V_{REF3}.

As can be observed in Fig. 5.3, these levels were chosen such that the receiver keeps operating in its highest-gain mode (the AGC curve then coincides with the highest-gain curve). For NRZ transmission this makes sense, because reducing the gain is only beneficial at higher power levels where excessive jitter due to output saturation corrupts the eye diagram. Modulation formats such as PAM-4 on the other hand are more susceptible to this, as compression causes the outer eyes to close and hence the BER to rise (which was observed in Chapter 3). In Section 5.7 the performance impact of an AGC in front of the BMEQ will be investigated in more detail.

5.2 Impact of Fiber Dispersion

The insertion of a SMF into the link causes a severe degradation of the BER, as shown in Fig. 5.4. The use of directly-modulated DFB lasers introduces chirp which is exacerbated through the fiber, incurring a sensitivity penalty. One effect that can be observed is that the BER at 10 km fiber is better than at 5 km or even 2.5 km. At 20 km, the signal has been completely corrupted by dispersion, and a BER $< 1 \times 10^{-2}$ could not be achieved. A similar effect has been observed in [5], where 5 km is stated as the limit for directly modulated on-off keying (OOK) due to laser-induced chirp, without dispersion compensation. The eye diagrams at −7 dBm power at the receiver can be seen in Fig. 5.5.

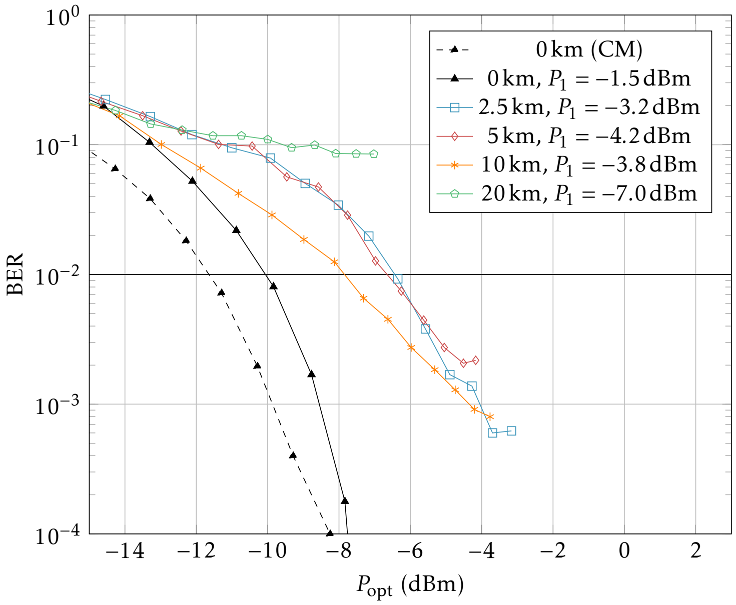

Figure 5.4: BER versus the optical power for NRZ in burst-mode, for different fiber lengths. P_1 is the power of the preceding loud packet.

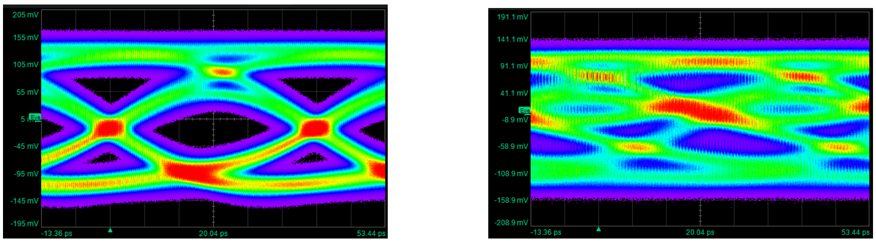

(a) back-to-back operation

(b) 2.5 km of fiber

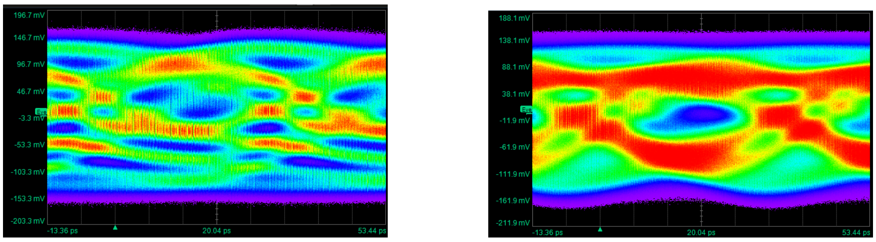

(c) 5 km of fiber

(d) 10 km of fiber

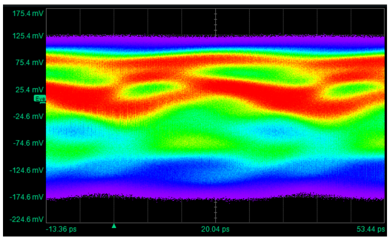

(e) 20 km of fiber

Figure 5.5: Received burst-mode eye diagrams for different fiber lengths, corresponding to the measurements around -7dBm in Fig. 5.4.

5.3 Burst-Mode Equalization for EDC

As stated in the introduction of this chapter, burst-mode electronic dispersion compensation (BMEDC) can be applied to improve the results in Fig. 5.4. Here, electronic dispersion compensation must be implemented on a burst-to-burst basis, re-adapting the weights during the preamble of each burst. To investigate the transmission performance improvements enabled by such a BMEDC, an adaptive FFE/DFE (shown in Fig. 5.6) is implemented in software and applied to the output signals of the LBMTIA, as captured by the RTO. First, we evaluate the performance improvement of the BMEQ in the case of a sufficiently long training duration, an ideally aligned training reference signal, and an input signal with its amplitude normalized to this reference signal. Then in the next sections, the sensitivity penalties arising from constraining these parameters will be individually investigated.

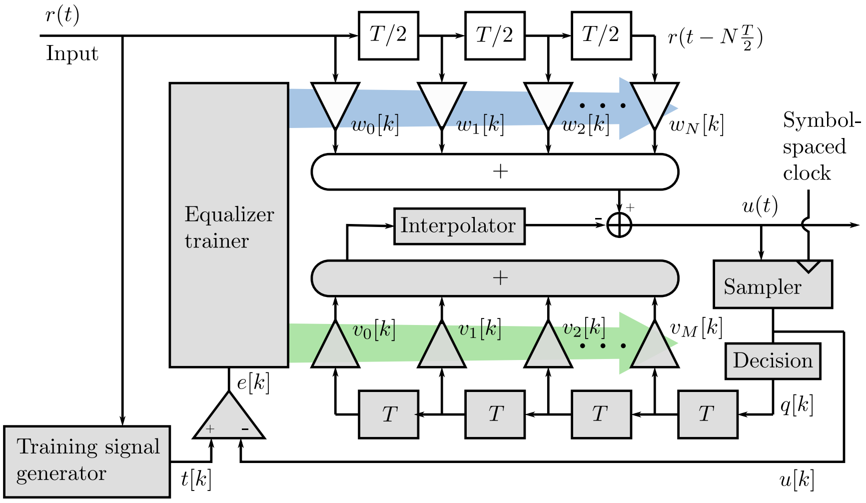

Figure 5.6: BMEQ-architecture.

In these experiments, the LMS algorithm is used to train the different taps of the FFE and DFE equalizers [6]. The weights w_i of the FFE filter are updated according to:

$$w_i[k+1] = w_i[k] + \mu_{\mathrm{FFE}} e[k] r(t_0 + kT - iT/2) \tag{5.1}$$

While the DFE-weights v_i are updated according to:

$$v_i[k+1] = v_i[k] + \mu_{\mathrm{DFE}} e[k] q[k-i] \tag{5.2}$$

In these equations, μ_{FFE} and μ_{DFE} are the adaptation coefficients, which can be increased to speed up the convergence of the tap weights. In the case of gear-shifted LMS, μ_{FFE} and μ_{DFE} are step-wise decreased over time. $r(t)$ is the received input signal, T is the symbol period, and $q[k]$ are the symbol samples after decision. The error signal $e[k]$ is determined by comparing the symbol samples $u[k]$ with the training sequence $t[k]$:

$$e[k] = t[k] - u[k] \tag{5.3}$$

First, the equalizers are trained using the entire payload of the burst to obtain the best achievable equalizer performance improvement (neglecting limited training durations). For this, a training sequence is used which is aligned to the center tap of the FFE structure. How this alignment can be achieved will be explained at the end of this chapter.

Then, the BER in these bursts is computed using the obtained FFE/DFE taps, and the resulting 1×10^{-2} sensitivity penalties compared to the continuous-mode back-to-back case are plotted as function of fiber length in Fig. 5.7. The equalized eye diagrams for the case of 5 km of fiber are plotted in Fig. 5.8.

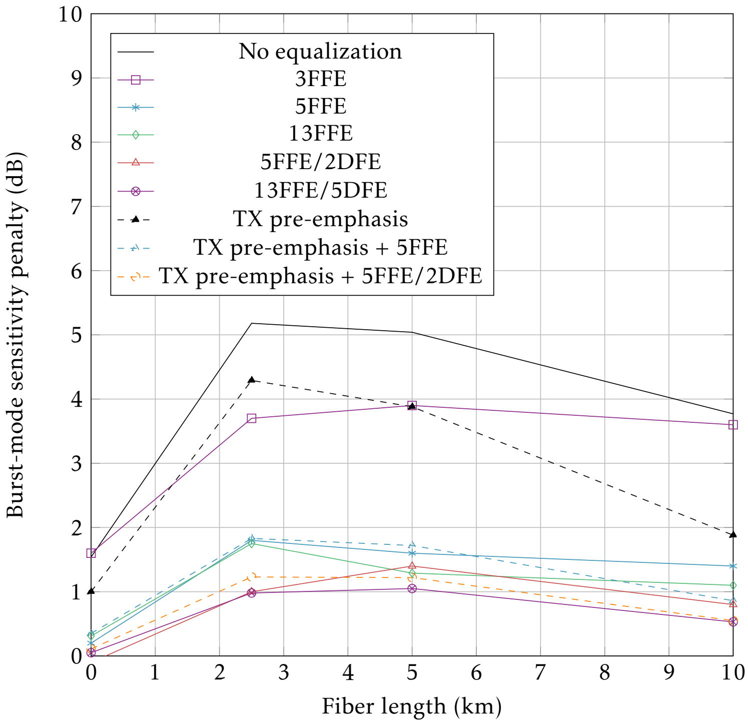

Figure 5.7: Burst-mode sensitivity as a function of fiber length for several link configurations. FFE-tap spacing is $T/2$ and DFE-tap spacing is T.

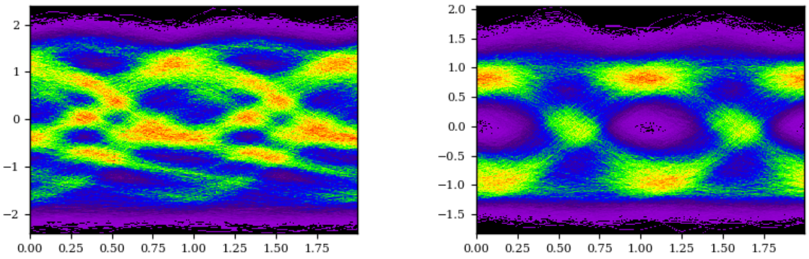

(a) Without equalization (b) After 5-taps FFE

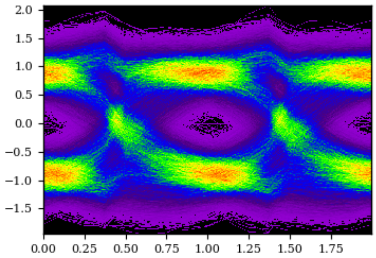

(c) After 5-taps FFE and 2-taps DFE

Figure 5.8: 5-taps FFE / 2-taps DFE equalization applied on the 5 km fiber signal as shown in Fig. 5.5c.

It can be seen that a simple 5-taps fractionally $T/2$-spaced FFE + 2-taps T-spaced DFE equalizer structure is already sufficient to reduce the sensitivity penalties well below 2 dB up until at least 10 km. Notice the lack of 20 km sensitivity penalties, as we were unable to achieve a BER of $< 1 \times 10^{-2}$ for this length of fiber.

For shorter lengths, the 5FFE+2DFE equalizer structure already outperforms the 13FFE, indicating the impact of the DFE structure. Notice that adding a DFE improves the sensitivity by less than 1 dB; which could be attributed due to the choice of the BER limit of 1×10^{-2}, where the erroneous detected bits are fed back into the equalizer, leading to error propagation.

In a second set of tests, a fixed 3-taps FFE was added at the transmitter (ONU) side with fixed coefficients (which were optimized for 0 km of fiber). It can be seen how such simple transmit-side equalization itself already reduces the sensitivity, even with no equalization at the receiver side. Further improvements can be observed when combined with receiver-side equalizers.

5.4 Impact of Limited Training Duration

In the previous section, the performance improvement of different equalizers was studied assuming a long training length. However, because the preamble time is limited, a sensitivity penalty arises from stopping the tap adaptation prematurely. Depending on the kind of equalizer and adaption algorithm used, different sensitivity penalties can be observed. For a 5-taps FFE + 2-taps DFE these are shown in Fig. 5.9, with normal standard LMS adaptation as well as gear-shifted LMS adaptation, in which μ_{FFE} and μ_{DFE} are reduced in 3 steps (50× → 10× → 1×) with equal step duration.

As shown in [3, 7], using gear-shifted LMS reduces the number of needed training symbols to obtain a certain equalizer performance. For example, less than 2 dB sensitivity penalty can be achieved with around 200 training symbols, in line with typical preambles for PON applications. Notice that at very short training durations, using only an FFE leads to lower burst-mode sensitivity penalties than when using a combined FFE/DFE structure. This indicates that the initial DFE tap weights can be further optimized, which is explored in the next section.

From an implementation point of view, gear-shifting is the most simple approach to improve the adaptation rate of the tap weights, while maintaining low mean-squared error after convergence. If additional hardware complexity and associated power consumption is acceptable, several more sophisticated algorithms exist to adjust the convergence coefficients μ_{FFE} and μ_{DFE}. In [8], the convergence coefficients are updated each step of the LMS algorithm according to:

$$\mu[k+1] = \begin{cases} \mu_{\mathrm{max}} & \text{for } \mu'[k+1] > \mu_{\mathrm{max}} \\ \mu_{\mathrm{min}} & \text{for } \mu'[k+1] < \mu_{\mathrm{min}} \\ \mu'[k+1] & \text{otherwise} \end{cases} \tag{5.4}$$

where

$$\mu'[k+1] = \alpha\mu[k] + \gamma e^2[k] \tag{5.5}$$

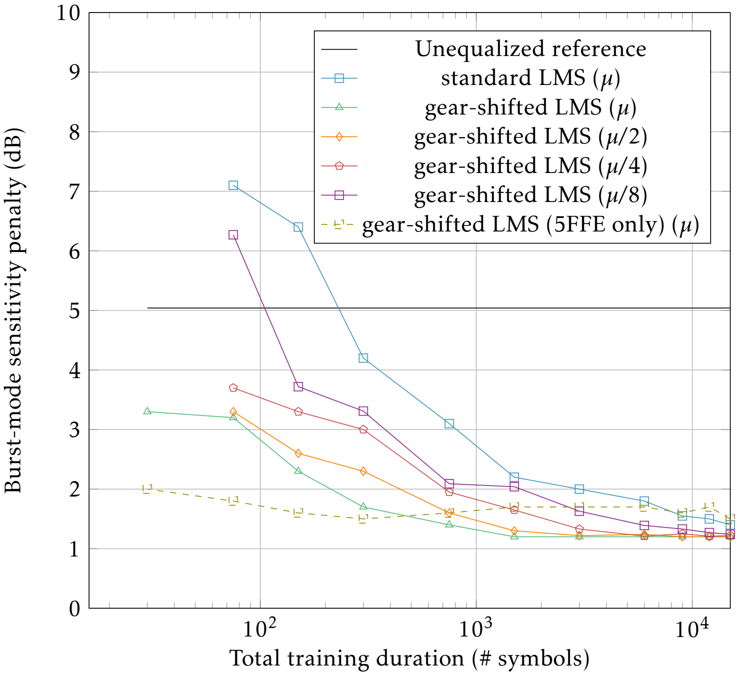

Figure 5.9: Burst-mode sensitivity penalty as a function of training duration (in # symbols) for LMS and gear-shifted LMS, for 5 km of fiber and 5-taps FFE/ 2-taps DFE.

Another approach presented in [9] is to detect sign changes in the gradient estimate, in which the underlying idea is that if there are no sign changes, the tap weights are still far from their optimum and hence the step-size can be increased. Conversely, if sign changes are detected in the gradient estimate, one is close to the optimum tap weights and the step-size should be decreased to reduce the mean-squared error. Both these algorithms have still reasonable additional computational complexity.

Finally, the RLS algorithm was studied for burst-mode electronic equalization in [3]. Under certain conditions, the RLS algorithm was found to converge at least one order of magnitude (expressed as the number of required training symbols to reach a given BER) faster than the standard LMS algorithm, at the expense of significantly higher complexity (number of multiplications involved).

5.5 Optimalization of Initial FFE/DFE Weights

As the resulting sensitivity penalty heavily depends on the initial weights, the question arises if an optimal initial weight setting can be found and more importantly, whether this setting applies to all fiber lengths, and thus, different ONUs.

Closer examination of the converged tap coefficients for the different fiber lengths reveals a relative degree of similarity, especially for the FFE. This proves that pre-emphasis with fixed tap coefficients can effectively improve the sensitivity of the link, as was already shown in Fig. 5.7. It should be noted however, that these results could be different when multiple (not necessarily identical) DFBs are used. Fig. 5.10 shows the converged tap coefficient for different fiber lengths, averaged over different input burst powers. The combined average of these taps can be used as a rough guideline into setting better initial FFE and DFE taps.

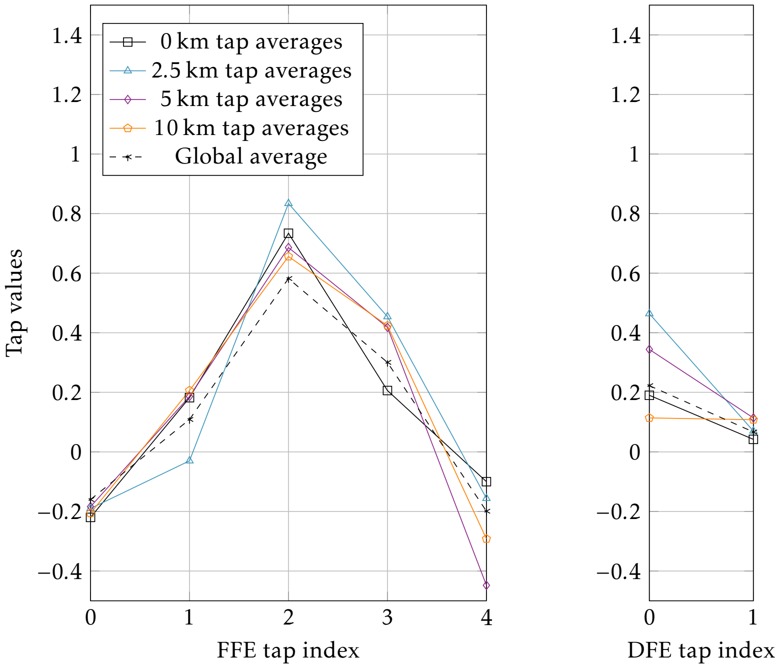

Figure 5.10: Converged tap values for the 5-taps FFE / 2-taps DFE structure.

Fig. 5.11 shows the sensitivity penalty versus the training length when the obtained averaged tap coefficients from Fig. 5.10 are used as initial values for the BMEQ. These show that the penalties are strongly reduced for short training durations. Also shown is the result for 10 km at the lowest μ_{FFE} and μ_{DFE}, to demonstrate that the chosen tap settings also work for other fiber lengths.

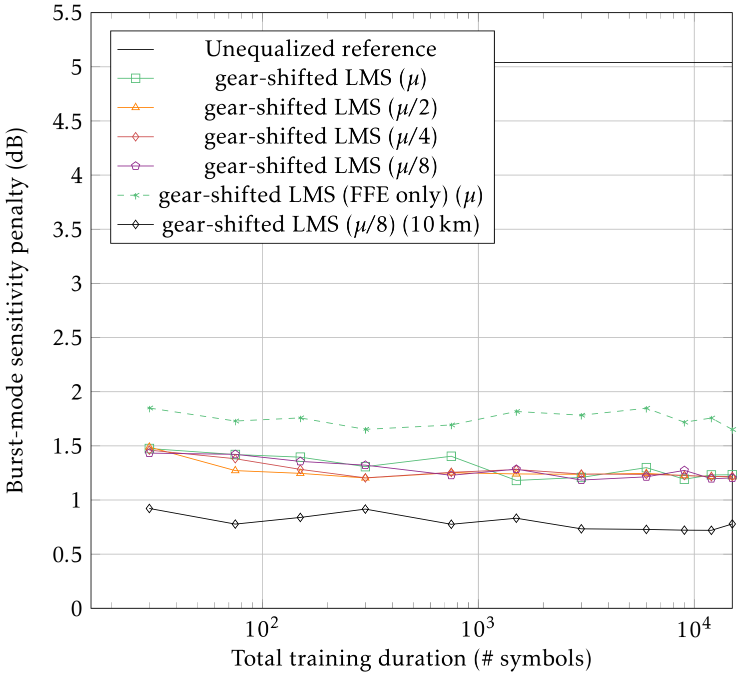

Figure 5.11: Burst-mode sensitivity penalty as a function of training duration (in # symbols) for LMS and gear-shifted LMS, for 5 km of fiber and 5-taps FFE/ 2-taps DFE with optimized initial tap settings.

5.6 Impact of Non-Ideal Training Signal Generation

Due to temperature variations along the fiber, each burst can arrive at the LBMTIA with an unknown phase with respect to the central OLT clock. Frequency offset can be neglected, as the bursts remain relatively short. In [7], the resulting phase offset was calculated and moderated by moving the center tap in the FFE. When sufficient taps are present, the FFE then re-aligns the input signal to the training signal.

The artificial alignment of the training signal to the input signal in the previous section has led to relatively small sensitivity penalties when the training duration was reduced and proper initial tap settings chosen. Furthermore, fewer taps could be used than in [7], reducing the complexity of the BMEQ. Shifting the training signal with respect to the input signal causes a significant increase of the training duration, as well as a penalty in the equalizer performance, as shown in Fig. 5.12.

These results show that the sensitivity penalty strongly increases in the case of a 5-taps FFE / 2-taps DFE equalizer when the training signal is shifted by more than $T/4$ (10 ps). For a 13-taps FFE / 5-taps DFE this effect is much less severe, as more taps are available to shift the training signal. However, this does require a longer training duration, as the previously chosen initial taps now all have to be shifted.

5.7 Impact of BMRX Output Dynamic Range

In the previous sections the amplitudes of the input signal and the training reference signal were normalized, mimicking an ideal AGC in front of the BMEQ. Without this normalization, the speed of convergence reduces with the input amplitude, as the step-size for the weight updates in Eq. (5.1) and Eq. (5.2) are reduced with at least the same factor.

In order to investigate the impact of swing reduction at the input of the BMEQ, the input swing is artificially reduced using a scaling factor $K < 1$. The experiment is performed for different train-

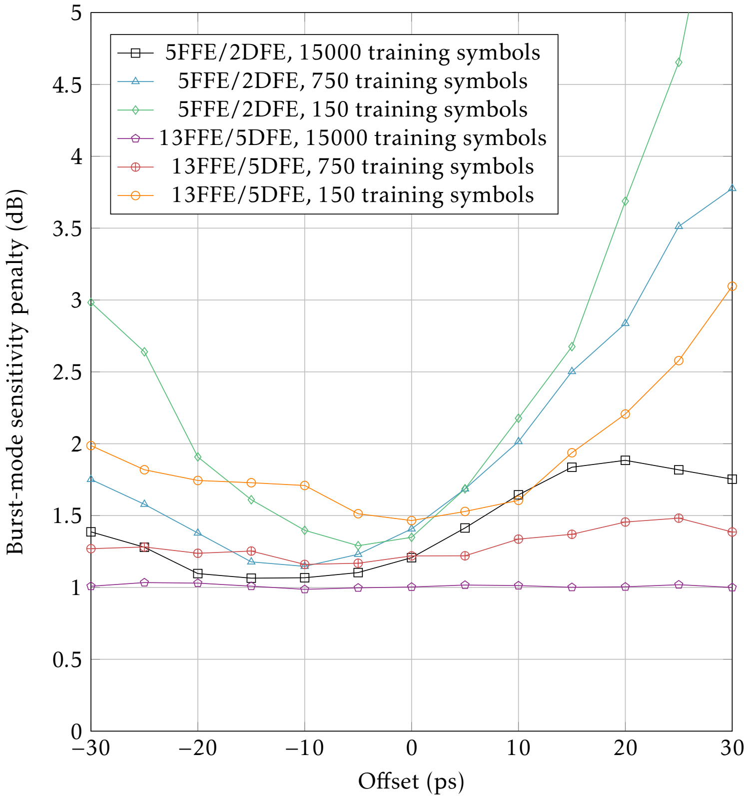

Figure 5.12: Sensitivity penalty as function of reference signal shift for various training lengths and equalizers, and optimum initial tap settings.

ing lengths, in which geared-LMS is used to train the 5-taps FFE/2-taps DFE equalizer with properly initialized weights. The result is shown in Fig. 5.13, where the burst-mode sensitivity penalty is plotted against the scaling factor K. In this figure, $K = 1$ refers to the situation shown in Fig. 5.11 (gear-shifted LMS, μ).

As can be seen from Fig. 5.13, the sensitivity penalty sharply increases when reducing the input amplitude beyond $K = 0.7$ (for 150 symbols). Decreasing the training length moves this threshold closer to the normalized value, as the LMS-training has not completely converged due to a lower convergence rate. From this graph, the specifications on the output dynamic range of the burst-mode front end can be deduced.

When the maximum allowed additional power penalty due to swing variations is limited to 1 dB, then $K > 0.63$ at 150 symbols training length. This means that the output dynamic range of the burst-mode front-end must be limited to 4.0 dB. Note however, that a sub-optimal choice of initial tap settings will require the training length to be increased for this result to remain valid.

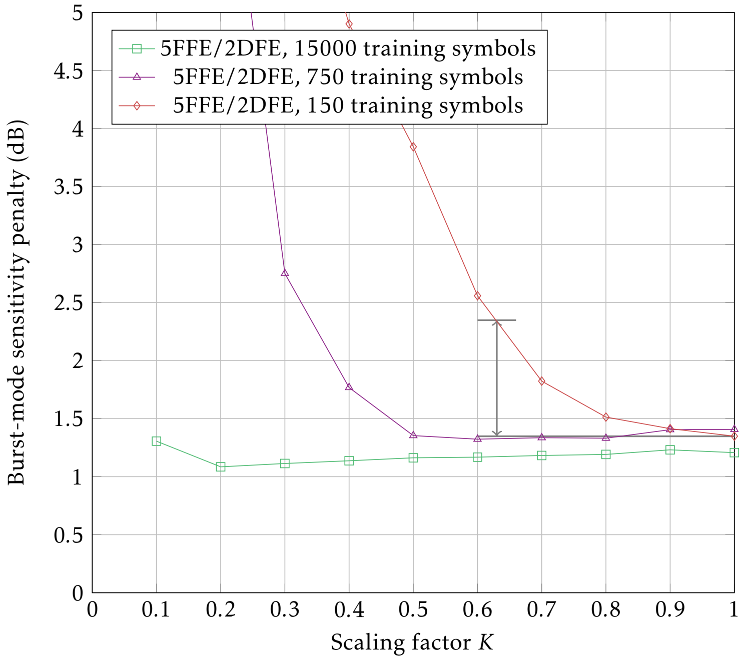

Figure 5.13: Sensitivity penalty as function of the input swing relative to the training signal and DFE slicer output amplitude. $K = 1$ corresponds to the normalized situation.

5.8 Conclusion

In this chapter, the feasibility of directly-modulated, single-channel 25 Gbit/s NRZ upstream transmission over up to 10 km was investigated, using a LBMTIA and BMEDC applied in the form of offline-processing. The use of direct modulation limits the reach in these links to about 10 km. Using a 5-taps FFE and a 2-taps DFE gets rid of most of the dispersion introduced in the link, with a remaining burst-mode sensitivity penalty of < 1.5 dB. It was shown that proper, re-usable initial tap settings can be found to reduce the sensitivity penalty when the training length is limited. When the training signal is shifted with respect to the input signal for more than 10 ps ($T/4$), significant sensitivity penalties are introduced that require additional taps to be used, as well as extra training time to align the center tap back with the training reference signal. Finally, the impact of swing variations at the input of the BMEQ is investigated, showing sensitivity penalties of > 1 dB due to limited training duration when the LBMTIA output dynamic range exceeds 3.7 dB. These criteria can then serve as an initial starting point for the development of BMEDC electronic circuit implementations supporting 25 Gbit/s and beyond.

References

[1] E. Harstead, D. V. Veen, V. Houtsma, and P. Dom, “Technology Roadmap for Time Division Multiplexed Passive Optical Networks (TDM PONs),” *Journal of Lightwave Technology*, pp. 1–1, 2018.

[2] X. Yin, B. Moeneclaey, X. Z. Qiu, J. Verbrugghe, K. Verheyen, J. Bauwelinck, J. Vandewege, M. Achouche, and Y. Chang, “A 10Gb/s APD-based linear burst-mode receiver with 31dB dynamic range for reach-extended PON systems,” in *2012 38th European Conference and Exhibition on Optical Communications*, Sep. 2012, pp. 1–3.

[3] P. Ossieur, C. Melange, T. De Ridder, J. Bauwelinck, B. Baekelandt, X. Qiu, and J. Vandewege, “Burst-Mode Electronic Equalization for 10-Gb/s Passive Optical Networks,” *IEEE Photonics Technology Letters*, vol. 20, no. 20, pp. 1706–1708, Oct 2008.

[4] P. Ossieur, N. A. Quadir, S. Porto, C. Antony, W. Han, M. Rensing, P. O’Brien, and P. D. Townsend, “A 10 Gb/s Linear Burst-Mode Receiver in 0.25um SiGe:C BiCMOS,” *IEEE Journal of Solid-State Circuits*, vol. 48, no. 2, pp. 381–390, Feb 2013.

[5] W. Poehlmann, H. Schmuck, R. Bonk, and T. Pfeiffer, “First 20 Gbit/s Burst-Mode OOK Upstream with Direct Modulated Laser over up to 50km Single Mode Fiber,” in *Photonic Networks; 17. ITG-Symposium; Proceedings of*, May 2016, pp. 1–4.

[6] S. U. H. Qureshi, “Adaptive equalization,” *Proceedings of the IEEE*, vol. 73, no. 9, pp. 1349–1387, Sep. 1985.

[7] S. Porto, C. Antony, A. Jain, D. Kelly, D. Carey, G. Talli, P. Ossieur, and P. D. Townsend, “Demonstration of 10 Gbit/s burst-mode transmission using a linear burst-mode receiver and

burst-mode electronic equalization [invited]," *IEEE/OSA Journal of Optical Communications and Networking*, vol. 7, no. 1, pp. A118–A125, Jan 2015.

[8] T. Aboulnasr and K. Mayyas, "A robust variable step-size LMS-type algorithm: analysis and simulations," *IEEE Transactions on Signal Processing*, vol. 45, no. 3, pp. 631–639, March 1997.

[9] R. Harris, D. Chabries, and F. Bishop, "A variable step (VS) adaptive filter algorithm," *IEEE Transactions on Acoustics, Speech, and Signal Processing*, vol. 34, no. 2, pp. 309–316, April 1986.

6

Conclusions and Future Work

6.1 Conclusions

Passive optical networks are increasingly more being deployed as a cost-effective way of implementing Fiber-to-the-Home. The augmentation of access networks such as DSL and HFC with this technology allows for higher data rates, extended reach, lower power consumption and higher end-user capacity overall.

In this thesis disseration, two receivers have been developed for use at the OLT, operating in burst-mode. To allow multi-level modulation formats such as PAM-4 and duobinary and to allow EDC through burst-mode equalization, the receivers are designed to be linear over a very wide input dynamic range.

In Chapter 3, a first 25 Gbaud BMRX is designed where AOC and AGC have been implemented using a simple LUT which contains gain and offset settings for different level burst input power levels. At the start of each burst, the appropriate slice is then selected. The receiver was characterized in a back-to-back burst-mode experiment using indirect MZM modulation, and resulted in a sensitivity of −13.8 dBm for NRZ and −5.4 dBm for PAM-4, and an input dynamic range of 17.7 dB for NRZ and 10.9 dB for PAM-4. However, due to the discrete switching and the limited number of slices, the output dynamic range was still significantly large (4.3 dB).

These conclusions have led to the development of a second-generation BMRX in Chapter 4, which uses a continuous AGC/AOC instead of the previously used slice-switching to reduce the output dynamic range, while maintaining burst-mode operation and linearity. By combining feedforward and feedback control circuits with sample-and-hold techniques to maintain their state, low settling times are achieved while benefiting from the precision of the feedback loops. A sensitivity of −18.1 dBm for NRZ and −11.4 dBm for PAM-4 was obtained, with an input dynamic range of 21.6 dB for NRZ and 15.8 dB for PAM-4. In addition, an output dynamic range of at most 2 dB is obtained.

The second-generation receiver from Chapter 4 improves upon the first version in many aspects: the NRZ and PAM-4 sensitivities are increased with 4.3 dB and 6 dB respectivily. The input dynamic ranges for these modulation formats are increased with 3.9 dB for NRZ and 4.9 dB for PAM-4. Compared to the state of the art, we reported the best sensitivity using PIN-photodiodes at 25 Gbit/s NRZ and 50 Gbit/s PAM-4, measured for a BMRX. Finally, the residual output dynamic range obtained in Chapter 4 is 3 dB better than [1]. A full overview of key specifications of both receivers is given in **??**.

To investigate the feasibility of future next-generation access networks, the first-generation receiver was used in an optical link setup using low-cost optical components and a portion of fiber of significant length, mimicking actual PON upstream transmission. The increased impact of dispersion and bandwidth limitations at 25 Gbaud requires techniques such as EDC through equalization, requiring a BMEQ following the burst-mode front end. Chapter 5 investigates the requirements and components of such an equalizer, and covers several burst-mode aspects limiting its performance. A 5-taps FFE / 2-taps DFE gets rid of most of the dispersion introduced in the link, and increases the sensitivity with over 3 dB in the presence of up to at least 10 km of fiber. When the output dynamic range of the LBMRX is kept below 3.7 dB (as is achieved with the receiver presented in Chapter 4), the resulting sensitivity penalty due to limited training duration is less than 1 dB.

6.2 Future Work

The developed receivers can be used in a plethora of applications, ranging from the intended application of passive optical networks to the domain of optical packet switching in datacenters. In the latter, the dynamic range requirements are relaxed, whereas reducing the overhead (the burst preamble) becomes more important.

	[2]	[3]	[1]	Chapter 3	Chapter 4
Technology	32nm SOI	28nm	0.25 µm BiCMOS	0.25 µm BiCMOS	0.25 µm BiCMOS
Chip area†	$0.06\,\text{mm}^2$	$0.06\,\text{mm}^2$	$4.22\,\text{mm}^2$	$2.20\,\text{mm}^2$	$1.39\,\text{mm}^2$
Modulation format	NRZ	NRZ	NRZ	NRZ/PAM4	NRZ/PAM4
Data rate (Gbit/s)	25	25	10	25/50	25/50
Power consumption‡ (mW)	109	34.2	650	375	280
Photodiode responsivity (A/W)	0.5 (PIN)	4 (APD)	1 (PIN)	0.5 (PIN)	0.5 (PIN)
Data type	PRBS7	PRBS7	PRBS31	PRBS10	PRBS15
Reference BER	1E-2	1E-2*	1E-2	1E-2	1E-2
Sensitivity (dBm)	-12.5	-19.5*	-24	-13.1/-5.4	-18.1/-11.4
Input DR (dB)	-	5	22.7	17.7/10.9	21.6/15.8
Output DR (dB)	-	-	4.4	4.3	1.4**/2.0***
Reconfiguration time (ns)	31	2.24	50	48	82.7

† Estimated single channel core size. ‡ Single-channel power consumption.
* Extrapolated from measured data (closest point: $-19\,\text{dBm}$ for 1E-3).
** Over a subset ($-10 \rightarrow 3.5\,\text{dBm}$) of the reported input DR.
*** Over a subset ($-10 \rightarrow 4.4\,\text{dBm}$) of the reported input DR.

Table 6.1: Overview of developed BMRXs, compared with the state-of-the-art.

Notice that in this thesis dissertation the receivers were tested using PIN-photodiodes only. This is done to evaluate the performance of the receivers and impact of equalization without the bandwidth limitations that are introduced by slower APD-photodiodes. For actual PON-deployments, APD photodiodes will be required to meet the optical power budget. At the time of writing, an assembly featuring an APD photodiode wirebonded to the second-generation LBMRX (as shown in Fig. 6.1) is yet to be tested. This assembly can be used for a second upstream PON link experiment targeting sensitivity levels more in line with the specifications imposed in Table 2.2. Through offline processing, the feasibility study for BMEQ implementation from Chapter 5 can then be repeated with this second-generation LBMRX, where additional bandwidth limitations are introduced by the APD. This way, the dynamic range and sensitivity can be extended even further.

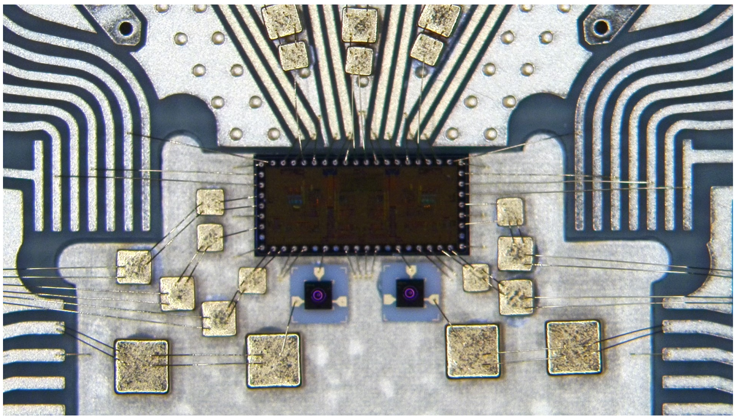

Figure 6.1: Wirebonded PCB-assembly with APD photodiodes.

The next step is then the development of the BMEQ implementation. This will require significant design effort, as the implementation involves complex mixed-signal design, combining both aspects from DSP with high-speed RF datapath performance. One aspect that has not been considered thus far is the necessity of a training signal generator, which generates the reference signal used during the adaptation of the LMS weights in the preamble of each burst. The generated reference should be aligned to the input signal such that the dominant tap in the FFE equalizer is positioned in the middle, after training. For this purpose, an aligner is necessary. One solution would be to use a serial aligner as shown in Fig. 6.2, which is commonly found in BER test equipment.

However, this solution fails to lock when the signal is heavily degraded. Alternatively, a correlation-based solution is shown in Fig. 6.3. In this system, the data is clocked serially into a shift register, after which an optimal correlation index is computed and used as the offset of a PRBS training sequence generator. Such a system could be implemented on an field programmable gate array (FPGA) or integrated together with the BMEQ.

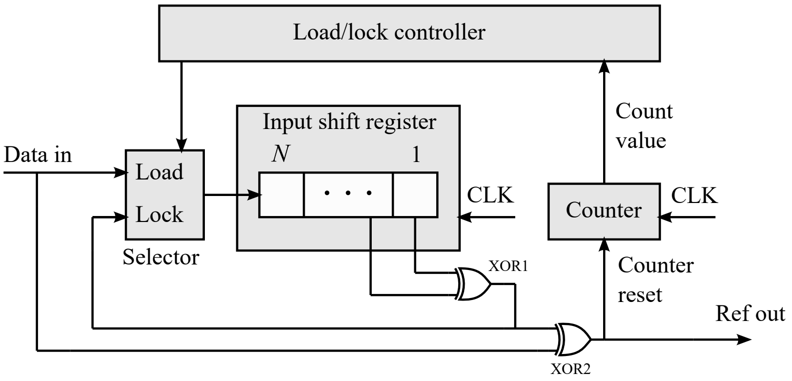

Figure 6.2: Serial aligner architecture.

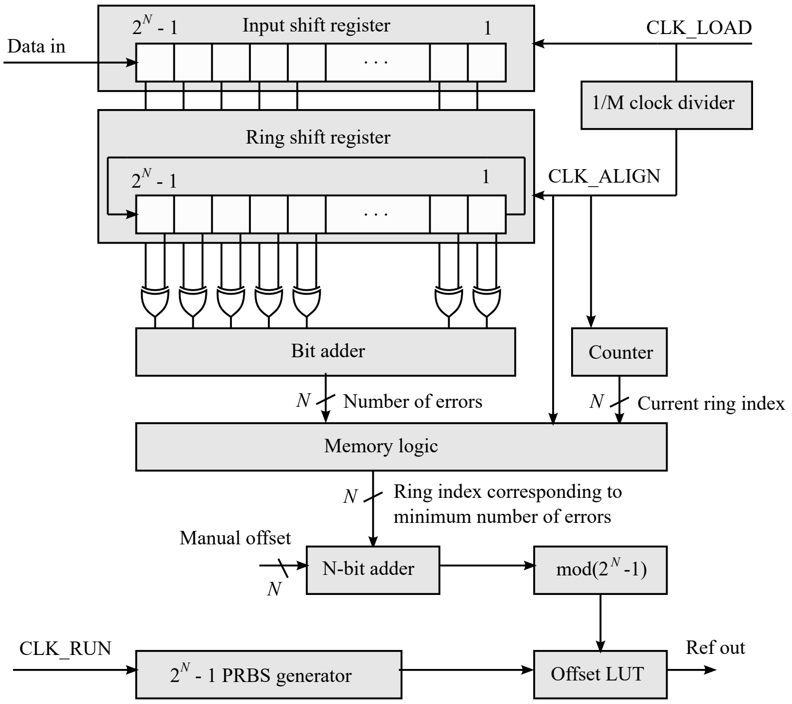

Figure 6.3: Proposed correlation-based aligner.

Finally, a third-generation BMRX should be developed in a more advanced technology, which allows implementing part of the AGC/AOC systems (e.g. feedforward AGC) in the digital domain, as well as improving the datapath performance to obtain better sensitivity levels and an even higher input dynamic range. Eventually, a fully developed BMRX (including AGC, AOC, equalization and BMCDR) can then one day be used as a promising OLT receiver for next-generation access networks.

6.3 Acknowledgements

The work in this Ph.D. is funded in part by the Ghent University Special Research Fund and the European Union's Horizon 2020 research and innovation programme, under projects WIPE (grant agreement N68857) and PICTURE (grant agreement N780930). In particular we would like to thank NXP for the fabrication of the two developed burst-mode receivers and the assistance of the Integrated Circuits (IC) Group (formerly known as the Mixed-Signal Microelectronics Group) from TU/e, as well as Albis Optoelectronics AG who provided the high-performance PIN-photodiodes.

The assembly used in Chapter 5 was fabricated by Ralph Heller from IBM Research Zurich. The work was supported by the Swiss National Secretariat for Education, Research and Innovation (SERI) under contract no. 15.0309. The opinion expressed and arguments employed herein do not necessarily reflect the official views of the Swiss Government.

References

[1] P. Ossieur, N. A. Quadir, S. Porto, C. Antony, W. Han, M. Rensing, P. O'Brien, and P. D. Townsend, "A 10 Gb/s Linear Burst-Mode Receiver in 0.25um SiGe:C BiCMOS," *IEEE Journal of Solid-State Circuits*, vol. 48, no. 2, pp. 381–390, Feb 2013.

[2] A. Rylyakov, J. E. Proesel, S. Rylov, B. G. Lee, J. F. Bulzacchelli, A. Ardey, B. Parker, M. Beakes, C. W. Baks, C. L. Schow, and M. Meghelli, "A 25 Gb/s Burst-Mode Receiver for Low Latency Photonic Switch Networks," *IEEE Journal of Solid-State Circuits*, vol. 50, no. 12, pp. 3120–3132, Dec. 2015. [Online]. Available: http://ieeexplore.ieee.org/document/7295549/

[3] K. C. Chen and A. Emami, "A 25-gb/s avalanche photodetector-based burst-mode optical receiver with 2.24-ns reconfiguration time in 28-nm cmos," *IEEE Journal of Solid-State Circuits*, vol. 54, no. 6, pp. 1682–1693, June 2019.